ESTIMATION AND FAULT DIAGNOSIS FOR VEHICLE ENERGY SYSTEMS

BY

PAMELA JOSEPH TANNOUS

DISSERTATION

Submitted in partial fulfillment of the requirements
for the degree of Doctor of Philosophy in Mechanical Engineering
in the Graduate College of the
University of Illinois at Urbana-Champaign, 2020

Urbana, Illinois

Doctoral Committee:

Professor Andrew Alleyne, Chair
Professor Carolyn Beck
Professor Srinivasa Salapaka
Associate Professor Prashant Mehta

Abstract

Driven by a desire to achieve reduced carbon emissions and maintenance costs, along with an increase in efficiency and performance, electrification has become a major trend in modern vehicles. This increase in electrification is accompanied by an increase in thermal power dissipated due to electrical inefficiencies. Consequently, temperature regulation becomes a greater challenge for these safety-critical systems.

Electrified vehicles consist of systems of systems that operate over a wide span of energy domains and timescales. To ensure their safe, reliable, and efficient performance, a holistic system perspective for estimation is needed. Accurate dynamic state estimation is critical for two main reasons:

1. *Thermal management:* This dissertation proposes a system perspective state estimation framework for complex multi-domain and multi-timescale dynamical systems. The framework consists of a multilevel hierarchical network of observers with each level having a unique update rate. To account for the significant interactions between subsystems, a novel bidirectional coordination strategy is developed. Sufficient conditions for the stability and convergence of the hierarchical network are derived. Experimental validation is conducted on a testbed representative of a fluid thermal management system of an electrified aircraft. Closed-loop simulation and experimental results confirm a reduction in computational cost compared to a conventional centralized observer and an increase in estimation accuracy compared to a decentralized observer which ignores coupling between subsystems.

2. *Fault diagnosis:* This dissertation proposes a robust system-perspective fault diagnosis framework for complex energy systems. Fault detection and isolation is derived from a set of structured residuals obtained from a bank of observers. Robustness is achieved by decoupling the unknown disturbances such as modeling error, linearization error, parameter variation, and noise from the residuals. The proposed approach is validated on a testbed representative of a fluid thermal management system of an electrified aircraft. Simulation and experimental results demonstrate successful fault detection and isolation with no false alarms or missed detections.

To my family, friends, and teachers.

Acknowledgements

I would like to thank my advisor Professor Andrew Alleyne for his continued support and guidance throughout the past 5 years. He has provided me invaluable opportunities that helped me grow as a researcher and an individual. I am very lucky that I had the chance to learn from him during my graduate studies. I would like also to thank the members of my doctoral examination committee, Professors Prashant Mehta, Srinivasa Salapaka, and Carolyn Beck for their support and feedback throughout my PhD research.

During my graduate studies at UIUC I had the opportunity to join the National Science Foundation Engineering Research Center for Power Optimization of Electro Thermal Systems (POETS) where I worked with great Professors and graduate students. I would like to thank Professors James Allison and Robert Pilawa-Podgurski and my colleagues Satya Peddada and Thomas Foulkes with whom I have collaborated on multi-disciplinary research. I have benefited greatly from this unique research experience with them. I would also like to thank the POETS faculty and staff for making POETS a great place to work. Especially, Professors Andrew Alleyne and Alan Mantooth, Jodi Gritten, Dr. Karen Bender, Sonya Chambers, Joe Muskin, and Dr. Jessica Perez. Also, a special thanks to Cyril Ribicki who helped me immensely in setting the experimental testbeds for my experiments. Finally, I would also like to thank all POETS students for supporting me during my time as conference chair to make the POETS conference a success.

I would like to thank my colleagues in the Alleyne Research Group for making Urbana-Champaign a great place to live. Thank you to Justin Koeln, Bryan Keating, Herschel Pangborn, Matthew Williams, Spencer Kieffer, Ashley Armstrong, Malia Kawamura, Chris Aksland, Nate Weir, Donald Docimo, Oyuna Angatkina, Spencer Igram, Sunny Sharma, Sarah Garrow, Cary Laird, and Mindy Wagenmaker. Also, a thank you to Reid Smith, Dylan

Charter, Kurtis Kuipers, Kayla Russel, Philip Renkert, Frank Lugo, and Chris Urbanski for carrying on with the ARG culture of collaboration and friendship.

I would like to thank my parents for being the main motivation for me to strive for success. With their hard work and dedication, they set a great example for me to work hard and follow my dreams. I would also like to thank my fiancé, Danny Lohan, for all his support throughout this process. He is a great source of inspiration and I am very grateful for having him in my life while working on my PhD.

Finally, all these great experiences would not have been possible without the financial support of the National Science Foundation Engineering Research Center for Power Optimization of Electro Thermal Systems (POETS) with cooperative agreement EEC-1449548.

Table of Contents

List of Figures

List of Tables

Chapter 1
Introduction

1.1 Motivation and Background

Over the past few decades, electrification has become a major trend in modern vehicles. Electric systems are progressively replacing previously used mechanical, pneumatic, and hydraulic systems as a means of transferring power within a vehicle. In the aerospace industry, the more electric aircraft (MEA) has been recognized as the future of aviation [1]–[3] due to its increased efficiency. For instance, the electric generation capability of the commercial aircraft Boeing 787 and Airbus A380 are approximately an order of magnitude higher than previous aircraft [1]. In the automotive industry, global electric vehicle (EV) sales are rising rapidly [4], driven by consumer preference and governmental requirements, with many hybrid or fully electric models in the market. Furthermore, electrification has become increasingly popular for both commercial and military ship development [5].

Vehicle electrification offers many benefits like reduced emissions and maintenance cost, and increased performance and efficiency. However, these benefits come at the expense of an increased thermal power dissipation caused by the electrical inefficiencies (i.e. battery, power electronics, electric machine, etc.) which leads to an inevitable increase in temperature. High temperatures, or hot spots, decrease reliability and performance and increase cooling cost and leakage power [6]–[8]. For example, there is a positive feedback loop between temperature and power leakage [8]. Additionally, a range of 10℃-15℃ difference in the operating temperature of a power electronics system can change its lifespan by a factor of 2 [9]. Therefore, accurate online state estimation is crucial for two main tasks:

1. *Real-time thermal management:* To further the development of electrified vehicles, sophisticated thermal management systems that meet the increased thermal requirements must be designed [10]–[19]. [20] indicates that 50-90% of military electronics failures can be attributed to ineffective thermal management techniques. State estimation is necessary to provide the information needed to design controllers for thermal management systems. Specifically, using accurate state estimates, controllers can be designed to improve the capability, the safety, and the reliability of a thermal management system. A system's capability represents its ability to meet mission objectives. A system's safety and reliability can be achieved by forcing the states of the system to stay within their operating constraints. For example, hierarchical model predictive control (MPC) represents an effective approach to manage the multi-domain and multi-timescale dynamics of electrified vehicles [21]–[23]. The main advantage of a hierarchical MPC approach compared to a centralized MPC approach is the ability of the controller to predict the performance of the vehicle far enough into the future at upper levels in the hierarchy as well as to respond quickly to unknown disturbances at lower levels with relatively low computational cost. Prior hierarchical control efforts [21]–[23] assumed full-state feedback. In practice, using sensors to measure every signal in a system is infeasible or prohibitively expensive in terms of sensor cost and installation. Furthermore, in some cases, sensors might affect the system's behavior. For example, a thermocouple can interfere with the useful thermal transport that could occur in their absence. Instead, an estimation algorithm provides the information needed for the hierarchical controllers. Consequently, the success of the control design becomes highly dependent on the success of the estimator. This emphasizes the need for accurate multi-domain dynamic state estimation that provides the data needed to control electrified vehicle systems.
2. *Real-time fault diagnosis:* State estimation is important to detect anomalies in the system performance. Careful online monitoring improves reliability of

electrified vehicles and allows lower safety factors and enhanced system performance. Moreover, since electrified vehicles are considered as safety-critical systems, it is vital to detect and identify any kind of potential malfunctions and faults as early as possible to minimize performance degradation and prevent possible complete system failure [24]. Examples of such faults are the blocking of an actuator (e.g. pumps, valves), the failure of a sensor (e.g. a thermocouple that fails to read the actual temperatures), or the disconnection of a component. Thus, faults are often classified as sensor faults, actuator faults, or plant faults. These faults are typically detected and located using analytical (also called software) or physical (also called hardware) redundancy [24], [25] approaches. Hardware redundancy approaches use multiple components with the same input signals so that the duplicated output signals can be compared to generate a diagnostic decision using methods like majority voting or limit checking [26], [27]. The major problems of this technique are the increased cost, weight, and volume introduced by the extra hardware needed. Hardware redundancy is a reliable technique, and it might be necessary to duplicate some critical components, however it is infeasible to apply this approach to every component of the system due to cost, space, and weight constraints. The constraints are particularly severe for electrified vehicles where space and weight, in particular, are at a premium. This problem can be solved using an analytical redundancy approach in which a mathematical model of the system is used instead of the extra hardware [28]–[30]. Observer-based FDI methods are one of the most well-known techniques based on analytical redundancy. The basic concept of observer-based FDI techniques is to compare the actual system behavior to the estimated system behavior obtained from an observer [30]–[35]. The residual generated from the difference between the actual response and the estimated response of the system is used to detect and isolate faults. The residual is zero in the fault-free case, and an increase in the value of the residual above zero indicates that a fault has occurred in the system. However, since perfect models do not exist in

practice, there will always be a discrepancy between the actual system's measurements and the estimated measurements obtained from the observers even when there is no fault in the system. This discrepancy causes false alarms and interferes with the performance of the FDI approach. Hence, to avoid false alarms, observer based FDI approaches should be designed to be robust to modeling uncertainties (i.e. modeling errors, linearization error, parameter variations, or model order reduction errors). On the other hand, reduction in the sensitivity of the FDI approach to modeling errors should not reduce its sensitivity to actual faults in the systems. Robustness is particularly important for the detection of incipient faults (i.e. drift change) since their effect on the residual is minor compared to the effect of abrupt faults (i.e. step change). Robust residuals can be generated using Unknown Input Observers (UIOs) through disturbance decoupling [36]. Additionally, to maintain state awareness and acceptable performance of these safety-critical systems under unexpected faults resilient control approaches have been investigated [37].

This dissertation proposes a system perspective estimation framework that is applicable to energy systems spanning multiple timescales and energy domains. Thus, it can be directly applied for thermal management systems of electrified vehicles. These systems consist of systems of systems interacting with each other over multiple time scales and multiple energy domains. MEA, EVs and all-electric ships (AES) have systems spanning the electrical, the thermal, the hydraulic, and the mechanical domains with dynamics operating at the sub-milliseconds timescale in the electrical domain and the minutes timescale in the thermal domain [22]. As an example, Figure 1.1 shows a schematic of the different components of the powertrain of a Mitsubishi i-MiEV. Each of these components or subsystems requires a specific range of operating temperatures to function effectively, reliably, and safely. Moreover, the dynamics of each component or subsystem are directly coupled to many other components or subsystems in the vehicle. Therefore, to prevent thermal failure, a holistic system perspective for thermal management should be adopted [10].

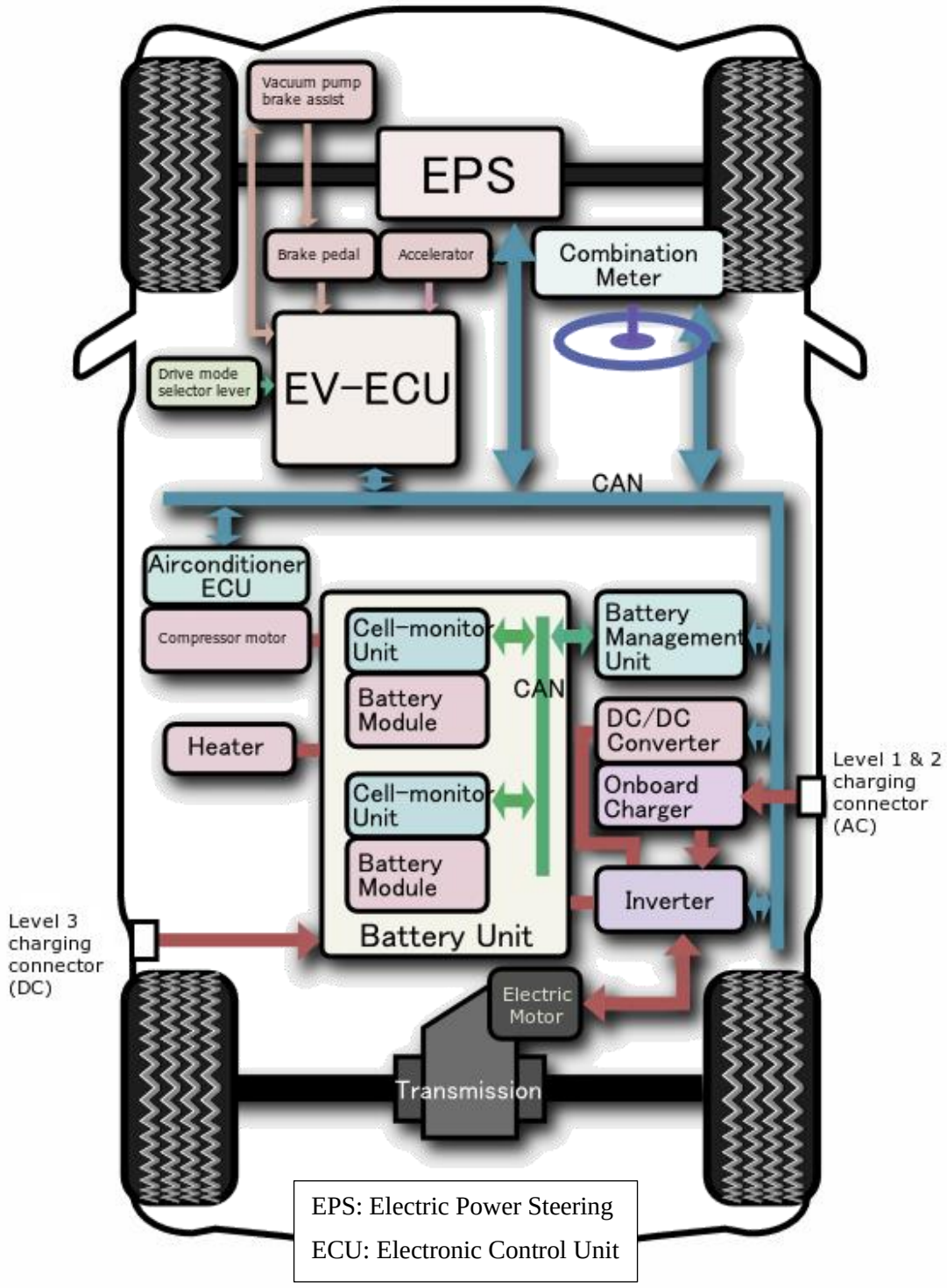

Figure 1.1 Mitsubishi i-MiEV System Schematic. [Modified from Wikipedia Commons].

As the system increases in complexity, it becomes more challenging to estimate its multi-domain dynamics with high speed, low memory requirements, and high capability in detecting and localizing anomalies using a centralized estimation approach [38]. Centralized estimation is usually computationally expensive as it relies on a single observer that accounts for all system interactions. On the other hand, decentralized estimation is less computationally demanding as it relies on multiple independent local observers each estimating their own part of the system. However, decentralized estimation completely ignores system's interactions which can lead to a reduced performance or even instability in highly coupled systems [39]. Hierarchical estimation combines the benefits of the two options by distributing the estimation problem among multiple local observers sharing information in a hierarchical framework. Hierarchical estimation is particularly useful when the overall system under control is characterized by dynamics of different timescales, e.g. slow and fast dynamics. Therefore, it is desirable to develop a hierarchical estimation approach for thermal management systems of electrified vehicles which must operate in transient mode and thereby require close observation and control.

1.2 Research Objectives

1.2.1 Problem Statement

To ensure safe, reliable, and efficient performance of electrified vehicles, a holistic system perspective for state estimation is needed. The coordination framework of this approach must directly consider coupling between subsystems, systems, and energy domains. In addition to the reduction in the computational power requirements, the proposed estimation approach should have the following features. First, this approach should be flexible in terms of the estimation algorithm used by each observer in the hierarchy. Therefore, specific nonlinear elements could be handled with nonlinear observers (e.g. Extended Kalman filter, Unscented Kalman filter, etc.) while leaving the linear elements to be observed by simpler linear observers (e.g. linear Kalman filter). Furthermore, it must be suitable for the multiple energy domains and timescales present in electro-thermal systems. Moreover, the algorithm should be designed to be scalable and modular. Therefore, the same algorithm can be applicable to different architectures or different systems that can be modeled in a similar way.

Additionally, to prevent failure of electrified vehicles due to unexpected faults in the sensors, actuators, or components of the system a fault diagnosis approach is needed. Such an approach should be designed to be robust to disturbances such as modeling error, linearization error, and model order reduction error. Furthermore, this approach should be designed to be modular and scalable so that it can be applied to electro-thermal systems of various architectures and components.

1.2.2 Dissertation Scope

The main contributions of this dissertation are the following:

1. Developing and experimentally validating a control-oriented hierarchical modeling framework that can capture coupling between components, subsystems, and energy domains. The resulting hierarchical models are simple enough for real-time implementation and detailed enough to accurately capture the dynamics of the systems. This approach relies on an aggregation-based model order reduction technique that preserves the correspondence between the reduced-order models and the physical systems.
2. Developing and experimentally validating a multilevel model-based hierarchical estimation approach with a novel coordination framework. The proposed approach is applied in real-time on a testbed representative of a fluid-based thermal management system for electrified vehicles. This approach is also generalizable to different vehicle systems with different architectures or components. A comparison with a conventional centralized observer and a decentralized observer shows the tradeoff between computational complexity and estimation accuracy achieved by the proposed hierarchical estimation approach.
3. Analyzing the stability of the proposed hierarchical estimation framework and deriving sufficient conditions for the convergence of the overall observer.

4. Analyzing the robustness of the proposed hierarchical estimation approach to faults at different levels in the hierarchy.
5. Developing and experimentally validating a robust fault diagnosis framework to detect and locate faults in thermal management systems of electrified vehicles. This approach can also be applied to different vehicle systems of various architectures and components.

Figure 1.2 provides a visual representation of the outline of the dissertation and the relations between the different contributions.

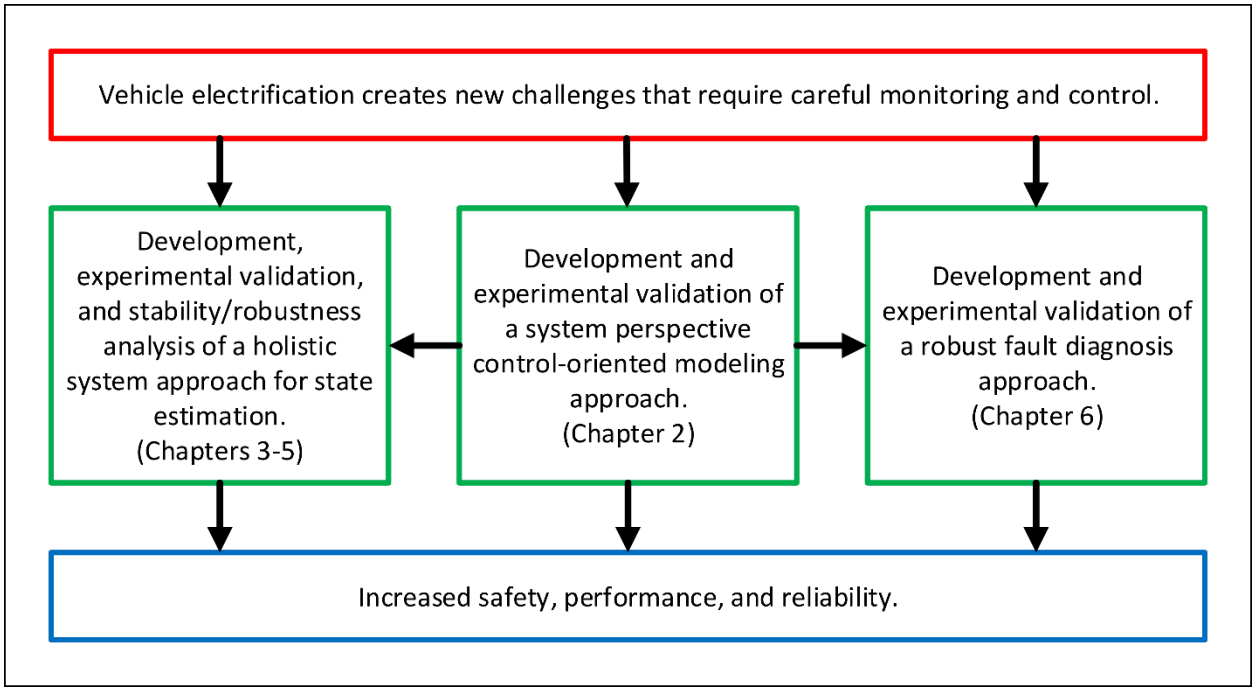

Figure 1.2 Dissertation Outline.

1.3 Organization of Dissertation

Chapter 2 presents the tools used to develop hierarchical models for electro-thermal systems. These tools include a previously developed [40] modular and scalable graph-based modeling approach, several system decomposition techniques that can be used to generate hierarchical models for the proposed hierarchical observer, and an aggregation-based model order reduction technique that can be applied to reduce the complexity of the models. Chapter 3

presents the architecture, formulation, and stability analysis of the proposed hierarchical estimation approach. Simulation and experimental results for a multilevel hierarchical observer coupled to a multilevel hierarchical controller are presented in Chapter 4. Furthermore, comparisons between the hierarchical observer, centralized, and decentralized observers in terms of estimation accuracy and computational complexity are also presented in Chapter 4. Chapter 5 investigates the robustness of the proposed hierarchical estimation approach to unexpected attacks or faults at different levels of the hierarchy. Chapter 6 presents the formulation of the fault diagnosis framework and the experimental validation of the approach on an example thermal management testbed. Chapter 7 concludes the main contributions of this dissertation and presents some topic for future research.

1.4 Notation

The symbol $\mathbb{R}$ denotes the set of real numbers. The symbol $\mathbb{R}^+$ denotes the set of non-negative real numbers. The symbol I denotes the identity matrix. x_i indicates a vector of i elements x_i, $i \in 1:N$. $\left[a_{ij}\right]$ denotes a matrix $A \in \mathbb{R}^{N \times P}$, with $i \in 1:N$, and $j \in 1:P$. Throughout the dissertation, lower-case subscripts and superscripts are used to name variables and upper-case superscripts are used to denote a mathematical function. For example, A^T denotes the transpose of a matrix A, and x^t represents a vector of sink states. The operator $|.|$ denotes the Euclidean norm of a vector and the operator $\|.\|$ denotes the Frobenius norm of a matrix. The symbol $\sup(.)$ denotes the supremum of a set. A function $\alpha:[0,\infty) \to [0,\infty)$ is said to be a class K function if it is continuous, strictly increasing, and satisfies $\alpha(0) = 0$. A function $\beta:[0,a) \times [0,\infty) \to [0,\infty)$ is said to be a class KL function if $\beta(.,t)$ is of class K for each fixed t and $\beta(r,t)$ is decreasing to zero as $t \to \infty$ for each fixed $r \geq 0$.

Chapter 2
Physics-based Lumped Parameter Dynamic Modeling

2.1 Background

To perform real-time model-based estimation, control, and fault diagnosis, appropriate models that balance between accuracy and computational complexity are needed. The chosen models should be simple enough for on-line implementation and detailed enough to simulate the dynamics at an acceptable level of accuracy. Dynamic models of energy systems can be developed using multiple simulation-based toolboxes such as the Thermal Management System (TMS) toolbox [41], Thermosys [42], and the Aerospace Power System (APS) toolbox [43], among many others. These toolboxes can be used to develop component-level models as well as system-level models by connecting individual component models according to a system topology. However, the models resulting from these toolboxes can not be directly represented by a set of equations needed for model-based estimation, control, and fault diagnosis. Furthermore, many of these simulation-based toolboxes do not directly consider the coupling between the different energy domains of an energy system. Bond graphs provide modular domain-independent graphical representations of system dynamics that can be used to derive state-space models. Their physical concepts are based on energy and energy exchange. In a bond graph, component energy ports are connected by bonds which represent the transfer of energy between the components of a system. Power along each bond is the product of a flow variable and an effort variable [44]. For example, in the electrical domain, effort represents voltage potential and flow represents current. In the hydraulic domain, effort represents pressure difference while flow represents volumetric flow rate. A drawback of this modeling approach is that system-level

models formed by interconnecting general-purpose component bond graphs can be extremely complex [45].

In this dissertation, an alternative graph-based modeling approach that balances modeling and computational complexity versus modeling accuracy has been adopted to derive control-oriented component-level and system-level dynamic models [40]. This modeling approach offers many benefits for the applications considered in this dissertation. First, it represents a modular and scalable modeling technique suitable for various systems of different complexities and architectures. For example, [46], [47] use this modeling technique to generate system-level electrified vehicles models, whereas in [48] it is used to generate a higher resolution component-level model of an inverter. Second, it is domain and timescale agnostic. Therefore, it can directly capture coupling between dynamics spanning multiple energy domains and timescales. For example, electrical and thermal graph-based models of electrified vehicles are derived in [43], [49]. These models capture the electro-thermal coupling of electrified air and land vehicles, respectively. Furthermore, hydraulic graph-based models for fluid-based thermal management systems of electrified vehicles are derived in [40] and [50]. Third, this graph-based modeling approach facilitates system decomposition which is vital for hierarchical estimation design. Example hierarchical graph-based models derived using this modeling approach can be found in [46], [47], [51].

The remainder of this chapter is organized as follows. Section 2.2 presents the general formulation of the graph-based modeling technique used in this dissertation. Graph-based modeling in the hydraulic and the thermal domains is presented in subsections 2.2.1 and 2.2.2, respectively. Various system decomposition approaches that can be used to generate hierarchical graph-based models are presented in section 2.3. Section 2.4 presents an aggregation-based model order reduction technique that can be used to reduce the computational complexity of the hierarchical models and, thus, the required computational time of the hierarchical observers. Concluding remarks are presented in section 2.5.

2.2 Graph-based Modeling

In this modeling technique, capacitive elements that store energy are represented by vertices, and the paths for energy transport between adjacent vertices are represented by edges

with each edge associated with a weight. The structure of the energy storage elements and the power flows throughout a system S is represented as an oriented graph $G=(v,e)$. v denotes the set of vertices $v=[v_i]$, for $i\in[1,N_v]$, where N_v represents the number of vertices of the graph G, and e denotes the set of edges $e=[e_j]$, for $j\in[1,N_e]$, where N_e represents the number of edges of the graph G. Each vertex v_i has an associated capacitance C_i and an associated dynamic state x_i. Each power flow P_j along an edge e_j is represented as a function of an associated edge input u_j and the head x_j^{head} and tail x_j^{tail} vertices it connects,

$$P_j = f_j(x_j^{tail}, x_j^{head}, u_j). \tag{2.1}$$

To represent interactions with neighboring systems or the external environment, a graph G also includes source edges $e^{in}=[e_l^{in}]$, for $l\in[1,N_l]$, with associated inlet power flows $P^{in}=[P_l^{in}]$, and sink vertices $v^t=[v_s^t]$, for $s\in[1,N_s]$, with associated sink states $x^t=[x_s^t]$. Inlet power flows and sink vertices are considered as disturbances to the graph G. That is, sink states are not considered as internal states and inlet power flows are not considered as internal power flows in the graph G. The orientation of each edge represents the direction of positive flow from the tail vertex v_j^{tail} to the head vertex v_j^{head}. The interconnection between the edges and the vertices of the graph G is described by an incidence matrix $M=[m_{ij}]\in\mathbb{R}^{N_v\times N_e}$, where m_{ij} is defined as

$$m_{ij}=\begin{cases} 1, & v_i \text{ is the tail of } e_j, \\ -1, & v_i \text{ is the head of } e_j, \\ 0, & else. \end{cases} \tag{2.2}$$

These graph-based models are governed by conservation laws. For example, in the thermal domain, graph-dynamics satisfy conservation of energy and in the hydraulic domain they satisfy conservation of mass. Therefore, the rate of change of the energy stored in each vertex v_i

of a graph G is determined by the difference between power flow in to v_i and power flow out of v_i as follows.

$$C_i \dot{x}_i(t) = \sum_{\{j | e_j \in \varepsilon_i^{head}\}} P_j(t) - \sum_{\{j | e_j \in \varepsilon_i^{tail}\}} P_j(t), \tag{2.3}$$

where $\varepsilon_i^{head} = \{e_j : v_j^{head} = v_i\}$ and $\varepsilon_i^{tail} = \{e_j : v_j^{tail} = v_i\}$ represent the sets of edges entering and leaving v_i.

By applying conservation of energy on each vertex in the graph, the dynamics of a system S represented by a graph G are given by

$$S : \begin{bmatrix} C\dot{x}(t) \\ \dot{x}^t(t) \end{bmatrix} = -MP + \begin{bmatrix} D \\ 0 \end{bmatrix} P^{in}, \tag{2.4}$$

where $x = [x_i]$ is the state vector for the internal vertices of G, $P = [P_j]$ is the vector of internal power flows along the edges, $C = diag([C_i])$, is a diagonal matrix of the capacitances $C_i > 0$, and $D = [d_{ij}] \in \mathbb{R}^{(N_v - N_s) \times N_l}$ is given by

$$d_{ij} = \begin{cases} 1, & v_i \text{ is the head of } P_l^{in}, \\ 0, & \text{else.} \end{cases} \tag{2.5}$$

The incidence matrix M can be partitioned as

$$M = \begin{bmatrix} \overline{M} \\ \underline{M} \end{bmatrix}, \ \overline{M} \in \mathbb{R}^{(N_v - N_s) \times N_e}. \tag{2.6}$$

That is, $\overline{M}$ represents a map from power flows P to internal state vertices x and $\underline{M}$ represents a map from power flows P to sink vertices x^t. Consequently, system dyanmics can be written as

$$C\dot{x} = -\overline{M}P + DP^{in}. \tag{2.7}$$

Figure 2.1 shows an example graph-based model that includes 4 internal vertices, 5 edges, 1 sink vertex v^t representing a surrounding system, and 2 source edges e_1^{in} and e_2^{in} entering the system from the surrounding environment or a neighboring system. The inlet power flows P_1^{in} and P_2^{in} along the source edges are not included in the vector of internal power flows, P, of G. Similarly, the sink state x^t associated with the sink vertex v^t is not included in the internal state vector x of G.

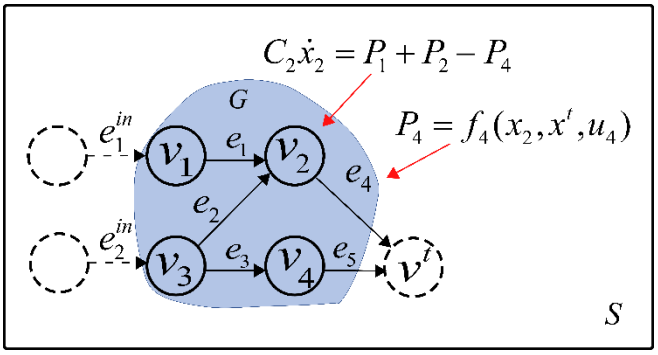

Figure 2.1 An example graph-based model.

2.2.1 Hydraulic Graph-based Models

In the hydraulic domain, the associated state of each vertex represents a pressure state p and the power flow along each edge represents a mass flow rate $\dot{m}$. Additionally, source power flows represent mass flow rates $\dot{m}^{in}$ entering the hydraulic graph from a neighboring system. Using this modeling technique, hydraulic graph-based models for single phase fluid-based thermal management systems of electrified vehicles are derived and experimentally validated in [40], [50]. In these references, the system is assumed to be closed, i.e. fluid does not enter or leave the system. Therefore, the hydraulic dynamics can be represented by

$$C\dot{p} = -\overline{M}\dot{m}. \tag{2.8}$$

A hydraulic graph-based model of a system is obtained by applying the conservation of mass principle on every component in the system separately. Equation (2.8) is then derived by combining the component hydraulic graph-based models according to the system topology.

Typical components of fluid-based thermal management systems of electrified vehicles include reservoirs, centrifugal pumps, liquid-to-liquid brazed plate heat exchangers, cold plate heat exchangers, flow/split junctions, valves, and pipes. Detailed derivation of the hydraulic graph-based model of each of these components shown in figure 2.2 can be found in [40]. For reservoirs, such as fuel tanks, the hydraulic capacitance is given by

$$C = \frac{A_c}{g}, \tag{2.9}$$

where A_c is the effective cross-sectional area and g is the gravitational constant. For all the other components, the hydraulic capacitance is given by

$$C = \frac{V\rho}{E}, \tag{2.10}$$

where V is the volume of the fluid in the component, ρ is the density of the fluid, and E is the bulk modulus. The mass flow rate $\dot{m}_j = f(p_j^{head}, p_j^{tail}, u_j)$ along hydraulic edges of pumps is given by

$$\dot{m}_j = \rho A_{c,j} \sqrt{2g(H_j - \frac{p_j^{head} - p_j^{tail}}{\rho g})}, \tag{2.11}$$

where H is the pump head and is determined empirically as a linear function of the pump speed ω and the pressure differential across the pump,

$$H_j = \alpha_{1,j} + \alpha_{2,j}(p_j^{head} - p_j^{tail}) + \alpha_{3,j}\omega_j. \tag{2.12}$$

α_1, α_2, and α_3 are constants. For all the other hydraulic edges, the mass flow rate is given by

$$\dot{m}_j = \rho A_{c,j} \sqrt{\frac{2(p_j^{tail} - p_j^{head} + \rho g \Delta h_j)}{\rho(f_j \frac{L_j}{D_j} + K_{L,j})}}, \tag{2.13}$$

where Δh_j is the height difference between the inlet and the outlet flow, f_j is the friction factor, L_j is the fluid flow length, D_j is the fluid diameter, and $K_{L,j}$ is the minor loss

coefficient. As shown in figure 2.2, graph-based models are based on the assumption of lumped parameters. Thus, the hydraulic dynamics of each component are captured by a single vertex. However, depending on the application and the available computational resources, a higher model fidelity can be achieved by increasing the number of states per component.

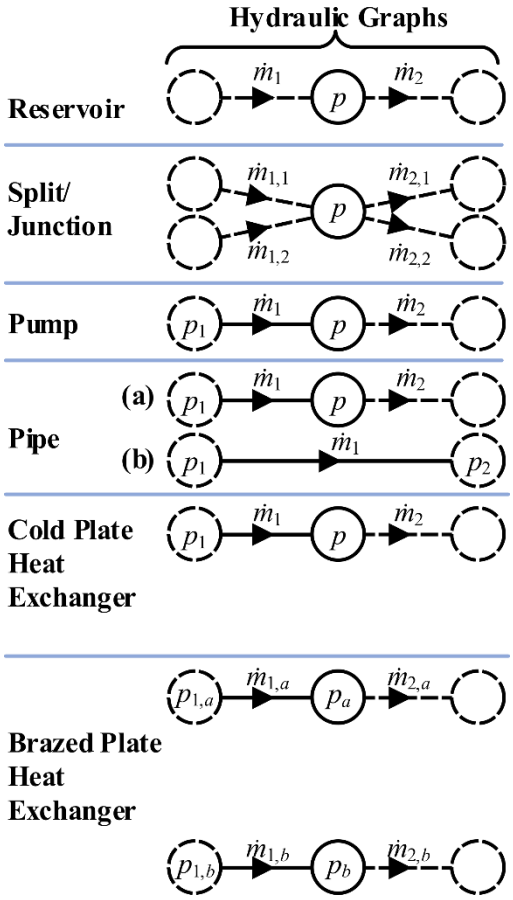

Figure 2.2 Hydraulic graph-based models for components typical of fluid-based thermal management systems of electrified vehicles. Modified from [40]**.**

2.2.2 Thermal Graph-based Models

In the thermal domain, each dynamic state x_i represents a temperature T_i and each edge e_j represents a thermal power P_j. For example, fluid-based thermal management systems are mainly governed by convective and advective power flows. An advective thermal power flow $P_j = f_j(T_j^{tail}, T_j^{head}, \dot{m}_j)$ is given by

$$P_j = \dot{m}_j c_{p,j} T_j^{tail}, \tag{2.14}$$

where $\dot{m}_j$ is the mass flow rate of the fluid entering the component, $c_{p,j}$ is the fluid specific heat capacitance, and T_j^{tail} is the temperature associated with the tail vertex. A thermal power flow due to convection is given by

$$P_j = h_j(\dot{m}) A_{s,j} (T_j^{tail} - T_j^{head}), \tag{2.15}$$

where h_j is the heat transfer coefficient, $A_{s,j}$ is the convective surface area, and T_j^{head} is the temperature associated with the head vertex. Thermal capacitances are given by

$$C_i = M_i c_{p,i}, \tag{2.16}$$

where M_i is the mass of the heat exchanger wall for vertices associated with heat exchanger wall temperature T_w (in figure 2.3) or the fluid mass for vertices associated with fluid temperature (i.e. T, T_a, or T_b in figure 2.3), and $c_{p,i}$ is the specific heat capacitance of the fluid or heat exchanger wall. For components with a varying fluid mass (e.g. reservoirs), the mass M_i is modeled as a time varying parameter. Detailed derivation and experimental validation of the thermal graph-based models for the components shown in figure 2.3 can be found in [40]. Similarly to the hydraulic graph-based models presented in subsection 2.2.2, the graph-based models presented in figure 2.3 are based on the assumption of the lumped parameters. Thus, the rate of change of the thermal energy stored in a thermal mass is represented by a single vertex v_i associated with a single dynamic state x_i. However, when needed, higher resolution thermal graph-based models can be derived. For example, in [48], a 79 state resistor-capacitor dynamic thermal graph-based model of a high power density inverter is derived and experimentally validated using this modeling technique. The edges of the thermal graph-based model presented in [48] are designed to capture thermal power flows due to conduction and convection heat transfer. Additionally, thermal radiation could readily be included in this framework by modeling it as a heat source or disturbance. For instance, the dynamic thermal graph-based model of a

cabin thermal management system of an electrified vehicle presented in [49], [52] incorporates solar load, internal loads from humans, ground reflected loads, and ambient air infiltration.

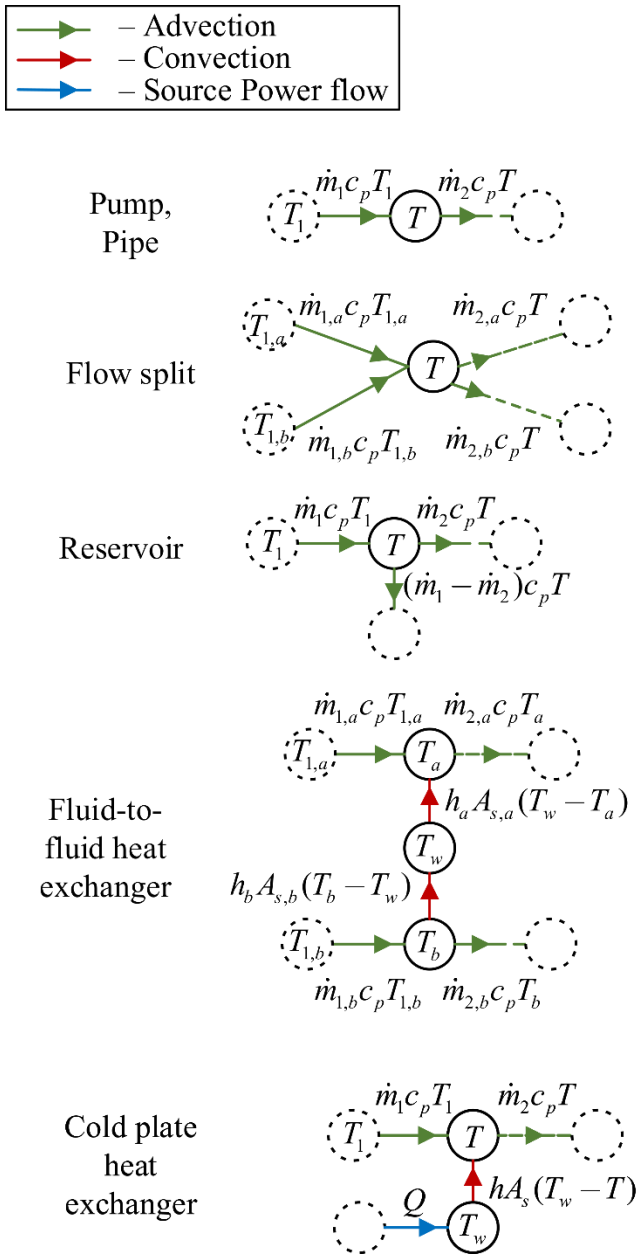

Figure 2.3 Thermal graph-based models for components typical of fluid-based thermal management systems of electrified vehicles. Modified from [40]**.**

2.3 Hierarchical Graph-based Models

To design a hierarchical observer, the system model must be decomposed into a hierarchy of interconnected systems and subsystems. There is a very rich literature on how to decompose a graph into multiple subgraphs or a hierarchy of subgraphs. An intuitive approach can be based on the spatial characteristics of the edges and the vertices of the graph. This can be related to the energy domain of the dynamics or the physical locations of the components. [53] proposes a partitioning algorithm derived from spatial considerations.

A hierarchical graph can also be derived using hierarchical clustering approaches [54], [55]. The output of these methods is a hierarchical tree, also called a dendrogram, whose levels represent segmentations of data sets. The main objective of clustering is to group data points within groups or clusters such that points of a single cluster have analogous characteristics to each other and different characteristics from points in different groups. Two subsets of these approaches are agglomerative methods and divisive methods. In agglomerative methods, each vertex is defined as its own cluster and, as the level of the hierarchy increases, the closest clusters are gradually merged into larger clusters (i.e. subgraphs, subsystems) until the graph of the entire system is reconstructed at the top-level of the hierarchy. There are multiple well-known hierarchical clustering methods [56], [57]. Additionally, [49] proposes a hierarchical clustering algorithm that focuses on minimizing coupling between the subsystems in the hierarchy. Divisive clustering approaches progress in an opposite direction. These approaches start with the entire system model at the top level of the hierarchy and as the level of the hierarchy decreases, edges of the graph are gradually cut to form smaller subgraphs (i.e. subsystems). A drawback of hierarchical clustering algorithms is the high time complexity resulting from gradually clustering datasets step-by-step [58].

Spectral graph partitioning is another popular tool that can be used to cluster vertices in a graph. These approaches are derived from graph theory with the goal of identifying communities of vertices in a graph based on the edges connecting them. Vertices of a community are highly coupled among themselves and weakly coupled to vertices of other communities. In these methods, clustering is performed using the eigenvalues and the eigenvectors of the Laplacian matrix of the graph [59], [60]. These methods can also result in a hierarchy of clusters (i.e. subsystems) [58], [61].

In this dissertation, the decomposition of the models is not unique, and the user can apply various decomposition approaches to derive a hierarchical graph-based model. For example, the hierarchical graph-based model used by the hierarchical observer in [51] and the hierarchical controller in [47] is based on the hierarchical clustering algorithm derived in [49]. Whereas, the hierarchical graph-based model used by the hierarchical controller in [62] and the hierarchical observer in [63] is derived based on spatial considerations.

Figure 2.4 shows an example 2-level hierarchical graph-based model. The top-level of the hierarchy consists of a graph-based model capturing the dynamics of the entire system. The lowest-level of the hierarchy comprises two subgraphs or subsystems derived by disconnecting edge 9 of the system-level graph-based model. The connecting vertices, also called coupling vertices in this dissertation, are modeled as sink states in the lowest-level subgraphs. More specifically, vertex 5 of the system-level model is modeled as a heat sink (or disturbance) to Subsystem 1 and vertex 4 of the system-level model is modeled as a sink vertex to Subsystem 2. A detailed formulation of an N -level hierarchical graph-based model is presented in subsection 3.5.1.

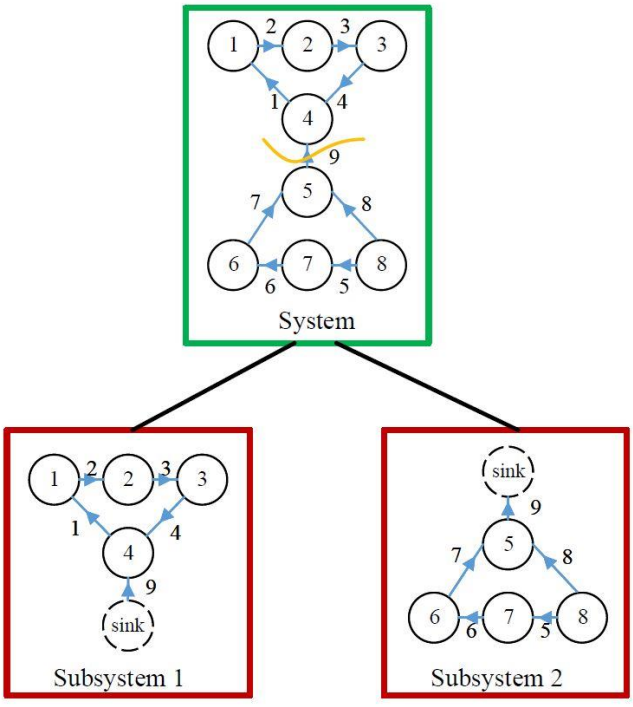

Figure 2.4 An example 2-level hierarchical graph-based model.

2.4 Structure-Preserving Model Order Reduction

2.4.1 Background

Electrified vehicles can be regarded as systems-of-systems that include hundreds of components. The dynamics of each component of these systems can be represented by tens of states [64]. Consequently, a graph-based model that captures the dynamics of an electrified vehicle system can consist of a very large number of states. Moreover, to capture the coupling between the multi-domain dynamics of these systems, the models should be simulated and controlled over small timesteps leading to prohibitively high demands on computational resources. Therefore, to facilitate online estimation and fault diagnosis, reduced-order models that balance between accuracy and computational complexity are required.

There are many methods available in the field of model order reduction (e.g. Truncated Balanced Realization, Hankel-norm reduction, etc. [65]). However, these approaches fail to retain the physical structure or the network topology of the reduced-order model. That is, the states of the resulting reduced-order model have no physical meaning. Nevertheless, preserving the physical correspondence between the reduced-order model and the physical system offers many benefits:

1. *Physical intuition:* A reduced-order model that preserves the physical meaning of its states is important for providing physical insights in large-scale dynamical systems. This results in easier model calibrations, and a better understanding of the complex interactions between the dynamics of the various subsystems through accurate, yet simple dynamical models.
2. *Multi-timescale dynamics*: Preserving the spatial structure of the model is directly related to preserving its temporal structure. This is very useful for designing the update rates of the observers and the controllers of multi-timescale dynamical systems (e.g. [66]).
3. *Sensor placement:* Preserving the structure of the network facilitates sensor placement which is a ctritical step in observer design. For example, [67] develops an optimal sensor placement approach for dynamic thermal

estimation of power electronic systems enabled by the experimentally validated structure-preserving reduced-order graph-based model developed in [48].

4. *Control design:* Tuning a model-based controller of a complex dynamical system (e.g. a model predictive controller) or a model-based observer (e.g. a Kalman filter) is simpler and more intuitive when a reduced-order model that preserves the physical structure of the full-order model is available (e.g. [68]).
5. *Fault diagnosis:* Electrified vehicle systems are considered as safety critical systems. Therefore, early detection and isolation of any fault that might occur in a sensor, an actuator, or a component of these systems is a high necessity. Fault diagnosis can be achieved by comparing the estimated states obtained from an online observer to the actual measured states obtained from the physical sensors of a system. That is, fast running models that can be implemented in real-time, and the ability to map measured signals to their corresponding estimated states are two major requirements for online model-based fault diagnosis (e.g. [48]). To achieve these two requirements, structure-preserving model order reduction techniques are needed.

2.4.2 Aggregation-based Model Order Reduction

Several structure-preserving model order reduction techniques can be found in the literature [69]–[72]. In this dissertation, low-order graph-based models are developed using an aggregation-based model order reduction technique derived from the timescale separation of the graph dynamics. Timescales can be identified by the eigenvalues or by the magnitude of the capacitances of a graph. For example, fast dynamics are associated with large eigenvalues and slow dynamics are associated with small eigenvalues [72]. Alternatively, vertices with large capacitances correspond to slow dynamics and vertices with small capacitances correspond to fast dynamics [68].

In the proposed approach, model order reduction is achieved by aggregating adjacent vertices belonging to the same dynamic group (e.g. slow, medium, or fast dynamics) into larger vertices, called "*super-vertices"*. Two vertices are defined as adjacent vertices if they are

connected to each other through an edge. Each *super-vertex* $\bar{v}_z$ is associated with a *super-state* $\bar{x}_z$ and a *super-capacitance* $\bar{C}_z$ given by

$$\bar{C}_z = \sum_{i \in \{1,2,...,N_V\}} C_i. \tag{2.17}$$

Similarly, a *super-power flow* $\bar{P}_z^{in}$ entering a *super-vertex* $\bar{v}_z$ is given by

$$\bar{P}_z^{in} = \sum_{i \in \{1,2,...,N_V\}} P_i^{in}. \tag{2.18}$$

Internal edges e_j in a *super-vertex* $\bar{v}_z$ are neglected. A graph-based model can be reduced from N_v dynamic vertices in the full-order model to M_v dynamic vertices in the reduced-order model by following steps 1-7 of Algorithm 1. The resulting dynamics of the reduced-order graph-based model can be represented by equation (2.7).

Algorithm 1: Aggregation-based Model Order Reduction Technique

---

1. Partition v into N_x dynamics groups D_k $(k = 1, 2, ..., N_x)$ such that for each k: $\forall (v_m, v_n) \in D_k$, $(m \neq n)$, $C_m \simeq C_n$. (N_x is defined by the user).
2. **for** $k = 1, 2, ..., N_x$ **do**
3. Aggregate adjacent (i.e. connected) vertices into N_w super-vertices $\bar{v}_z (z = 1, 2, ..., N_w)$. ($N_w$ is defined by the user).
4. **for** $z = 1, 2, ..., N_w$ **do**
5. $$\bar{C}_z = \sum_{i \in \{1,2,...,N_V\}} C_i$$
   $$\bar{P}_z^{in} = \sum_{l \in \{1,2,...,N_l\}} P_l^{in}$$
6. **end for**
7. **end for**
8. At the next level of the hierarchy, repeat steps 1-7 (until the top level is reached), such that for each D_k additional vertices are aggregated into larger super-vertices $\bar{v}_z$.

Step 8 of Algorithm 1 can be applied to design a hierarchical reduced-oder graph-based model needed for hierarchical estimation design. Specifically, in the proposed hierarchical

estimation framework (refer to section 3.3), high-level observers (and controllers) manage decisions at the system-level, whereas low-level observers (and controllers) manage component/subsystem dynamics. To reduce computational load, high-level observers can use low-resolution representations of the models used by low-level observers. However, high-level models should be accurate enough not to create large model mismatches and possibly lead to closed-loop instability. Consequently, the aggregation procedure presented in 1 (i.e. steps 1-7) can be repeated at each level of the hierarchy, such that as the level of the hierarchy increases the order of the model decreases. Additionally, at high levels of the hierarchy (e.g. the top level), higher reduction can be achieved by relaxing step 3 of Algorithm 1 to allow aggregation of adjacent vertices belonging to two dynamic groups. This is illustrated in the example reduced-order graph-based model presented in figure 2.5. In this example, the vertices of a graph-based model representing a subsystem of an electrified vehicle are divided into three dynamics groups (i.e. $N_x = 3$) based on the magnitude of their capacitances. Vertices with large capacitances belong to the slow dynamics group D_1 (i.e. red vertices in figure 2.5), vertices with small capacitances belong to the fast dynamics group D_3 (i.e. green vertices in figure 2.5), and the remaining vertices are grouped in the medium dynamics group D_2 (i.e. blue vertices in figure 2.5). At the 1st level (i.e. lowest level) of the hierarchy, the subsystem is represented by its full-order graph-based model to provide an accurate representation of the subsystem dynamics at the component level. At the 2nd level, a reduced-order model is designed by aggregating the adjacent vertices v_2, v_6, and v_7 of the lowest-level model into a single super-vertex $\bar{v}_2$, and adjacent vertices v_4, v_8, and v_9 into another super-vertex $\bar{v}_4$. At the highest level of the hierarchy (i.e. Level $\bar{3}$), super-vertices $\bar{v}_3$ and $\bar{v}_5$ of the second-level model are aggregated into super-vertex $\bar{v}_3$. That is, step 3 of the algorithm is relaxed to allow a higher model order reduction by only capturing low resolution dynamics at the system-level. Experimentally validated reduced-order models for fluid-based thermal management systems of electrified vehicles derived using this approach are presented in section 4.4.

Compared to conventional methods, this model order reduction technique offers many benefits. First, it maintains the structure of the graph. As a result, it preserves the physical correspondence between full-order and reduced-order models. Additionally, this technique

retains the timescale separation of the dynamics of the reduced-order model, which is valuable for hierarchical estimation and control design.

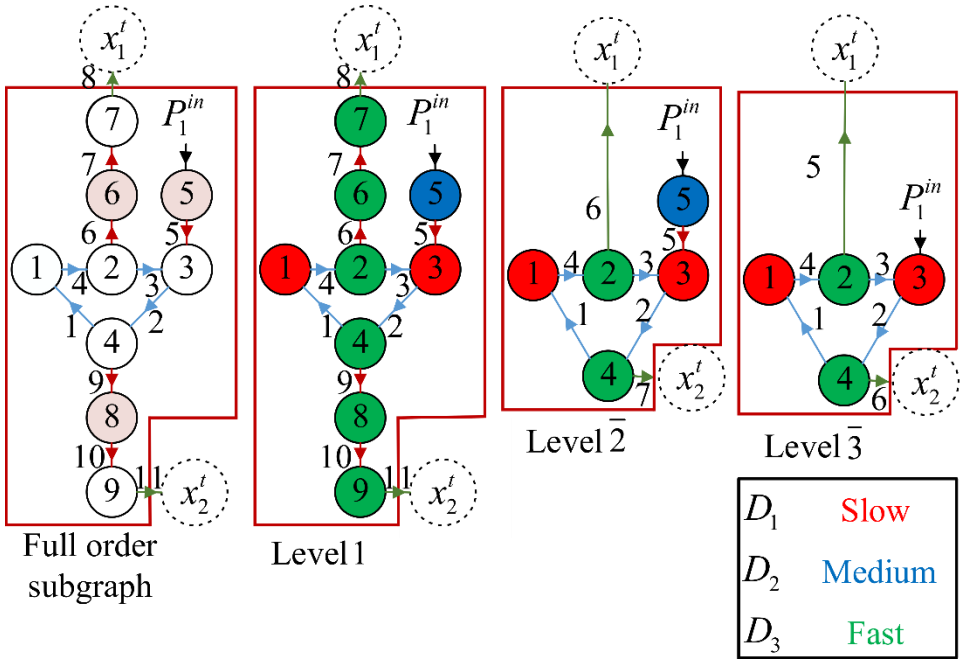

Figure 2.5 An example that illustrates the aggregation-based model order reduction technique used in this dissertation applied on a subsystem graph-based model in a 3-level hierarchy.

2.5 Conclusions

This chapter presented a physics-based lumped parameter modeling approach for multi-domain dynamical systems. The technique consists of representing lumped parameter models as graphs composed of vertices connected by edges. The resulting models can be simulated in real-time and can capture component-level and system-level dynamics. This modeling technique is energy domain and timescale agnostic. Consequently, it can directly account for the dynamic interactions that naturally occur in a multi-domain dynamical system. Additionally, the modeling approach is modular and scalable. Thus, it is suitable for various systems of different architectures. The general formulation of this graph-based modeling technique was presented in section 2.2. In subsections 2.2.1 and 2.2.2, it was used to derive physics-based models in the hydraulic and the thermal domains, respectively.

To design hierarchical observers, the graph-based model must be decomposed into a hierarchy of interconnected systems and subsystems. In this dissertation, the decomposition of the models is not unique, and section 2.3 presented several system decomposition approaches that can be used to generate hierarchical graph-based models. Section 2.4 presented an aggregation-based model order reduction technique that can be used to reduce the required computational time of hierarchical observers. The proposed technique is based on the timescale separation of the graph dynamics and maintains the physical correspondence between full-order and reduced-order models. Experimental validation of the lumped parameter modeling approach presented in section 2.2, one of the hierarchical system decomposition approaches presented in section 2.3, and the model order reduction approach described in section 2.4 are presented in Chapters 4 and 6 (refer to sections 4.6 and 6.5).

Chapter 3
Multi-level Model-based Hierarchical Estimation

3.1 Background and Motivation

Centralized and decentralized estimation represent two design options for estimating the states of a dynamical systems. Centralized estimation [73] provides high estimation accuracy, but it is usually computationally expensive as it relies on a single observer that accounts for all system's interactions. Decentralized estimation is less computationally demanding and relies on multiple independent local observers each estimating their own part of the system. However, the lack of communication between the observers of a decentralized framework negatively affects estimation accuracy and stability, especially in highly coupled systems.

Distributed estimation is an alternative approach that creates a tradeoff between centralized and decentralized estimation algorithms. This framework consists of a network of observers that exchange information among each other according to a network topology. In a distributed approach, each observer in the network relies on their local measurements and neighboring interactions to estimate the states of the system. Various methods for distributed estimation have been proposed in the literature (e.g. consensus-based algorithms [74], diffusion-based algorithms [75], etc.). However, in these approaches, each observer in the network is required to store and estimate the entire system model leading to large computational requirements. Furthermore, these approaches are not suitable for systems with multiple timescale dynamics since the observers of a distributed network are designed to update at a single update rate.

Hierarchical estimation is another approach that creates a tradeoff between centralized and decentralized estimation algorithms. In this approach, estimation is achieved by a hierarchical network of local observers sharing information among each other. Each local observer estimates the states of their own part of the system by relying on their local meaurements and information received from neighboring observers in the network. Hierarchical observers allow parallel processing, and thus are less computationally demanding than centralized observers. Furthermore, hierarchical observers account for subsystem's interactions, and thus can reach higher estimation accuracy and better stability than decentralized observers. Moreover, these observers are designed to update at different timescales at each level of the hierarchy which makes them suitable for systems characterized with multiple dynamic behaviors (e.g. slow and fast dynamics).

Most works on hierarchical estimation rely on the weighted least square (WLS) algorithm [76]–[83]. [84] presents a simple two-level Kalman filter-based hierarchical estimation algorithm for an ethylene-propylene-diene polymer (EPDM) reactor designed by decomposing the system model into two subsystems. The dynamics of the low-level subsystem are completely independent of the top-level subsystem. Therefore, only an upward flow of information was sufficient for the design of the hierarchical observer. [85] presents a two-level Kalman filter-based hierarchical estimation algorithm with a unidirectional flow of information to estimate the dynamics of power systems. Coupling among subsystems is ignored at the lowest level and only accounted for by a global observer at the top level of the hierarchy. [51] extends this algorithm to a multi-level hierarchical estimation approach. However, as shown in [85], the loss of information caused by ignoring subsystems interactions at low levels in the hierarchy can lead to a reduction in the estimation accuracy, and possibly affect stability, especially in highly coupled systems.

This chapter develops a multi-level hierarchical estimation algorithm with a novel coordination framework for multi-domain dynamical systems. In the proposed framework, subsystem's interactions are considered at all levels of the hierarchy through a bidirectional flow of information among the observers.

The remainder of this chapter is organized as follows. Section 3.2 presents the formulation of a benchmark centralized observer. The architecture of the proposed hierarchical

observer is presented in section 3.3. The advanatges of the proposed framework compared to conventional and current practices are presented in section 3.4. Section 3.5 presents the formulation, stability analysis and sufficient conditions for the convergence of the proposed hierarchical observer. Section 3.6 presents two case studies that demonstrate the boundedness and convergence of the proposed estimation framework. A conclusion for this chapter is presented in section 3.7.

3.2 Centralized Observer Formulation

This section presents two formulations for a benchmark centralized observer that can be used to estimate the dynamics of multi-domain dynamical systems modeled by the graph-based modeling approach presented in Chapter 2. The first formulation is based on representing the graph by a discrete linear time-varying model. This is enabled by assuming a state-affine form for the power flows along the edges of the graph. The second formulation is based on representing the system by a switched linear model.

The remainder of this section is organized as follows. A linear time-varying system representation is presented in subsection 3.2.1. The formulation of a conventional centralized discrete Kalman filter is presented in subsection 3.2.2. A switched linear system representation is presented in subsection 3.2.3. Finally, the formulation of a switched Kalman filter that can be used to capture switching dynamics of discrete actuators is presented in subsection 3.2.4.

3.2.1 Discrete Linear Time-Varying Model

By applying conservation of energy on each vertex, the dynamics of the internal states of a graph G are given by (see Chapter 2)

$$C\dot{x} = -\overline{M}P + DP^{in} \tag{3.1}$$

where $C = diag([C_i])$, is a diagonal matrix of the capacitances $C_i > 0$, x is a vector of the internal states, $\overline{M}$ is an incidence matrix that maps power flows $P = \left[P_j \right]$ to the internal states x, and D maps source power flows P^{in} to x. To facilitate a linear representation of the graph dynamics, it is assumed that the power flows along the edges of a graph can be represented by a state-affine form as follows.

$$P_j = f_j^{tail}(u_j)x_j^{tail} - f_j^{head}(u_j)x_j^{head}, \tag{3.2}$$

where $f_j^{tail}:\mathbb{R}\to\mathbb{R}^+$ and $f_j^{head}:\mathbb{R}\to\mathbb{R}^+$ are scalar functions, x_j^{tail} and x_j^{head} are the states associated with the head v_j^{head} and tail v_j^{head} vertices connected by edge e_j, and u_j is the actuator input along that edge. This assumption can be satisfied for many energy systems. For example, this assumption holds for thermal power flows of fluid-based thermal management systems (i.e. advective and convective power flows) as shown by equations (2.14) and (2.15). Specifically, advective power flows are modeled as $P_j = \dot{m}_j c_{p,j} T_j^{tail}$, where $\dot{m}_j$ is the fluid mass flow rate, $c_{p,j}$ is the fluid specific heat capacitance, and T_j^{tail} is the temperature associated with the tail vertex (i.e. the temperature of the upstream flow). Therefore, for advective power flows, $f_j^{tail}(u_j) = \dot{m}_j c_{p,j}$ and $f_j^{head}(u_j) = 0$. Similarly, convective power flows are modeled as $P_j = h_j(\dot{m})A_{s,j}(T_j^{tail} - T_j^{head})$, where $h_j(\dot{m})$ is the convective heat transfer coefficient, $A_{s,j}$ is the convective surface area, and T_j^{head} is the temperature associate with the head vertex. Therefore, for convective power flows, $f_j^{tail}(u_j) = f_j^{head}(u_j) = h_j(\dot{m})A_{s,j}$.

Consequently, the power flow vector P of a graph G can be written as

$$P = F(u)\begin{bmatrix} x \\ x^t \end{bmatrix}, \tag{3.3}$$

where x^t is the sink state vector, and $F(u) = [f_{ji}(u_j)] \in \mathbb{R}^{N_e \times N_v}$ is given by

$$f_{ji}(u_j) = \begin{cases} f_j^{tail}(u_j) & v_i \text{ is the tail of } e_j, \\ -f_j^{head}(u_j) & v_i \text{ is the head of } e_j, \\ 0 & \text{else.} \end{cases} \tag{3.4}$$

Furthermore, similarly to the incidence matrix M in equation (2.6), $F(u)$ can be partitioned into

$$F(u) = \begin{bmatrix} \overline{F}(u) & \underline{F}(u) \end{bmatrix} \tag{3.5}$$

where $\bar{F}(u) = [f_{ji}(u_j)] \in \mathbb{R}^{N_e \times (N_v - N_s)}$ and $\underline{F}(u) = [f_{ji}(u_j)] \in \mathbb{R}^{N_e \times N_s}$. Subsequently, by substituting equations (3.3) and (3.5) into (3.1), the dynamics of the graph-based model can be represented by a linear time-varying state space model as follows.

$$\begin{cases} \dot{x} = A(u)x + BP^{in} + E(u)x^t, \\ y = Hx + \upsilon, \end{cases} \tag{3.6}$$

where

$$A(u) = -C^{-1}\bar{M}\bar{F}(u), \tag{3.7}$$

$$B = C^{-1}D, \tag{3.8}$$

$$E(u) = -C^{-1}\bar{M}\underline{F}(u), \tag{3.9}$$

H is a mapping from the true states x to the measured states y, and υ is the measurement noise.

Finally, by assuming a zero-order hold for the edge inputs u, the source power flows P^{in}, and the sink states x^t, a discrete representation of the model dynamics can be written as

$$\begin{cases} x_{k+1} = A_k x_k + B_k P_k^{in} + E_k x_k^t, \\ y_k = Hx_k + \upsilon_k \end{cases} \tag{3.10}$$

where

$$A_k = e^{A\tau^s}, \tag{3.11}$$

$$B_k = A^{-1}(A_k - I)B, \tag{3.12}$$

$$E_k = A^{-1}(A_k - I)E, \tag{3.13}$$

τ^s is the sample time, I is the identity matrix, and k is the time index.

This class of systems can be proven open-loop stable under appropriate conditions on the connectivity of the graph and the current form of the equations governing power flow along its edges (i.e. equation (3.2)). For a detailed proof of the open loop stability of this class of system

the reader is referred to [62]. From the open loop stability of the system dynamics, it follows that the pair (A_k, H) is detectable and an asymptotic observer exists.

3.2.2 Centralized Discrete Kalman filter

The system dynamics represented by equations (3.10)-(3.13) can be estimated by a centralized discrete Kalman filter described by the following prediction and correction steps.

Measurement update (correction step)

$$\begin{cases} M_k := HP_{k|k-1}H^T + R_k \\ \hat{x}_{k|k} = \hat{x}_{k|k-1} + P_{k|k-1}H^T M_k^{-1}(y_k - H\hat{x}_{k|k-1}) \\ P_{k|k} = P_{k|k-1} - P_{k|k-1}H^T M_k^{-1} HP_{k|k-1}^T \end{cases} \tag{3.14}$$

Time update (prediction step)

$$\begin{cases} \hat{x}_{k+1|k} = A_k \hat{x}_{k|k} + B_k P_k^{in} + E_k x_k^t \\ P_{k+1|k} = A_k P_{k|k} A_k^T + Q_k \end{cases} \tag{3.15}$$

$\hat{x}_{k+1|k}$ and $\hat{x}_{k|k}$ represent the state estimates of x_k at times $k+1$ and k, respectively, given observations up to time k. $P_{k|k}$ and $P_{k+1|k}$ are the measurement update and time update error covariance matrices, respectively. P_0, the initial condition for $P_{k-1|k-1}$, is given by

$$P_0 = E[(x_0 - \hat{x}_0)(x_0 - \hat{x}_0)^T], \tag{3.16}$$

where $\hat{x}_0 = E[x_0]$, and $E[.]$ represents the expected value. Q_k and R_k represent the covariance matrices of the process noise and the observation noise, respectively. The *correction* and *prediction* steps (i.e. equations (3.14) and (3.15)) can be combined into a single step resulting in the following set of equations

$$\begin{cases} M_k := HP_{k|k-1}H^T + R_k \\ K_k = A_k P_{k|k-1}H^T M_k^{-1}, \\ \hat{x}_{k+1|k} = A_k \hat{x}_{k|k-1} + B_k P_k^{in} + E_k x_k^t + K_k(y_k - H\hat{x}_{k|k-1}), \\ P_{k+1|k} = A_k(P_{k|k-1} - P_{k|k-1}H^T M_k^{-1} HP_{k|k-1}^T)A_k^T + Q_k, \end{cases} \tag{3.17}$$

where K_k is the Kalman gain matrix of the observer.

3.2.3 Switched Linear System

Some systems comprise switching actuators that represent discrete events. In particular, several of the physical systems to be considered later in this dissertation fall into this class. For example, thermal management systems typically include valves opening and closing. Continuous-time systems with discrete switching events are called hybrid or switched systems [86]. To capture the discrete behavior of such actuators, u in equation (3.6) can be replaced by $u_{\sigma(t)}$, where $\sigma(t):[0,\infty)\rightarrow[1:N_m]$ is a switching signal that specifies the active mode of operation and N_m is the finite number of modes. Consequently, equation (3.6) can be represented as

$$\dot{x} = A_{\sigma(t)}x + BP^{in} + E_{\sigma(t)}x^t, \tag{3.18}$$

where

$$A_{\sigma(t)} = A(u_{\sigma(t)}) \tag{3.19}$$

$$E_{\sigma(t)} = E(u_{\sigma(t)}) \tag{3.20}$$

A discrete representation of equation (3.18) can be derived by assuming a zero-order hold for the edge inputs u, the source inputs P^{in}, the sink states x^t, and switching signal σ as follows.

$$\begin{cases} x_{k+1} = A^d_{\sigma_k} x_k + B^d_{\sigma_k} P^{in}_k + E^d_{\sigma_k} x^t_k, \\ y_k = Cx_{k,} \end{cases} \tag{3.21}$$

where

$$A^d_{\sigma_k} = e^{A_{\sigma_k}\tau^s}, \tag{3.22}$$

$$B^d_{\sigma_k} = A^{-1}_{\sigma_k}(A^d_{\sigma_k} - I)B_{\sigma_k}, \tag{3.23}$$

$$E^d_{\sigma_k} = A^{-1}_{\sigma_k}(A^d_{\sigma_k} - I)E_{\sigma_k}. \tag{3.24}$$

3.2.4 Switched Centralized Kalman filter

The system dynamics represented by equations (3.21) - (3.24) can be estimated by a switching Kalman filter that applies the *correction* and *prediction* steps described by equations (3.14) and (3.15), or equation (3.17), for each mode σ_k, $k \in \{1, 2, ..., N_{\mathrm{m}}\}$. Specifically, for each σ_k, the following *correction* and *prediction* steps are applied.

Measurement update (correction step)

$$\begin{cases} M_k := HP_{k|k-1}H^T + R_k \\ \hat{x}_{k|k} = \hat{x}_{k|k-1} + P_{k|k-1}H^T M_k^{-1}(y_k - H\hat{x}_{k|k-1}) \\ P_{k|k} = P_{k|k-1} - P_{k|k-1}H^T M_k^{-1} HP_{k|k-1}^T \end{cases} \tag{3.25}$$

Time update (prediction step)

$$\begin{cases} \hat{x}_{k+1|k} = A_{\sigma_k}^d \hat{x}_{k|k} + B_{\sigma_k}^d P_k^{in} + E_{\sigma_k}^d x_k^t \\ P_{k+1|k} = A_{\sigma_k}^d P_{k|k} A_{\sigma_k}^d + Q_{\sigma_k}. \end{cases} \tag{3.26}$$

That is, $\hat{x}_{k|k}$ and $P_{k|k}$ are used to estimate x_{k+1} regradless of whether the subgraph dynamics have switched from σ_k to σ_{k+1}. Alternatively, the *prediction* and *correction* steps can be combined into a single step as follows.

$$\begin{cases} M_k := HP_{k|k-1}H^T + R_k \\ K_k = A_{\sigma_k}^d P_{k|k-1}H^T M_k^{-1}, \\ \hat{x}_{k+1|k} = A_{\sigma_k}^d \hat{x}_{k|k-1} + B_{\sigma_k}^d P_k^{in} + E_{\sigma_k}^d x_k^t + K_k(y_k - H\hat{x}_{k|k-1}), \\ P_{k+1|k} = A_{\sigma_k}^d (P_{k|k-1} - P_{k|k-1}H^T M_k^{-1} HP_{k|k-1}^T) A_{\sigma_k}^d + Q_{\sigma_k}, \end{cases} \tag{3.27}$$

Stability and convergence of such an observer are investigated in [87].

3.3 Hierarchical Observer Architecture

The proposed multilevel hierarchical observer consists of multiple local observers connected in a hierarchy to a global observer at the top level. Each observer estimates the dynamics of its corresponding part of the system (i.e. its own subgraph) using its own estimation

algorithm. Low-level observers estimate dynamics at the component/subsystem-level and high-level observers estimate dynamics at the system-level. More specifically, as the level of the hierarchy increases, the part of the system estimated by each local observer increases and only the global observer at top level captures the dynamics of the entire system. Additionally, to reduce the overall computational load, high-level observers use low resolution representations of the models used by low-levels observers such that as the level of the hierarchy increases the orders of the models decrease.

The hierarchy described here is delineated by time scale. That is, as the level of the hierarchy increases the time step of the observers increases such that low-level observers update fast enough to capture the fast dynamics at the component-level and high-level observers update slowly with the dynamics of the system-level models. Local observers operating at the same level in the hierarchy update at the same rate and do not share information. Restricting the flow of information between observers to be only upwards and downwards in the hierarchy can significantly reduce the total communication cost.

Three types of information are shared in the hierarchical observer proposed in this dissertation: sensor measurements, local state estimates, and coupling information estimates (also called disturbance estimates or sink state estimates). At the lowest level of the hierarchy, local observers receive sensor measurements from the physical system and disturbance estimates from next-level observers. At all upper levels in the hierarchy, observers do not have direct access to physical sensor measurements. Instead, they treat local state estimates received from lower-level observers as *pseudo-measurements*. Coupling information is received from upper-level observers since more interactions are naturally included in the model as the level of the hierarchy increases. An example 4-level hierarchical observer is shown in Figure 3.1. The update rates of the observers at Level 1, Level 2, Level 3, and Level 4 are 100s, 10s, 1s, and 0.1s, respectively.

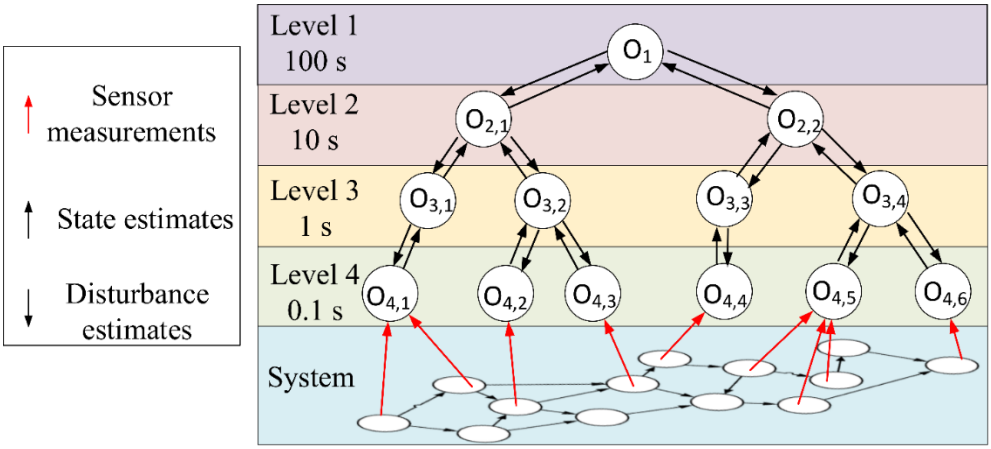

Figure 3.1 An example hierarchical observer of 4 levels. Each local observer estimates its own part of the system using its own estimation algorithm. Observers operating at the same level update at the same rate and do not share information.

3.4 Advantages of Hierarchical Estimation

Compared to the conventional centralized estimation approach which relies on a single observer that accounts for all system's interactions, the proposed hierarchical estimation approach provides the following advantages:

1. *Lower computational complexity:* A centralized estimation approach relies on a single observer to estimate the dynamics of a system. Whereas, a hierarchical observer runs multiple smaller observers in parallel allowing a reduction in the computational cost. This reduction is further enabled by applying appropriate model order reduction at upper levels in the hierarchy such that as the level of the hierarchy increases the orders of the models used decrease.
2. *Flexibility:* The proposed hierarchical estimation framework is flexible in terms of the estimation algorithm used by each observer in the hierarchy. For example, specific nonlinear elements could be handled with nonlinear estimation algorithms (e.g. Extended Kalman filter (EKF), Unscented Kalman filter (UKF), etc.) while leaving the linear elements to be observed by simpler linear estimation algorithms (e.g. Luenberger observer, Kalman filter (KF), etc.).
3. *Robustness:* A hierarchical framework does not suffer from a single point of failure associated with a centralized estimator. Therefore, compared to a centralized

observer, a hierarchical observer can be more robust to failure (e.g. sensor failures).

4. *Modularity:* Adding, removing, or modifying a subsystem can be easily handled in the proposed hierarchical observer. Whereas, these alterations require a complete redesign of the observer in a centralized estimation framework.
5. *Scalability:* The proposed hierarchical estimation approach can be applied to estimate the dynamics of small-scale systems or can be extended to estimate the dynamics of large-scale complex systems. As a result, the proposed hierarchical estimation framework can be directly applied to different systems with various architectures.
6. *Suitable for multiple timescale dynamics:* A centralized observer is designed using a single time step. However, the proposed hierarchical observer consists of a network of local observers updating at different timescales. As a result, the proposed hierarchical observer can be applied to estimate the dynamics of multi-domain dynamical systems.

On the other hand, compared to decentralized estimation [88] and Kalman-filter based hierarchical estimation algorithms [51], [84], [85] where subsystem's interactions are ignored, the proposed hierarchical estimation approach can achieve higher estimation accuracy. This is enabled by a bi-directional flow of information that propagates coupling information between the local observers at all levels of the hierarchy.

3.5 Hierarchical Observer Formulation

This section presents the formulation of the proposed hierarchical estimation approach. As mentioned in section 3.3, the proposed framework is independent of the choice of the estimation algorithm used by each observer in the hierarchy. That is, each observer in the hierarchy can use its own nonlinear estimation algorithm to estimate the nonlinear dynamics of its subgraph given in the form of equation (2.7); or the subgraph dynamics can be linearized and estimated using linear estimation algorithms. The formulation presented in this section is based on the linear Kalman filter algorithm. This is facilitated by the assumption given by equation (3.2).

The remainder of this section is organized as follows. Subsection 3.5.1 presents the formulation of an N-level hierarchical dynamic model derived from the graph-based modeling approach described in Chapter 2. Subsection 3.5.2 presents the formulation of a Kalman filter-based hierarchical estimation algorithm and describes how to modify the hierarchical observer to include different types of observers in the hierarchy.

3.5.1 N-Level Hierarchical Dynamic Model

To design a hierarchical observer, there must be a hierarchical model of the system dynamics. A hierarchical model can be designed by applying the following steps:

1. Design a graph-based model that accurately captures the dynamics of the physical system. To derive the graph dynamics, apply conservation laws on each vertex of the graph as shown in section 2.2. The dynamics of the graph can then be represented by a set of first order differential equations given in the form of equation (2.7). In general, a graph is represented by nonlinear dynamics. However, a linear form can be obtained by individually linearizing each edge of the graph. For example, this can be done by considering a state-affine form for the power flows as shown in equation (3.2).
2. Decompose the graph into a hierarchy of interconnected systems and subsystems. An N-level hierarchical model is defined by a top-level model, $N-2$ intermediate-levels with several models each, and the lowest-level models. This step can be achieved using several system decomposition techniques. For example, section 2.3 describes various methods that can be used to derive a hierarchy from a graph-based model.
3. At all levels of the hierarchy, except for the lowest level, apply the structure-preserving model order reduction technique presented in Chapter 2 (i.e. Algorithm 1 in section 2.4). This step allows a reduction in the computational complexity of the observer.

The formulation of the top-level, intermediate-levels, and lowest-level models is described in 3.5.1.1, 3.5.1.2, and 3.5.1.3, respectively.

3.5.1.1 Top-level Model

The top-level of the hierarchy consists of a single reduced-order graph-based model that represents the dynamics of the entire physical system, and hence it inherently captures all subsystem's interactions. Following steps 1-3 from section 3.5.1, and assuming a state-affine form for the power flows (i.e. equation (3.2)), the top-level model can be represented by

$$\begin{cases} \dot{x}_p = A_p(u_p)x_p + B_p P_p^{in} + E_p(u_p)x_p^t, \\ y_p = H_p x_p + \upsilon_p, \end{cases} \tag{3.28}$$

where

$$A_p(u_p) = -C_p^{-1}\overline{M}_p\overline{F}_p(u_p), \tag{3.29}$$

$$B_p = C_p^{-1}D_p, \tag{3.30}$$

$$E_p(u_p) = -C_p^{-1}\overline{M}_p\underline{F}_p(u_p). \tag{3.31}$$

The subscript p refers to the top-level of the hierarchy. By assuming a zero-order hold for the edge inputs u_p, the source power flows P_p^{in}, and the sink states x_p^t, a discrete representation of the top-level model (3.28) can be written as

$$\begin{cases} x_{k+1,p} = A_{k,p}x_{k,p} + B_{k,p}P_{k,p}^{in} + E_{k,p}x_{k,p}^t, \\ y_{k,p} = H_p x_{k,p} + \upsilon_{k,p} \end{cases} \tag{3.32}$$

where

$$A_{k,p} = e^{A_p\tau_p^s}, \tag{3.33}$$

$$B_{k,p} = A_p^{-1}(A_{k,p} - I)B_p, \tag{3.34}$$

$$E_{k,p} = A_p^{-1}(A_{k,p} - I)E_p, \tag{3.35}$$

and τ_p^s is the sample time of the top-level model. At this level of the hierarchy, the sink states x_p^t represent distrubances that are external to the entire system (e.g. the external environment).

3.5.1.2 Intermediate-levels Models

An N-level hierarchical model consists of $N-2$ intermediate-levels with several subsystem models each. Each of these models is a reduced order representation of models used at lower levels in the hierarchy. By applying steps 1-3 from section 3.5.1, and assuming a state-affine form for the power flows (i.e. equation (3.2)), each susbsytem m of every intermediate level can be represented by

$$\begin{cases} \dot{x}_{n,m} = A_{n,m}(u_{n,m})x_{n,m} + B_{n,m}P_{n,m}^{in} + E_{n,m}(u_{n,m})x_{n,m}^{t} + E_{n,m}^{coup}(u_{n,m})x_{n,m}^{coup}, \\ y_{n,m} = H_{n,m}x_{n,m} + \upsilon_{n,m}, \end{cases} \tag{3.36}$$

where the subscript n refers to the level of the hierarchy, and $x_{n,m}^{coup}$ is a vector of the coupling states. Specifically, the vector $x_{n,m}^{t}$ represents variables that capture the interactions of subsystem m with entities that are external to the entire system not only susbsystem m (e.g. the external environment). Whereas, the vector $x_{n,m}^{coup}$ represents states that capture the interactions of susbsystem m with the neighboring subsystems. Matrices $A_{n,m}(u_{n,m})$, $B_{n,m}$, $E_{n,m}(u_{n,m})$, and $E_{n,m}^{coup}(u_{n,m})$ are given by

$$A_{n,m}(u_{n,m}) = -C_{n,m}^{-1}\overline{M}_{n,m}\overline{F}_{n,m}(u_{n,m}), \tag{3.37}$$

$$B_{n,m} = C_{n,m}^{-1}D_{n,m}, \tag{3.38}$$

$$E_{n,m}(u_{n,m}) = -C_{n,m}^{-1}\overline{M}_{n,m}\underline{F}_{n,m}(u_{n,m}), \tag{3.39}$$

$$E_{n,m}^{coup}(u_{n,m}) = -C_{n,m}^{-1}\overline{M}_{n,m}\underline{F}_{n,m}^{coup}(u_{n,m}), \tag{3.40}$$

by decomposing the power flow vector $P_{n,m}$ of each intermediate level subsystem m into

$$P_{n,m} = \begin{bmatrix} \overline{F}_{n,m}(u_{n,m}) & \underline{F}_{n,m}(u_{n,m}) & \underline{F}_{n,m}^{coup}(u_{n,m}) \end{bmatrix} \begin{bmatrix} x_{n,m} \\ x_{n,m}^{t} \\ x_{n,m}^{coup} \end{bmatrix}, \tag{3.41}$$

where $\overline{F}_{n,m}(u_{n,m}) \in \mathbb{R}^{N_{e,n,m} \times (N_{v,n,m} - N_{s,n,m} - N_{coup,n,m})}$ is a map for the internal states $x_{n,m}$, $\underline{F}_{n,m}(u_{n,m}) \in \mathbb{R}^{N_{e,n,m} \times N_{s,n,m}}$ is a map for the external sink states $x^t_{n,m}$, and $\underline{F}^{coup}_{n,m}(u_{n,m}) \in \mathbb{R}^{N_{e,n,m} \times N_{coup,n,m}}$ is a map for the coupling states $x^{coup}_{n,m}$. $N_{e,n,m}$ is the number of edges (i.e. $e_{n,m}$), $N_{v,n,m}$ is the number of vertices (i.e. $x_{n,m}$, $x^t_{n,m}$, and $x^{coup}_{n,m}$), $N_{s,n,m}$ is the number of external sink vertices (i.e. $x^t_{n,m}$), and $N_{coup,n,m}$ is the number of coupling vertices (i.e. $x^{coup}_{n,m}$) of subsystem m at intermediate level n.

By assuming a zero-order hold for the edge inputs $u_{n,m}$, the source power flows $P^{in}_{n,m}$, the coupling states $x^{coup}_{n,m}$, and the external sink states $x^t_{n,m}$, a discrete representation of each subsystem model m given by (3.36) can be written as

$$\begin{cases} x_{k+1,n,m} = A_{k,n,m} x_{k,n,m} + B_{k,n,m} P^{in}_{k,n,m} + E_{k,n,m} x^t_{k,n,m} + E^{coup}_{k,n,m} x^{coup}_{k,n,m}, \\ y_{k,n,m} = H_{n,m} x_{k,n,m} + \upsilon_{k,n,m} \end{cases} \tag{3.42}$$

where

$$A_{k,n,m} = e^{A_{n,m} \tau^s_{n,m}}, \tag{3.43}$$

$$B_{k,n,m} = A^{-1}_{n,m} (A_{k,n,m} - I) B_{n,m}, \tag{3.44}$$

$$E_{k,n,m} = A^{-1}_{n,m} (A_{k,n,m} - I) E_{n,m}, \tag{3.45}$$

$$E^{coup}_{k,n,m} = A^{-1}_{n,m} (A_{k,n,m} - I) E^{coup}_{n,m}. \tag{3.46}$$

3.5.1.3 Low-level Models

Following steps 1-3 from section 3.5.1, and assuming a state-affine form for the power flows (i.e. equation (3.2)), each subsystem w at the lowest level of the hierarchy is given by

$$\begin{cases} \dot{x}_w = A_w(u_w) x_w + B_w P^{in}_w + E_w(u_w) x^t_w + E^{coup}_w(u_w) x^{coup}_w, \\ y_w = H_w x_w + \upsilon_w, \end{cases} \tag{3.47}$$

where x_w^t captures the coupling of subsystem w with entities that are external to the entire system (e.g. the environment), and x_w^{coup} captures the interactions of subsystem w with the neighboring subsystems. As described in section 3.3, model order reduction is not applied at the lowest level of the hierarchy. That is, each subsystem w is represented by a full order graph-based model. Matrices $A_w(u_w)$, B_w, $E_w(u_w)$, and $E_w^{coup}(u_w)$ are given by

$$A_w(u_w) = -C_w^{-1}\overline{M}_w\overline{F}_w(u_w), \tag{3.48}$$

$$B_w = C_w^{-1}D_w, \tag{3.49}$$

$$E_w(u_w) = -C_w^{-1}\overline{M}_w\underline{F}_w(u_w), \tag{3.50}$$

$$E_w^{coup}(u_w) = -C_w^{-1}\overline{M}_w\underline{F}_w^{coup}(u_w), \tag{3.51}$$

by decomposing the power flow vector P_w of each subsystem w into

$$P_w = \begin{bmatrix} \overline{F}_w(u_w) & \underline{F}_w(u_w) & \underline{F}_w^{coup}(u_w) \end{bmatrix} \begin{bmatrix} x_w \\ x_w^t \\ x_w^{coup} \end{bmatrix}, \tag{3.52}$$

where $\overline{F}_w(u) \in \mathbb{R}^{N_{e,w} \times (N_{v,w} - N_{s,w} - N_{coup,w})}$ is a map for the internal states x_w, $\underline{F}_w(u_w) \in \mathbb{R}^{N_{e,w} \times N_{s,w}}$ is a map for the external sink states x_w^t, and $\underline{F}_w^{coup}(u_w) \in \mathbb{R}^{N_{e,w} \times N_{coup,w}}$ is a map for the coupling states x_w^{coup}. $N_{e,w}$, $N_{v,w}$, $N_{s,w}$, and $N_{coup,w}$ are the numbers of edges (i.e. e_w), vertices (i.e. x_w, x_w^t, and x_w^{coup}), external sink vertices (i.e. x_w^t), and coupling vertices (i.e. x_w^{coup}) of subsystem w, respectively.

By assuming a zero-order hold for the edge inputs u_w, the source power flows P_w^{in}, the coupling states x_w^{coup}, and the sink states x_w^t, a discrete representation of each lowest-level subsystem model can be written as

$$\begin{cases} x_{k+1,w} = A_{k,w}x_{k,w} + B_{k,w}P^{in}_{k,w} + E_{k,w}x^{t}_{k,w} + E^{coup}_{k,w}x^{coup}_{k,w}, \\ y_{k,w} = H_w x_{k,w} + \upsilon_{k,w} \end{cases} \tag{3.53}$$

where

$$A_{k,w} = e^{A_w \tau^s_w}, \tag{3.54}$$

$$B_{k,w} = A_w^{-1}(A_{k,w} - I)B_w, \tag{3.55}$$

$$E_{k,w} = A_w^{-1}(A_{k,w} - I)E_w, \tag{3.56}$$

$$E^{coup}_{k,w} = A_w^{-1}(A_{k,w} - I)E^{coup}_w. \tag{3.57}$$

Remarks:

a) The top-level model (i.e. equation (3.28)) does not include a term that explicitly accounts for coupling between subsystems since all subsystem interactions are inherently captured in this model.

b) Except for the models at the lowest level of the hierarchy, each model in the hierarchical network is a reduced order comibation of models at the immediate lower level in the hierarchy

3.5.2 KF-Based Hierarchical Estimation Algorithm

This section presents the formulation of a Kalman filter-based hierarchical estimation algorithm. That is, at each level of the hierarchy, each observer is designed as a Kalman filter.

3.5.2.1 Top-level Observer

Using the top-level graph-based model described in 3.5.1.1, the top-level observer can be designed as

$$\begin{cases} M_{k,p} \coloneqq H_p P_{k|k-1,p} H_p^T + R_{k,p}, \\ K_{k,p} = A_{k,p} P_{k|k-1,p} H_p^T M_{k,p}^{-1}, \\ \hat{x}_{k+1|k,p} = A_{k,p} \hat{x}_{k|k-1,p} + B_{k,p} P_{k,p}^{in} + E_{k,p} x_{k,p}^t + K_{k,p}(H_p \hat{x}_{k,p}^l - H_p \hat{x}_{k|k-1,p}), \\ P_{k+1|k,p} = A_{k,p}(P_{k|k-1,p} - P_{k|k-1,p} H_p^T M_{k,p}^{-1} H_p P_{k|k-1,p}^T) A_{k,p}^T + Q_{k,p}. \end{cases} \tag{3.58}$$

Since the top-level observer does not have access to physical sensor measurements, y, and treats local state estimates received from lower level observers as *pseudo-measurements,* the innovation term $y_k - H\hat{x}_{k|k-1}$ from equation (3.17) is replaced by $H_p \hat{x}_{k,p}^l - H_p \hat{x}_{k|k-1,p}$, where $\hat{x}_{k,p}^l$ represents the local state estimates at time k sent to the top-level observer from local observers at the immediate lower level in the hierarchy.

3.5.2.2 Intermediate-levels Observers

Using the intermediate-levels models described in 3.5.1.2, each observer of subsystem m at intermediate level n can be designed as

$$\begin{cases} M_{k,n,m} \coloneqq H_{n,m} P_{k|k-1,n,m} H_{n,m}^T + R_{k,n,m} \\ K_{k,n,m} = A_{k,n,m} P_{k|k-1,n,m} H_{n,m}^T M_{k,n,m}^{-1}, \\ \hat{x}_{k+1|k,n,m} = A_{k,n,m} \hat{x}_{k|k-1,n,m} + B_{k,n,m} P_{k,n,m}^{in} + E_{k,n,m} x_{k,n,m}^t \\ \qquad\qquad + K_{k,n,m}(H_{n,m} \hat{x}_{k,n,m}^l - H_{n,m} \hat{x}_{k|k-1,n,m}) + E_{k,n,m}^{coup} \hat{x}_{k,n,m}^{coup}, \\ P_{k+1|k,n,m} = A_{k,n,m}(P_{k|k-1,n,m} - P_{k|k-1,n,m} H_{n,m}^T M_{k,n,m}^{-1} H_{n,m} P_{k|k-1,n,m}^T) A_{k,n,m}^T + Q_{k,n,m}. \end{cases} \tag{3.59}$$

That is, similarly to the top-level observer (i.e. equation (3.58)), intermediate-levels observers do not have access to physical sensor measurements. Instead, they receive *pseudo-measurements* (i.e. local state estimates) from lower-level observers. Consequently, the innovation term $y_k - H\hat{x}_{k|k-1}$ from (3.17) is replaced by $H_{n,m} \hat{x}_{k,n,m}^l - H_{n,m} \hat{x}_{k|k-1,n,m}$ in equation (3.59), where $\hat{x}_{k,n,m}^l$ represents local state estimates at time k sent to intermediate-level observer m from local observers at the immediate lower level in the hierarchy. Additionally, the term $E_{k,n,m}^{coup} \hat{x}_{k,n,m}^{coup}$ represents the coupling state estimate vector received by observer m from observers at the immediate upper level in the hierarchy.

3.5.2.3 Lowest-level Observers

Using the lowest-level models described in section 3.5.1.3, each observer at the lowest level of the hierarchy can be designed as

$$\begin{cases} M_{k,w} := H_w P_{k|k-1,w} H_w^T + R_{k,w} \\ K_{k,w} = A_{k,w} P_{k|k-1,w} H_w^T M_{k,w}^{-1}, \\ \hat{x}_{k+1|k,w} = A_{k,w}\hat{x}_{k|k-1,w} + B_{k,w}P_{k,w}^{in} + E_{k,w}x_{k,w}^{t} \\ \qquad\qquad + K_{k,w}(y_{k,w} - H_w\hat{x}_{k|k-1,w}) + E_{k,w}^{coup}\hat{x}_{k,w}^{coup}, \\ P_{k+1|k,w} = A_{k,w}(P_{k|k-1,w} - P_{k|k-1,w}H_w^T M_{k,w}^{-1} H_w P_{k|k-1,w}^T)A_{k,w}^T + Q_{k,w}, \end{cases} \tag{3.60}$$

where $E_{k,w}^{coup}\hat{x}_{k,w}^{coup}$ represents the coupling state estimates vector received by observer w from upper-level observers. As shown by the innovation term, $y_{k,w} - H_w\hat{x}_{k|k-1,w}$, the lowest-level observers have direct access to physical sensor measurements, y_k.

Remarks:

1) $\tau_p^s > \tau_{n1}^s > \tau_{n2}^s > ... > \tau_w^s$, i.e. the update rates of the observers increase as the level of the hierarchy decreases. The subscripts $n1, n2$, refers to two different intermediate levels with level $n1$ being higher than level $n2$. Additionally, observers at the same level update at the same rate.
2) At instances when observers at different levels are due to update, it is assumed that lower level observers update first. This can be achieved by delaying the update of upper level observers until after lower level observers update.
3) The process and measurement noise covariance matrices, Q_k and R_k, can be used as tuning parameters.
4) It is assumed that the source power flows, $P_{k,p}^{in}$, $P_{k,n,m}^{in}$, and $P_{k,w}^{in}$, and the sink states $x_{k,p}^{t}$, $x_{k,n,m}^{t}$, and $x_{k,w}^{t}$ are known (i.e. measurable) variables and the coupling terms $x_{k,n,m}^{coup}$ and $x_{k,w}^{coup}$ are unknown but estimated by $\hat{x}_{k,n,m}^{coup}$ and $\hat{x}_{k,w}^{coup}$ via observers at the immediate upper level in the hierarchy.

5) Top-level and intermediate-level observers estimate reduced-order representations of the full-order graph-based models used at the lowest level of the hierarchy. The main goal of these observers is to estimate the complex dynamic interactions between the different susbsystems by capturing system-level dynamics.

3.5.2.4 Hierarchical Observer with Several Estimation Algorithms

The proposed estimation framework is modular and flexible in terms of the estimation algorithm used by each observer in the hierarchy. Therefore, depending on the class of systems estimated by each observer in the hierarchy, the hierarchical observer can be designed as a combination of several estimation algorithms (e.g. linear, nonlinear, switching, non-switching, etc.). For example, discrete actuators such as valves and switches are essential components in electrified vehicles. To capture switching dynamics of discrete actuators, a switching observer is needed. This can be directly captured in the hierarchy by simply designing the local observer responsible for estimating switching dynamics as a switching observer (e.g. equation (3.27)). However, that switching observer should be designed to receive coupling information from upper level observers and pseudo-measurements or measurements from lower-level observers or physical sensors, depending on its level in the hierarchy.

3.5.3 Stability Analysis

The stability properties of the proposed hierarchical estimation framework are explored in this section. The authors in [88] investigate the boundedness and convergence of a distributed estimation framework designed by connecting a set of decentralized observers together via a communication network. The distributed estimation framework proposed in [88] is independent of the estimation algorithm used by each observer in the network, and thus the stability analysis presented in [88] can provide a basis for the stability and convergence of the framework proposed in this dissertation. Nevertheless, there are several major differences between the two approaches that should be considered in the derivation of the stability bounds of the proposed hierarchical observer:

1) Coupling information: the distributed estimation framework presented in [88] is based on the assumption that a decentralized estimation network that ignores coupling between subsystems already exists. To account for the coupling, each

decentralized observer in the network is connected to a compensator. The combination of a decentralized observer and a compensator is called an augmented observer. Distributed estimation is then achieved by a network of augmented observers that communicate with each other through their compensators. Additionally, each compensator requires the evaluation of a pseudo-inverse at every sampling time. However, depending on the available measurements for each observer, the pseudo-inverse may lead to ill-conditioned matrices. To overcome ill-conditioning, the sample time of the observers needs to be sufficiently small. These constraints do not exist in the proposed hierarchical estimation framework since coupling information is directly shared between the observers at all levels of the hierarchy. In other words, the bidirectional flow of information designed in the proposed hierarchical estimation framework eliminates the need for compensators. As a result, the proposed hierarchical estimation framework is less restrictive in terms of the choice of the update rates of the observers in the hierarchy. This allows the user to design large update rates for high-level observers in the hierarchy without creating ill-conditioned matrices.

2) Single versus multiple update rates: The distributed estimation framework presented in [88] is designed to update at a single rate. That is, all observers in the network send and receive information at the same rate. In contrast, the proposed hierarchical estimation framework includes observers updating at different rates. As a result, the stability analysis of the proposed hierarchical estimation framework should consider the errors introduced by sharing and receiving information between the observers at multiple update rates.

3) Sensor measurements versus pseudo-measurements: In the distributed estimation framework presented in [88], every local observer has direct access to physical sensor measurements. Whereas, in the proposed framework, only local observers at the lowest level of the hierarchy have direct access to sensor readings, and every other observer in the network receives pseudo-measurements from local observers at the level in the hierarchy that is

immediately below. Therefore, the stability analysis of the proposed hierarchical estimation framework should consider the errors introduced by replacing sensor readings by local state estimates (i.e. pseudo-measurements) at upper levels in the hierarchy.

To prove the stability of the proposed hierarchical observer, the following assumptions are used.

Assumption 1: states x, source inputs P^{in}, sink states x^t, edge inputs u, unknown disturbances d introduced from the model order reduction errors, and sensor noise υ of each graph at each level of the hierarchy are assumed to be bounded. That is, in equations (3.32), (3.42), and (3.53),

$$\begin{aligned} &x_p \in \mathcal{X}_p, \\ &x_{n,m} \in \mathcal{X}_{n,m}, \\ &x_w \in \mathcal{X}_w, \end{aligned} \tag{3.61}$$

$$\begin{aligned} &P_p^{in} \in \mathcal{P}_p^{in}, \\ &P_{n,m}^{in} \in \mathcal{P}_{n,m}^{in}, \\ &P_w^{in} \in \mathcal{P}_w^{in}, \end{aligned} \tag{3.62}$$

$$\begin{aligned} &x_p^t \in \mathcal{X}_p^t, \\ &x_{n,m}^t \in \mathcal{X}_{n,m}^t, \\ &x_w^t \in \mathcal{X}_w^t, \end{aligned} \tag{3.63}$$

$$\begin{aligned} &u_p \in \mathcal{U}_p, \\ &u_{n,m} \in \mathcal{U}_{n,m}, \\ &u_w \in \mathcal{U}_w, \end{aligned} \tag{3.64}$$

$$\begin{aligned} &\upsilon_p \in \mathcal{V}_p, \\ &\upsilon_{n,m} \in \mathcal{V}_{n,m}, \\ &\upsilon_w \in \mathcal{V}_w, \end{aligned} \tag{3.65}$$

$$
\begin{aligned}
d_p &\in \mathcal{D}_p, \\
d_{n,m} &\in \mathcal{D}_{n,m},
\end{aligned}
\tag{3.66}
$$

where

$$
\begin{aligned}
\mathcal{P}_p^{in} &:= \{P_p^{in} \in \mathbb{R}^{N_{l_p}} \quad s.t.\ \left|P_p^{in}\right| \le \overline{P_p^{in}},\ \overline{P_p^{in}} > 0\}, \\
\mathcal{P}_{n,m}^{in} &:= \{P_{n,m}^{in} \in \mathbb{R}^{N_{l_{n,m}}} \quad s.t.\ \left|P_{n,m}^{in}\right| \le \overline{P_{n,m}^{in}},\ \overline{P_{n,m}^{in}} > 0\}, \\
\mathcal{P}_w^{in} &:= \{P_w^{in} \in \mathbb{R}^{N_{l_w}} \quad s.t.\ \left|P_w^{in}\right| \le \overline{P_w^{in}},\ \overline{P_w^{in}} > 0\},
\end{aligned}
\tag{3.67}
$$

$$
\begin{aligned}
\mathcal{U}_p &:= \{u_p \in \mathbb{R}^{N_{u_p}} \quad s.t.\ \left|u_p\right| \le \overline{u_p},\ \overline{u_p} > 0\}, \\
\mathcal{U}_{n,m} &:= \{u_{n,m} \in \mathbb{R}^{N_{u_{n,m}}} \quad s.t.\ \left|u_{n,m}\right| \le \overline{u_{n,m}},\ \overline{u_{n,m}} > 0\}, \\
\mathcal{U}_w &:= \{u_w \in \mathbb{R}^{N_{u_w}} \quad s.t.\ \left|u_w\right| \le \overline{u_w},\ \overline{u_w} > 0\},
\end{aligned}
\tag{3.68}
$$

$$
\begin{aligned}
\mathcal{V}_p &:= \{\upsilon_p \in \mathbb{R}^{N_{y_p}} \quad s.t.\ \left|\upsilon_p\right| \le \overline{\upsilon_p},\ \overline{\upsilon_p} > 0\}, \\
\mathcal{V}_{n,m} &:= \{\upsilon_{n,m} \in \mathbb{R}^{N_{y_{n,m}}} \quad s.t.\ \left|\upsilon_{n,m}\right| \le \overline{\upsilon_{n,m}},\ \overline{\upsilon_{n,m}} > 0\}, \\
\mathcal{V}_w &:= \{\upsilon_w \in \mathbb{R}^{N_{y_w}} \quad s.t.\ \left|\upsilon_w\right| \le \overline{\upsilon_w},\ \overline{\upsilon_w} > 0\},
\end{aligned}
\tag{3.69}
$$

$$
\begin{aligned}
\mathcal{D}_p &:= \{d_p \in \mathbb{R}^{N_{v_p}} \quad s.t.\ \left|d_p\right| \le \overline{d_p},\ \overline{d_p} > 0\}, \\
\mathcal{D}_{n,m} &:= \{d_{n,m} \in \mathbb{R}^{N_{v_{n,m}}} \quad s.t.\ \left|d_{n,m}\right| \le \overline{d_{n,m}},\ \overline{d_{n,m}} > 0\},
\end{aligned}
\tag{3.70}
$$

$\mathcal{X}_p$, $\mathcal{X}_{n,m}$, $\mathcal{X}_w$, $\mathcal{X}_p^t$, $\mathcal{X}_{n,m}^t$, and $\mathcal{X}_w^t$ are compact sets, N_{l_p}, $N_{l_{n,m}}$, and N_{l_w} are the numbers of source inputs, N_{u_p}, $N_{u_{n,m}}$, and N_{u_w} are the numbers of edge inputs, and N_{y_p}, $N_{y_{n,m}}$, and N_{y_w} are the numbers of sensors of top-level, intermediate-levels, and lowest-level observers, respectively. N_{v_p}, and $N_{v_{n,m}}$ are the number of vertices of the top-level and intermediate-level models. The bounds $\overline{P_p^{in}}$, $\overline{P_{n,m}^{in}}$, $\overline{P_w^{in}}$, $\overline{u_p}$, $\overline{u_{n,m}}$, $\overline{u_w}$, $\overline{\upsilon_p}$, $\overline{\upsilon_{n,m}}$, $\overline{\upsilon_w}$, $\overline{d_p}$, and $\overline{d_{n,m}}$ are known scalars. The unknown disturbance vectors (i.e. d_p and $d_{n,m}$) represent model order reduction errors. Since full-order models are used at the lowest level, these disturbances only

affect intermediate and top levels of the hierarchy. *Assumption 1* implies that the systems considered are stable. A shown in [62], the open-loop stablity of the class of system considered in this chapter can be proved under appropriate conditions on the connectivity of the graph-based model and the current form of the equations governing power flow along its edges (i.e. equation (3.2)).

Definition 1: let $G(\hat{x}_{k|k-1}, P_k^{in}, x_k^t, y_k)$ be defined as

$$G(\hat{x}_{k|k-1}, P_k^{in}, x_k^t, y_k) \coloneqq D_k + K_k(y_k - H\hat{x}_{k|k-1}), \tag{3.71}$$

where

$$D_k \coloneqq A_k\hat{x}_{k|k-1} + B_k P_k^{in} + E_k x_k^t. \tag{3.72}$$

In other words, $G(\hat{x}_{k|k-1}, P_k^{in}, x_k^t, y_k)$ is a compact form of a discrete-time Kalman filter, where K_k is the Kalman gain matrix.

Definition 2: $\alpha(.) \coloneqq \beta(., \tau^d)$ is a class K function. $f(\bar{u})$ is a constant function representing an upper bound on the Frobenius norm of $\left\|E_k^{coup}\right\|$ (i.e. $\left\|E_{k,p}^{coup}\right\| \leq f_p(\bar{u}_p)$). The estimation error of an observer i is defined as $e_{k+1,i} \coloneqq \hat{x}_{k+1|k,i} - x_{k+1,i}$. $\mathbb{I}_i^u$ and $\mathbb{I}_i^l$ are the set of upper-level and lower-level observer indices with which observer i interacts, respectively. For example, if observer i receives coupling state estimates from observers 2 and 3 at the upper level and pseudo-measurements (i.e. local state estimates) from observers 1 and 3 at the lower level in the hierarchy, then $\mathbb{I}_i^u = \{2,3\}$ and $\mathbb{I}_i^l = \{1,3\}$.

Assumption 2: For the top-level observer, the following inequality holds,

$$\begin{aligned}\left|G_p(\hat{x}_{k|k-1,p}, P_{k,p}^{in}, x_{k,p}^t, y_{k,p}) - x_{k+1,p}\right| \leq \beta_p\left(\left|z_{0,p} - x_{0,p}\right|, t_k - t_0\right) + \phi_p\left(\max_{\tau}\left|\upsilon(\tau)\right|\right) \\ + \zeta_p\left(\max_{\tau}\left|d_p(\tau)\right|\right).\end{aligned} \tag{3.73}$$

Assumption 3: For each intermediate-level observer, the following holds,

$$\left|G_{n,m}(\hat{x}_{k|k-1,n,m}, P^{in}_{k,n,m}, x^{t}_{k,n,m}, y_{k,n,m}) + E^{coup}_{k,n,m} x^{coup}_{k,n,m} - x_{k+1,n,m}\right| \leq$$
$$\beta_{n,m}\left(\left|z_{0,n,m} - x_{0,n,m}\right|, t_k - t_0\right) + \phi_{n,m}\left(\max_{\tau}\left|\upsilon(\tau)\right|\right) + \zeta_{n,m}\left(\max_{\tau}\left|d_{n,m}(\tau)\right|\right). \tag{3.74}$$

Assumption 4: For each lowest-level observer, the following holds,

$$\left|G_{w}(\hat{x}_{k|k-1,w}, P^{in}_{k,w}, x^{t}_{k,w}, y_{k,w}) + E^{coup}_{k,w} x^{coup}_{k,w} - x_{k+1,w}\right| \leq$$
$$\beta_{w}\left(\left|z_{0,w} - x_{0,w}\right|, t_k - t_0\right) + \phi_{w}\left(\max_{\tau}\left|\upsilon(\tau)\right|\right). \tag{3.75}$$

β_p, $\beta_{n,m}$, and β_w are class KL functions and ϕ_p, $\phi_{n,m}$, ϕ_w, ζ_p, and $\zeta_{n,m}$ are class K functions. Equations (3.73)-(3.75) characterize the boundedness and convergence of each observer in the hierarchy when actual coupling information $E^{coup}_{k,i} x^{coup}_{k,i}$ and physical sensor measurements $y_{k,i}$ are available. Assumptions 2-4 can be easily satisfied since when actual coupling information and actual sensor measurements are available, each observer in the hierarchy will be equivalent to a centralized observer (i.e. centralized Kalman filter) and thus asymptotic convergence can be achieved under appropriate detectability (or observability) conditions.

Assumption 5:

$$\begin{aligned} K_{k,p} &\leq \mathcal{K}_p, \\ K_{k,n,m} &\leq \mathcal{K}_{n,m}, \\ K_{k,w} &\leq \mathcal{K}_w, \end{aligned} \tag{3.76}$$

where $\mathcal{K}_p$, $\mathcal{K}_{n,m}$, and $\mathcal{K}_w$ are positive constants.

Proposition 1: If *assumptions 1-5* are satisfied, then the estimation error of

a) the top-level observer is bounded by

$$\left|e_{k+1,p}\right| \leq \alpha_p\left(\left|e_{k,p}\right|\right) + \phi_p\left(\max_{\tau}\left|\upsilon(\tau)\right|\right) + \zeta_p\left(\max_{\tau}\left|d_p(\tau)\right|\right) + \mathcal{K}_p \sum_{l \in \mathbb{I}^{l}_{p}} \left|e_{k,l}\right|, \tag{3.77}$$

b) each intermediate-level observer is bounded by

$$\begin{aligned}\left|e_{k+1,n,m}\right| \le \alpha_{n,m}\left(\left|e_{k,n,m}\right|\right) + \phi_{n,m}\left(\max_{\tau}\left|\upsilon(\tau)\right|\right) + \zeta_{n,m}\left(\max_{\tau}\left|d_{n,m}(\tau)\right|\right) \\ + \mathcal{K}_{n,m}\sum_{l\in\mathbb{I}^{l}_{n,b}}\left|e_{k,l}\right| + f_{n,m}(\bar{u}_{n,m})\sum_{h\in\mathbb{I}^{u}_{n,m}}\left|e_{k,u}\right|,\end{aligned} \tag{3.78}$$

c) each observer at the lowest level of the hierarchy is bounded by

$$\left|e_{k+1,w}\right| \le \alpha_{w}\left(\left|e_{k,w}\right|\right) + \phi_{w}\left(\max_{\tau}\left|\upsilon(\tau)\right|\right) + f_{w}(\bar{u}_{w})\sum_{h\in\mathbb{I}^{u}_{w}}\left|e_{k,u}\right|. \tag{3.79}$$

Proof

Equation (3.77) is derived as follows. Using *Definition 1*, *Definition 2*, and equation (3.58), the estimation error of the top-level observer can be written as

$$\begin{aligned}e_{k+1,p} &= \hat{x}_{k+1|k,p} - x_{k+1,p} \\ &= D_{k,p} + K_{k,p}(H_p\hat{x}^{l}_{k,p} - H_p\hat{x}_{k|k-1,p}) - x_{k+1,p} \\ &= G_p(\hat{x}_{k|k-1,p}, P^{in}_{k,p}, x^{t}_{k,p}, y_{k,p}) - x_{k+1,p} - K_{k,p}(y_{k,p} - H_p\hat{x}^{l}_{k,p}),\end{aligned} \tag{3.80}$$

Using the triangular inequality, equation (3.80) can be bounded by

$$\left|e_{k+1,p}\right| \le \left|G_p(\hat{x}_{k|k-1,p}, P^{in}_{k,p}, x^{t}_{k,p}, y_{k,p}) - x_{k+1,p}\right| + \left|K_{k,p}(y_{k,p} - H_p\hat{x}^{l}_{k,p})\right| \tag{3.81}$$

Using *Assumptions 1*,*2*, and *5* in addition to the triangular inequality, equation (3.81) can be bounded by

$$\begin{aligned}\left|e_{k+1,p}\right| \le \beta_p\left(\left|z_{0,p} - x_{0,p}\right|, t_k - t_0\right) + \phi_p\left(\max_{\tau}\left|\upsilon_p(\tau)\right|\right) \\ + \zeta_p\left(\max_{\tau}\left|d_p(\tau)\right|\right) + \mathcal{K}_p\sum_{l\in\mathbb{I}^{l}_{p}}\left|e_{k,l}\right|\end{aligned} \tag{3.82}$$

Therefore, over one sample time τ^{s}_{p}, and if t_k and $\left|e_{k,p}\right|$ are considered as the initial time and the initial condition for the estimation error, equation (3.82) can be written as

$$\begin{aligned}\left|e_{k+1,p}\right| \le \alpha_p\left(\left|e_{k,p}\right|\right) + \phi_p\left(\max_{\tau}\left|\upsilon_p(\tau)\right|\right) \\ + \zeta_p\left(\max_{\tau}\left|d_p(\tau)\right|\right) + \mathcal{K}_p \sum_{l\in\mathbb{I}_p^l}\left|e_{k,l}\right|. \qquad \square\end{aligned} \tag{3.83}$$

Similarly, using *Assumptions 1, 3,* and *5,* the upper bound of equation (3.78) is calculated as follows.

$$\begin{aligned}e_{k+1,n,m} &= \hat{x}_{k+1|k,n,m} - x_{k+1} \\ &= G_{k,n,m}(\hat{x}_{k|k-1,n,m}, P^{in}_{k,n,m}, x^{t}_{k,n,m}, y_{k,n,m}) - x_{k+1} \\ &\quad - K_{k,n,m}(y_{k,n,m} - H_{n,m}\hat{x}^{l}_{k,n,m}) + E^{coup}_{k,n,m}\hat{x}^{coup}_{k,n,m},\end{aligned} \tag{3.84}$$

Assumption 1 implies that $x^{coup}_{n,m}$ is bounded since the states x of each subsystem at each level of the hierarchy are bounded. Therefore, the term $E^{coup}_{k,n,m}x^{coup}_{k,n,m}$ can be added to and subtracted from equation (3.84) as follows.

$$\begin{aligned}e_{k+1,n,m} &= \hat{x}_{k+1|k,n,m} - x_{k+1} \\ &= G_{k,n,m}(\hat{x}_{k|k-1,n,m}, P^{in}_{k,n,m}, x^{t}_{k,n,m}, y_{k,n,m}) - x_{k+1} \\ &\quad - K_{k,n,m}(y_{k,n,m} - H_{n,m}\hat{x}^{l}_{k,n,m}) + E^{coup}_{k,n,m}\hat{x}^{coup}_{k,n,m} \\ &\quad + E^{coup}_{k,n,m}x^{coup}_{k,n,m} - E^{coup}_{k,n,m}x^{coup}_{k,n,m},\end{aligned} \tag{3.85}$$

Next, following the same procedure used to derive the upper bound of equation (3.77), the following upper bound can be derived for equation (3.78).

$$\begin{aligned}\left|e_{k+1,n,m}\right| \le \left|G_{k,n,m}(\hat{x}_{k|k-1,n,m}, P^{in}_{k,n,m}, x^{t}_{k,n,m}, y_{k,n,m}) + E^{coup}_{k,n,m}x^{coup}_{k,n,m} - x_{k+1}\right| \\ + \left|E^{coup}_{k,n,m}\hat{x}^{coup}_{k,n,m} - E^{coup}_{k,n,m}x^{coup}_{k,n,m}\right| + \left|K_{k,n,m}(y_{k,n,m} - H_{n,m}\hat{x}^{l}_{k,n,m})\right|,\end{aligned} \tag{3.86}$$

$$\begin{aligned}\left|e_{k+1,n,m}\right| \le \beta_{n,m}\left(\left|z_{0,n,m} - x_{0,n,m}\right|, t_k - t_0\right) + \phi_{n,m}\left(\max_{\tau}\left|\upsilon(\tau)\right|\right) + \zeta_{n,m}\left(\max_{\tau}\left|d_{n,m}(\tau)\right|\right) \\ + \left\|E^{coup}_{k,n,m}\right\|\left|\hat{x}^{coup}_{k,n,m} - x^{coup}_{k,n,m}\right| + \left\|K_{k,n,m}\right\|\left|y_{k,n,m} - H_{n,m}\hat{x}^{l}_{k,n,m}\right|,\end{aligned} \tag{3.87}$$

$$\left|e_{k+1,n,m}\right| \le \beta_{n,m}\left(\left|z_{0,n,m}-x_{0,n,m}\right|, t_k - t_0\right) + \phi_{n,m}\left(\max_{\tau}\left|\upsilon(\tau)\right|\right) + \zeta_{n,m}\left(\max_{\tau}\left|d_{n,m}(\tau)\right|\right) + f_{n,m}\left(\bar{u}_{n,m}\right)\sum_{h\in\mathbb{I}^{u}_{n,m}}\left|e_{k,u}\right| + \mathcal{K}_{n,m}\sum_{l\in\mathbb{I}^{l}_{n,m}}\left|e_{k,l}\right|, \tag{3.88}$$

$$\left|e_{k+1,n,m}\right| \le \alpha_{n,m}\left(\left|e_{k,n,m}\right|\right) + \phi_{n,m}\left(\max_{\tau}\left|\upsilon(\tau)\right|\right) + \zeta_{n,m}\left(\max_{\tau}\left|d_{n,m}(\tau)\right|\right) + \mathcal{K}_{n,m}\sum_{l\in\mathbb{I}^{l}_{n,m}}\left|e_{k,l}\right| + f_{n,m}(\bar{u}_{n,m})\sum_{h\in\mathbb{I}^{u}_{n,m}}\left|e_{k,u}\right|. \quad \square \tag{3.89}$$

Finally, using *Assumptions 1*, *4*, and *5*, the upper bound of equation (3.79) is derived as follows.

$$\begin{aligned} e_{k+1,w} &= \hat{x}_{k+1|k,w} - x_{k+1} \\ &= G_{k,w}(\hat{x}_{k|k-1,w}, P^{in}_{k,w}, x^{t}_{k,w}, y_{k,w}) + E^{coup}_{k,w}\hat{x}^{coup}_{k,w} - x_{k+1} \\ &= G_{k,w}(\hat{x}_{k|k-1,w}, P^{in}_{k,w}, x^{t}_{k,w}, y_{k,w}) + E^{coup}_{k,w}\hat{x}^{coup}_{k,w} - x_{k+1} \\ &\quad + E^{coup}_{k,w}x^{coup}_{k,w} - E^{coup}_{k,w}x^{coup}_{k,w}, \end{aligned} \tag{3.90}$$

$$\begin{aligned} \left|e_{k+1,w}\right| &\le \left|G_{k,w}(\hat{x}_{k|k-1,w}, P^{in}_{k,w}, x^{t}_{k,w}, y_{k,w}) + E^{coup}_{k,w}x^{coup}_{k,w} - x_{k+1}\right| \\ &\quad + \left|E^{coup}_{k,w}\hat{x}^{coup}_{k,w} - E^{coup}_{k,w}x^{coup}_{k,w}\right|, \end{aligned} \tag{3.91}$$

$$\begin{aligned} \left|e_{k+1,w}\right| &\le \beta_{w}\left(\left|z_{0,w}-x_{0,w}\right|, t_k - t_0\right) + \phi_{w}\left(\max_{\tau}\left|\upsilon(\tau)\right|\right) \\ &\quad + \left\|E^{coup}_{k,w}\right\|\left|\hat{x}^{coup}_{k,w} - x^{coup}_{k,w}\right|, \end{aligned} \tag{3.92}$$

$$\begin{aligned} \left|e_{k+1,w}\right| &\le \beta_{w}\left(\left|z_{0,w}-x_{0,w}\right|, t_k - t_0\right) + \phi_{w}\left(\max_{\tau}\left|\upsilon(\tau)\right|\right) \\ &\quad + f_{w}\left(\bar{u}_{w}\right)\sum_{h\in\mathbb{I}^{u}_{w}}\left|e_{k,u}\right|, \end{aligned} \tag{3.93}$$

$$\left|e_{k+1,w}\right| \le \alpha_{w}\left(\left|e_{k,w}\right|\right) + \phi_{w}\left(\max_{\tau}\left|\upsilon(\tau)\right|\right) + f_{w}(\bar{u}_{w})\sum_{h\in\mathbb{I}^{u}_{w}}\left|e_{k,u}\right|. \quad \square \tag{3.94}$$

Proposition 1 describes the open-loop evolution (i.e. over one timestep) of the estimation error of each observer in the hierarchy. Sufficient conditions for the stability of the hierarchical observer designed according to equations (3.58) - (3.60) are provided in *Theorem 1* and *Theorem 2*.

Theorem 1: If *Assumptions 1-5* are satisfied, and there exist positive scalars ψ_i and ρ_i where $0 < \psi_i < \rho_i$ and positive constants $\delta_i > 0$ such that the following holds,

a) for the top-level observer, $|e_{0,p}| \le \rho_p$, and

$$\begin{aligned} \psi_p - Q_p\left(|\rho_p|\right) - \phi_p\left(\max_\tau |\upsilon_p(\tau)|\right) - \zeta_p\left(\max_\tau |d_p(\tau)|\right) \\ - \mathcal{K}_p \sum_{l \in \mathbb{I}_p^l} |\rho_l| \ge \delta_p, \end{aligned} \tag{3.95}$$

b) for each intermediate-level observer, $|e_{0,n,m}| \le \rho_{n,m}$, and

$$\begin{aligned} \psi_{n,m} - Q_{n,m}\left(|\rho_{n,m}|\right) - \phi_{n,m}\left(\max_\tau |\upsilon_{n,m}(\tau)|\right) - \zeta_{n,m}\left(\max_\tau |d_{n,m}(\tau)|\right) \\ - \mathcal{K}_{n,m} \sum_{l \in \mathbb{I}_{n,m}^l} |\rho_l| - f_{n,m}(\bar{u}_{n,m}) \sum_{h \in \mathbb{I}_{n,m}^u} |\rho_u| \ge \delta_{n,m}, \end{aligned} \tag{3.96}$$

c) and for each lowest-level observer, $|e_{0,w}| \le \rho_w$, and

$$\psi_w - Q_w\left(|\rho_w|\right) - \phi_w\left(\max_\tau |\upsilon_w(\tau)|\right) - f_w(\bar{u}_w) \sum_{h \in \mathbb{I}_w^u} |\rho_u| \ge \delta_w, \tag{3.97}$$

where $Q_i\left(|\rho_i|\right)$ is a class K function satisfying $Q_i\left(|e_i|\right) \ge \alpha_i\left(|e_i|\right)$, then the estimation error, $|e_i| = |\hat{x}_i - x_i|$, of each observer in the hierarchy is a decreasing sequence and uniformly ultimately bounded for $\psi_i \le |e_i| \le \rho_i$.

Proof

Convergence of the top-level observer is proved as follows. If there exist positive scalars ψ_p and ρ_p satisfying inequality (3.95), then for $\psi_p \le |e_p| \le \rho_p$, the following holds

$$|e_p| - Q_p\left(|e_p|\right) - \phi_p\left(\max_\tau |\upsilon_p(\tau)|\right) - \zeta_p\left(\max_\tau |d_p(\tau)|\right) - \mathcal{K}_p \sum_{l \in \mathbb{I}_p^l} |e_l| \ge \delta_p. \tag{3.98}$$

By comparing inequality (3.98) to (3.77) and taking into account that $Q_p\left(\left|e_p\right|\right) \geq \alpha_p\left(\left|e_p\right|\right)$ for $\left|e_p\right| \leq \rho_p$, it can be deduced that

$$\left|e_{k+1,p}\right| \leq \left|e_{k,p}\right| - \delta_p. \tag{3.99}$$

Therefore, for $t_0 \leq t_q \leq t_k$, if $\left|e_p\right| \geq \psi_p$, then $\left|e_p\right|$ can be described by the following decreasing sequence,

$$\left|e_{q,p}\right| \leq \left|e_{0,p}\right| - q\delta_p. \tag{3.100}$$

When $\left|e_p\right| < \psi_p$ is reached (i.e. $\psi_p \leq \left|e_p\right| \leq \rho_p$ is not satisfied anymore), it can be deduced that $\left|e_p\right|$ is upper bounded by $\left|e_p\right| \leq \rho_p^{\min}$ (i.e. $\lim_{k\to\infty} \sup \left|e_{k,p}\right| \leq \rho_p^{\min}$), where $\rho_p^{\min} := \max\left\{\left|e_{k+\tau_p^s,p}\right| : \left|e_{k,p}\right| \leq \psi_p\right\}$.

□

Convergence of each intermediate-level observer is proved as follows. If there exist positive scalars $\psi_{n,m}$ and $\rho_{n,m}$ satisfying inequality (3.96), then for $\psi_{n,m} \leq \left|e_{n,m}\right| \leq \rho_{n,m}$, the following holds

$$\begin{aligned} &\left|e_{n,m}\right| - Q_{n,m}\left(\left|e_{n,m}\right|\right) - \phi_{n,m}\left(\max_{\tau}\left|\upsilon_{n,m}(\tau)\right|\right) - \zeta_{n,m}\left(\max_{\tau}\left|d_{n,m}(\tau)\right|\right) \\ &-\mathcal{K}_{n,m} \sum_{l\in\mathbb{I}_{n,m}^{l}} \left|e_l\right| - f_{n,m}(\bar{u}_{n,m}) \sum_{h\in\mathbb{I}_{n,m}^{u}} \left|e_u\right| \geq \delta_{n,m}. \end{aligned} \tag{3.101}$$

By comparing inequality (3.101) to (3.78) and taking into account that $Q_{n,m}\left(\left|e_{n,m}\right|\right) \geq \alpha_{n,m}\left(\left|e_{n,m}\right|\right)$ for $\left|e_{n,m}\right| \leq \rho_{n,m}$, it can be deduced that

$$\left|e_{k+1,n,m}\right| \leq \left|e_{k,n,m}\right| - \delta_{n,m}. \tag{3.102}$$

Therefore, for $t_0 \leq t_q \leq t_k$, if $\left|e_{n,m}\right| \geq \psi_{n,m}$, then $\left|e_{n,m}\right|$ can be described by the following decreasing sequence,

$$\left|e_{q,n,m}\right| \le \left|e_{0,n,m}\right| - q\delta_{n,m}. \tag{3.103}$$

When $\left|e_{n,m}\right| < \psi_{n,m}$ is reached (i.e. $\psi_{n,m} \le \left|e_{n,m}\right| \le \rho_{n,m}$ is not satisfied anymore), it can be deduced that $\left|e_{n,m}\right|$ is upper bounded by $\left|e_{n,m}\right| \le \rho_{n,m}^{\min}$ (i.e. $\limsup_{k\to\infty} \left|e_{k,n,m}\right| \le \rho_{n,m}^{\min}$), where

$$\rho_{n,m}^{\min} := \max\left\{\left|e_{k+\tau_{n,m}^{s},n,m}\right| : \left|e_{k,n,m}\right| \le \psi_{n,m}\right\}. \qquad \square$$

Finally, convergence of each lowest-level observer is proved as follows. If there exist positive scalars ψ_w and ρ_w satisfying inequality (3.97), then for $\psi_w \le |e_w| \le \rho_w$, the following holds

$$|e_w| - Q_w\left(|e_w|\right) - \phi_w\left(\max_{\tau} |\upsilon_w(\tau)|\right) - f_w(\bar{u}_w) \sum_{h\in\mathbb{I}_w^u} |e_u| \ge \delta_w, \tag{3.104}$$

By comparing inequality (3.104) to (3.79) and taking into account that $Q_w\left(|e_w|\right) \ge \alpha_w\left(|e_w|\right)$ for $|e_w| \le \rho_w$, it can be deduced that

$$\left|e_{k+1,w}\right| \le \left|e_{k,w}\right| - \delta_w. \tag{3.105}$$

Therefore, for $t_0 \le t_q \le t_k$, if $|e_w| \ge \psi_w$, then $|e_w|$ can be described by the following decreasing sequence,

$$\left|e_{q,w}\right| \le \left|e_{0,w}\right| - q\delta_w. \tag{3.106}$$

When $|e_w| < \psi_w$ is reached (i.e. $\psi_w \le |e_w| \le \rho_w$ is not satisfied anymore), it can be deduced that $|e_w|$ is upper bounded by $\left|e_w\right| \le \rho_w^{\min}$ (i.e. $\limsup_{k\to\infty} \left|e_{k,w}\right| \le \rho_w^{\min}$), where

$$\rho_w^{\min} := \max\left\{\left|e_{k+\tau_w^{s},w}\right| : \left|e_{k,w}\right| \le \psi_w\right\}. \qquad \square$$

The convergence of the hierarchical observer is presented in *Theorem 2.*

Theorem 2: The ultimate boundedness of each observer in the hierarchy implies that the state estimation error of the hierarchical observer is ultimately bounded.

Proof:

The total estimation error of the hierarchical observer e_k^{total} is upper bounded as follows.

$$\lim_{k\to\infty} \sup \left| e_k^{total} \right| \leq \sum_{i=1}^{N_{total}} \rho_i^{\min}, \tag{3.107}$$

where N_{total} is the total number of observers in the hierarchy and $\rho_i^{\min}$ associated with observer i is defined as $\rho_i^{\min} := \max \left\{ \left| e_{k+\tau_i^s,i} \right| : \left| e_{k,i} \right| \leq \psi_i \right\}$. □.

Theorem 1 characterizes the effects of the initial estimation error, the magnitude of sensor noise, the model order reduction error, and the estimation accuracy of upper and lower level observers on the estimation accuracy of each observer in the hierarchy. In particular, equations (3.95) - (3.97) are achieved if the initial estimation error, the upper bound on the sensor noise, and the upper bound on the model order reduction error are sufficiently small, and the estimation accuracy of upper and lower observers is sufficiently high. *Theorem 1* provides insights on the choice of the various parameters that affect the convergence and stability of the hierarchical observer and thus can be a very useful tool during its design process.

Note: The upper bounds in *Proposition 1* (i.e. equations (3.77)-(3.79)) are derived in a conservative way. For example, this can be seen in the terms representing the effect of the estimation accuracy of upper-level and lower-level observers on the stability and convergence of each observer i in the hierarchy. For instance, in the proof of *Proposition 1*, the term $\left| (y_{k,p} - H_p \hat{x}_{k,p}^l) \right|$ in equation (3.81) is upper bounded by $\sum_{l \in \mathbb{I}_p^l} \left| e_{k,l} \right|$ (i.e. the sum of the norm of the estimation error of every lower-level observer with which the top level observer communicates). This conservatism can be relaxed by just considering the estimation error of the local state estimates used as pseudo-measurements by the top-level observer. However, the case study presented in section 3.6 demonstrates that, in practice, the derived error bounds of the proposed hierarchical obsever are not too conservative.

3.6 Case Study

3.6.1 Example 1

In this example, a 2-level hierarchical observer is designed for the 2-state system shown in Figure 3.2. At the lowest level of the hierarchy, each state is considered as a subsystem and is estimated by a Kalman filter. At the top level of the hierarchy, the 2 states are aggregated into a single super-state (Figure 3.3) that is estimated by a third Kalman filter. The super-capacitance of the super-state is equal to the sum of the capacitances of the 2 states. The estimate of the super-state is passed to each lowest-level observer to account for the coupling information needed. The profiles of the control inputs u_i along the green edges are shown in Figure 3.4. $T_{s1} = 20$, $T_{s2} = 40$, $c_{p,i} = 3500$, and $B = 2916$. The capacitances of the vertices are $C_1 = 350$, $C_2 = 300$, and $\overline{C^u} = 650$. By applying conservation of energy on each vertex, the dynamics of T_{h1} (i.e. the first subsystem at the lowest level of the hierarchy) are given by

$$C_1 \dot{T}_{h1} = u_1 c_p T_{s,1} + B(T_{h2} - T_{h1}) - u_1 c_p T_{h1}, \tag{3.108}$$

the dynamics of the T_{h2} (i.e. the second subsystem at the lowest level of the hierarchy) are given by

$$C_2 \dot{T}_{h2} = u_2 c_p T_{s,2} - B(T_{h2} - T_{h1}) - u_2 c_p T_{h2}, \tag{3.109}$$

and the dynamics of the super-state T_h^u at the top level of the hierarchy are given by

$$\overline{C_h^u} \dot{T}_h^u = u_1 c_p T_{s,1} + u_2 c_p T_{s,2} - u_1 c_p T_h^u - u_2 c_p T_h^u. \tag{3.110}$$

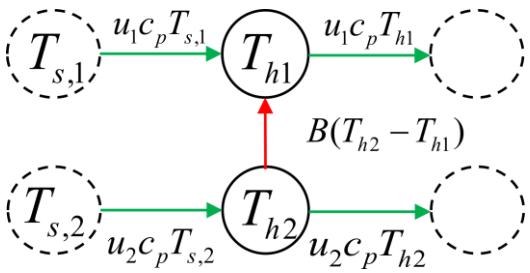

Figure 3.2 Graph-based model of a 2-state system.

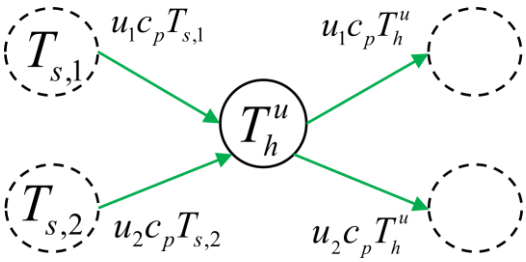

Figure 3.3 Graph-based model of the super-state obtained by aggregating the 2-state system.

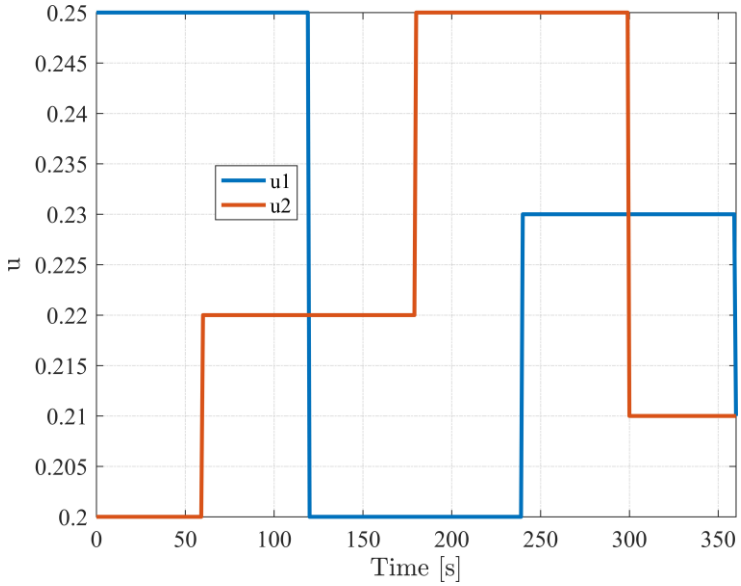

Figure 3.4 Control inputs of the 2-state system.

Figure 3.5 shows the discretized dynamics of the 2 subsystems at the lowest level and the super-state at top level of the hierarchy. This figure shows that the super-state is roughly an average of the 2 states.

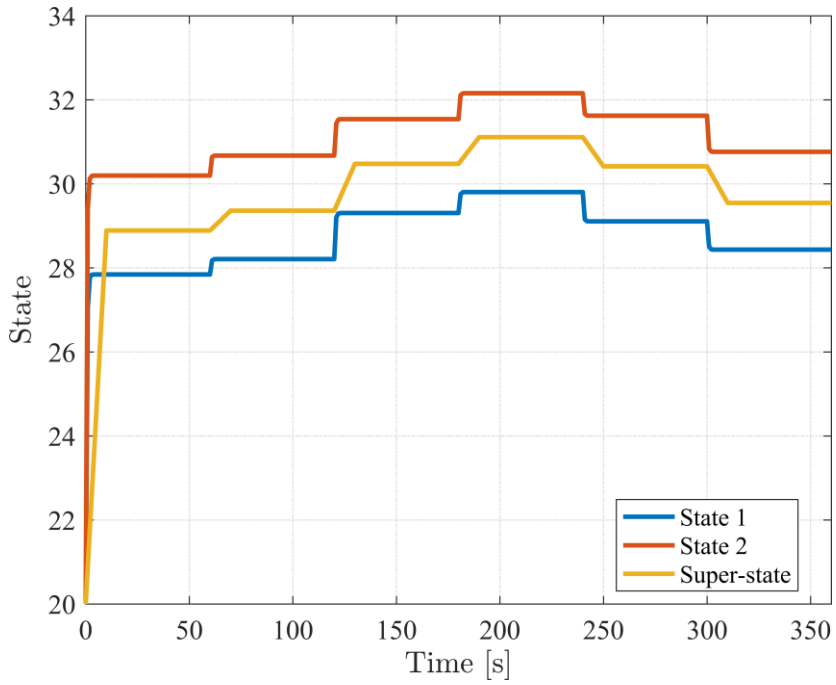

Figure 3.5 Dynamics of the 2 states versus the super-state.

The Kalman filter of each state at the lowest level of the hierarchy receives noisy measurements of its own state disturbed by additive white noise and the coupling information needed from the top-level observer. Specifically, in equation (3.108), T_{h2} is an unmeasured coupling state with respect to T_{h1}. Similarly, in equation (3.109), T_{h1} is an unmeasured coupling state with respect to T_{h2}. To account for this unmeasured coupling information, each observer at the lowest level of the hierarchy receives an estimate of the super-state T_h^u from the top-level observer. At the lowest level of the hierarchy, each observer updates every 1s and the top-level observer updates every 10s. The performance of each observer at the lowest level of the hierarchy is presented in Figure 3.6. Figure 3.7 shows the performance of the top-level Kalman filter. These results show that the hierarchical observer converged using coupling information passed down in the hierarchy.

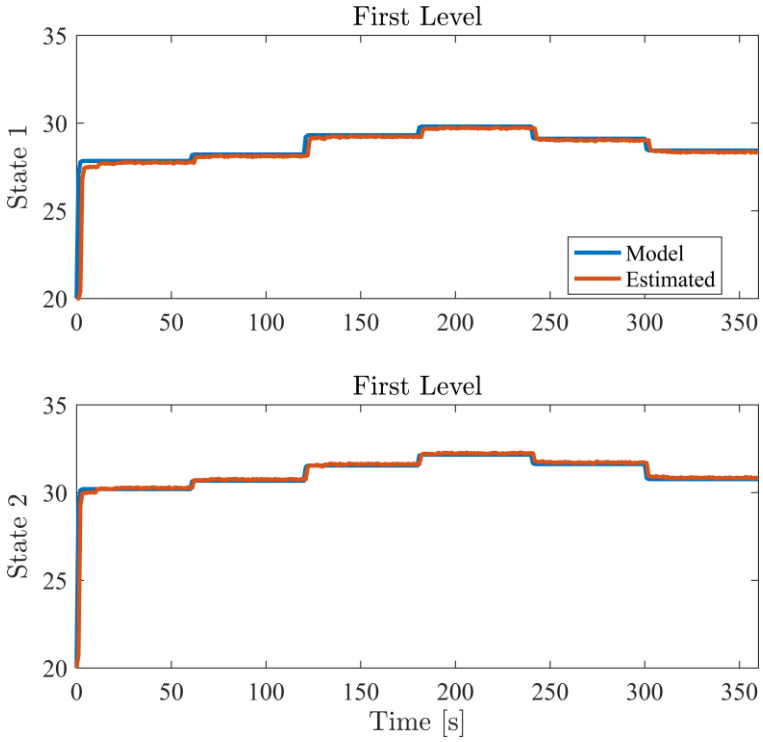

Figure 3.6 Estimated versus actual values of the two subsystems at the lowest level of the hierarchy.

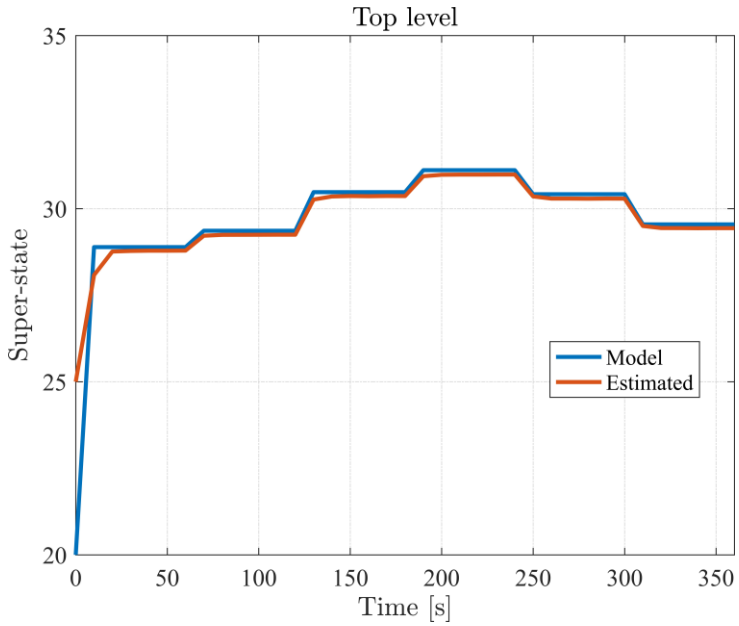

Figure 3.7 Estimated versus actual values of the super-state at the top level of the hierarchy.

3.6.2 Example 2

The goal of this case study is to derive the error bounds of an example hierarchical observer designed to estimate the dynamic thermal behavior of a simple fluid-based thermal management system (FTMS). A schematic of the FTMS is presented in Figure 3.8. The system is composed of 2 fluid loops (i.e. FL1 and FL2) connected through a pump and a valve. Each fluid loop consists of a fluid reservoir, a pump, a cold plate heat exchanger, and several fluid-to-fluid heat exchangers. Heat enters to the system through the walls of the cold plate heat exchangers and gets transferred to the 4 heat sinks referred to in Figure 3.8 through the fluid driven by the pumps.

Experimentally validated thermal graph-based models for these components can be found in [40]. Figure 3.9 shows a thermal graph-based model for the entire system (i.e. FL1 and FL2). The model consists of 21 states representing the temperature of the fluids, the cold plate walls, and the heat exchanger walls. In addition, the model includes 4 external sink vertices that capture the interactions of the system with the external environment.

A hierarchy of two levels is then obtained as shown in Figure 3.10. The top-level model is a reduced-order graph-based model that consists of 11 states that capture the thermal dynamics of the entire system. This model is designed by applying the aggregation-based model order reduction technique presented in section 2.4. The lowest-level models are designed by decomposing the full-order graph-based model of the entire system into two subsystems, each representing one fluid loop. This is achieved by cutting the edge connecting the temperature of the secondary sides of heat exchangers 1 and 5 in Figure 3.9. Consequently, in Figure 3.10, the vertex representing the temperature of the secondary side of heat exchanger 5 is modeled as a coupling vertex in the graph-based model of fluid loop 1 (i.e. FL1). Similarly, the vertex representing the temperature of the secondary side of heat exchanger 1 is modeled as a coupling vertex to the graph-based model of fluid loop 2 (i.e. FL2).

As demonstrated in section 3.2.1, thermal power flows of a FTMS satisfy equation (3.2). Therefore, the thermal dynamics of the hierarchical model shown in Figure 3.10 can be represented by a linear time varying system. The dynamic thermal behavior of the system is then estimated by a two-level hierarchical observer comprised of two local Kalman filters at the lowest level and a global Kalman filter at the top level of the hierarchy. The observer

architecture is shown in Figure 3.11. O_i refers to the observer of subsystem i (e.g. O_{FL1} refers to the observer of fluid loop FL1). At the lowest level, the observers update every $1\,s$ and the top-level observer updates every $10\,s$.

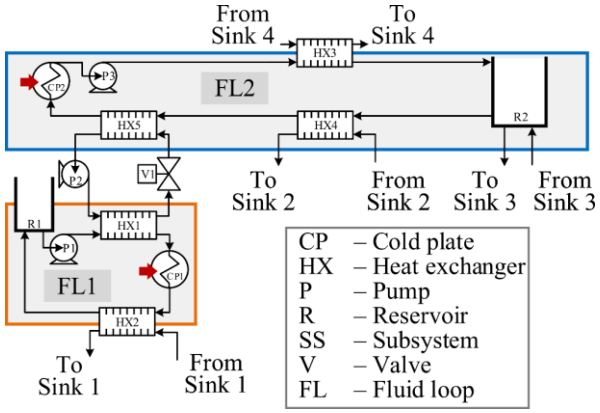

Figure 3.8 Schematic of an example fluid-based thermal management system (FTMS).

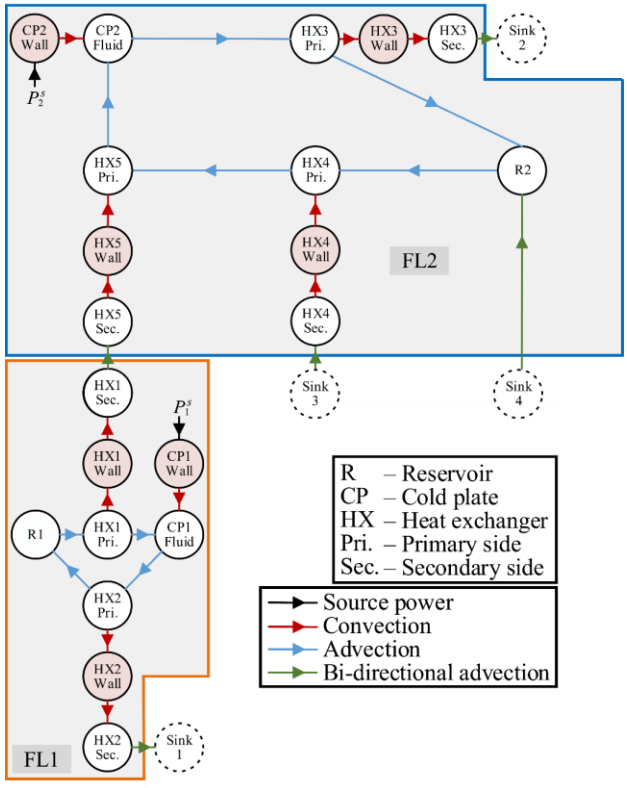

Figure 3.9 Thermal graph-based model of the FTMS in Figure 3.8.

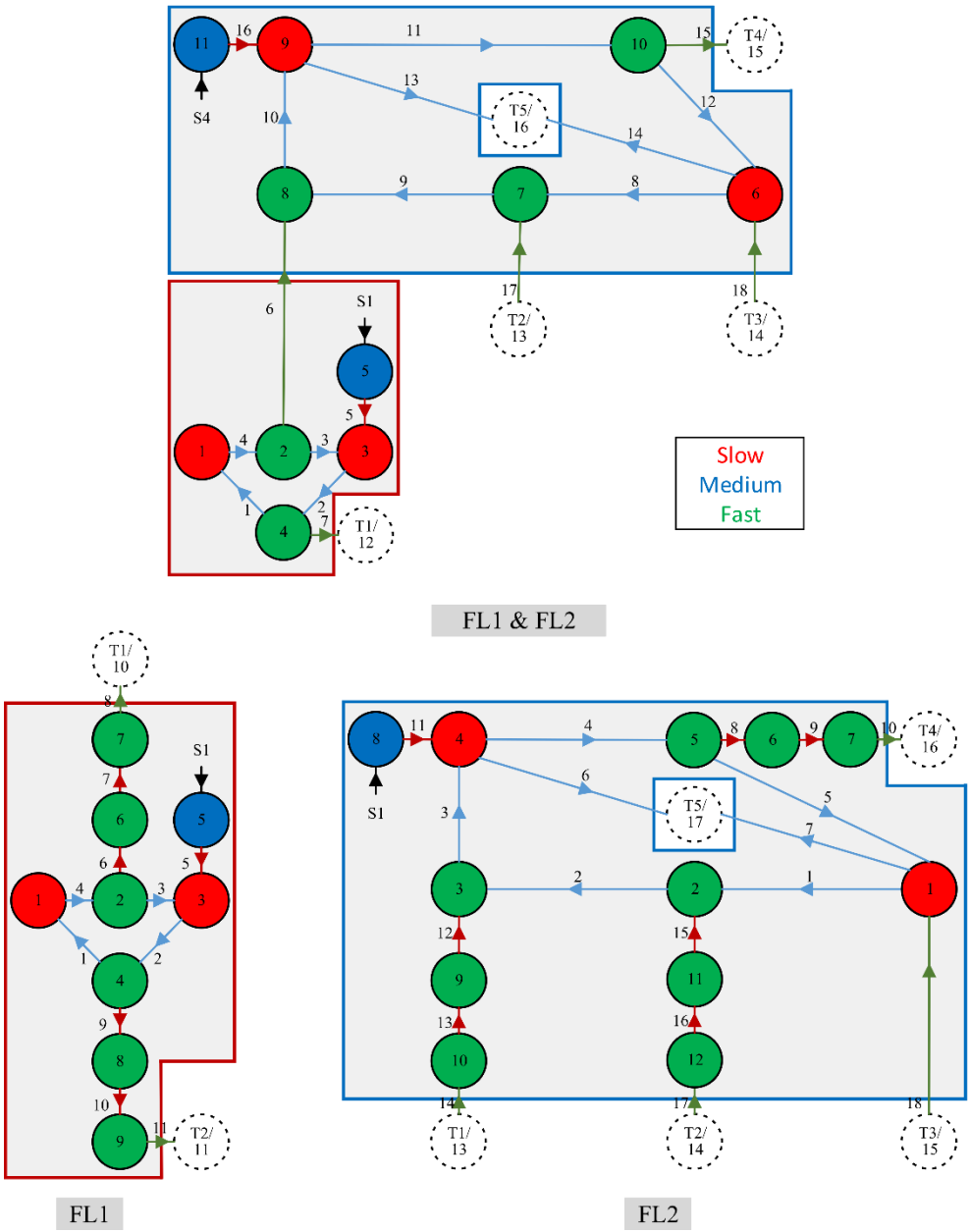

Figure 3.10 A two-level hierarchical model of the system shown in Figure 3.8.

The 2-norm of the estimation error of each observer in the hierarchy is shown in Figure 3.12. The bounds on the estimation errors are calculated according to equations (3.77) and (3.79) using the following parameters. $\max_{\tau}\left|\upsilon_p(\tau)\right| = \max_{\tau}\left|\upsilon_{w,FL1}(\tau)\right| = \max_{\tau}\left|\upsilon_{w,FL2}(\tau)\right| = 0.75^{\circ}C$, $\max_{\tau}\left|d_p(\tau)\right| = 1.5^{\circ}C$, $\mathcal{K}_p = 2.14$, $f_{w,FL1}(\bar{u}_{w,FL1}) = 0.586$, and $f_{w,FL2}(\bar{u}_{w,FL2}) = 0.576$. Figure 3.12 shows that, at all levels of the hierarchy, the estimation errors stay within the calculated set of bounds.

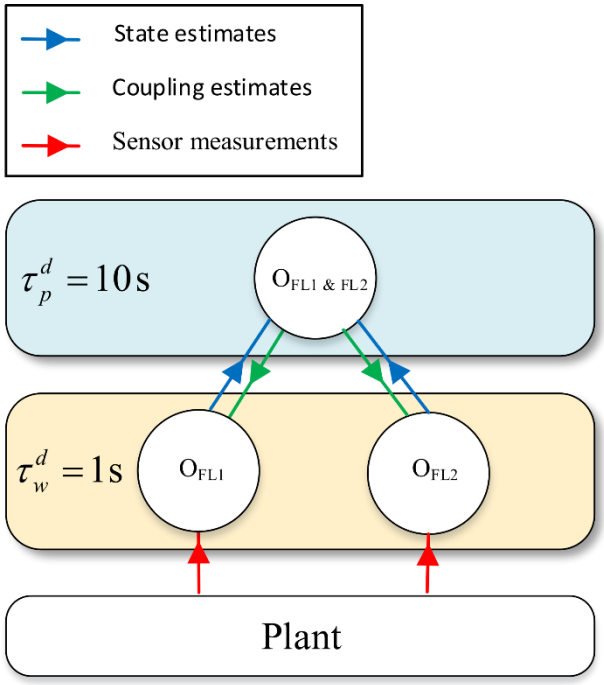

Figure 3.11 A two-level hierarchical observer.

3.7 Conclusion

This chapter presented a multilevel hierarchical estimation algorithm with a novel coordination framework that directly accounts for coupling between subsystems. The proposed algorithm creates a tradeoff between centralized and decentralized estimation. Section 3.2 presented the formulation of a centralized observer used as a benchmark for the proposed hierarchical estimation framework. The architecture of the proposed hierarchical observer was presented in section 3.3. The advantages of the proposed framework compared to conventional

and current practices were presented in section 3.4. Section 3.5 presented the formulation, stability analysis and sufficient conditions for the convergence of the proposed hierarchical observer. Finally, Section 3.6 presented two case studies that investigated the stability properties of a two-level hierarchical observer. Experimental validation of the proposed hierarchical estimation approach will be provided in Chapter 4. Furthermore, the performance of the hierarchical observer will be compared to conventional centralized and decentralized observers in terms of accuracy and computational complexity.

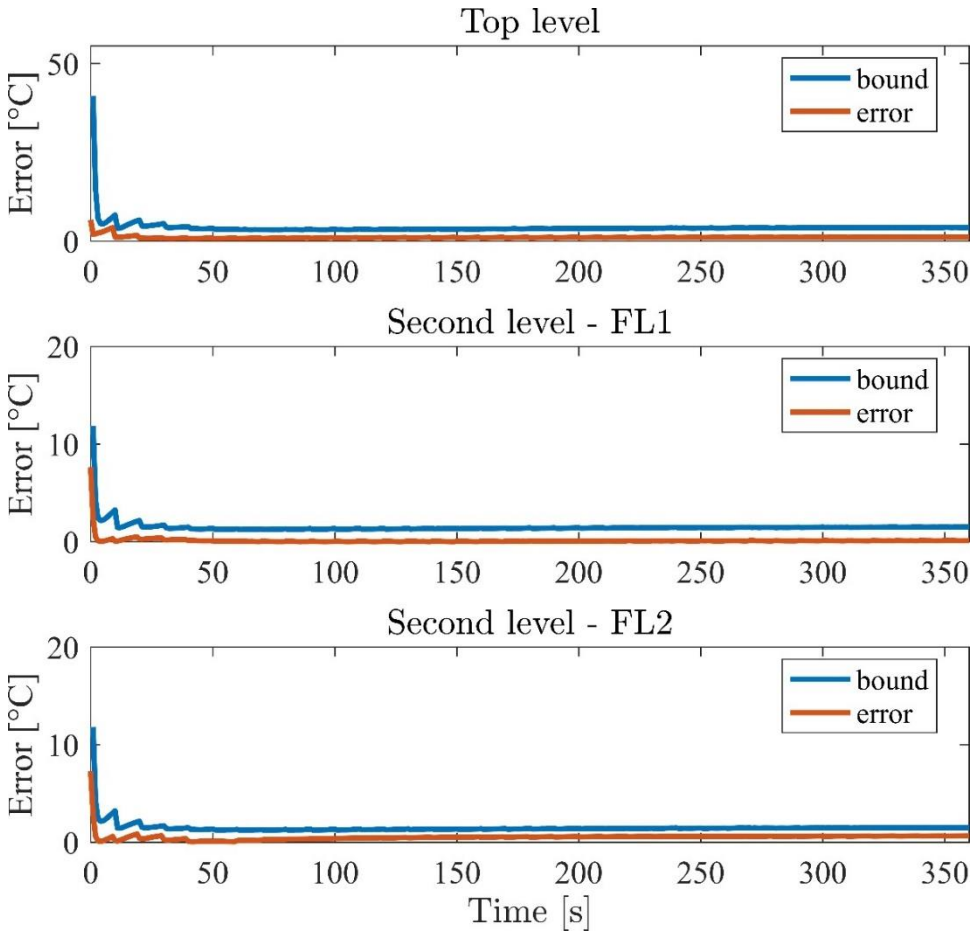

Figure 3.12 Convergence of the hierarchical observer.

Chapter 4
Experimental Validation of a Hierarchical Observer for a Fluid-based Thermal Management System

4.1 Introduction

This chapter experimentally validates the hierarchical estimation framework presented in Chapter 3. For this purpose, a modular and scalable fluid thermal management system testbed has been developed. The testbed can be easily reconfigured to represent various system architectures with different sets of components. Several architectures designed using this testbed are presented in [23], [48], [62]. A comparison between the proposed hierarchical estimation framework, a decentralized observer, and a benchmark centralized observer is also presented in this chapter. It is found that the proposed hierarchical estimation approach provides a beneficial tradeoff between accuracy and computational complexity. Specifically, compared to a conventional centralized framework, the proposed estimation approach significantly reduces the computational complexity required to run the observer at the expense of a mild reduction in estimation accuracy. Compared to a decentralized observer, the proposed estimation framework offers an increase in the estimation accuracy at the expense of some increase in the computational complexity.

The remainder of this chapter is organized as follows. The testbed used for experimental validation is presented in section 4.2. A hierarchical graph-based model of the system is presented in section 4.3. A multi-level hierarchical observer is presented in section 4.4. Closed-loop simulation results of the hierarchical observer coupled to a hierarchical controller are presented in section 4.5. Experimental closed-loop performance is demonstrated in section 4.6.

Section 4.7 provides a comparison between the hierarchical observer and a conventional centralized observer. Section 4.8 provides a comparison between the hierarchical observer and a decentralized observer. A conclusion for this chapter is presented in section 4.9.

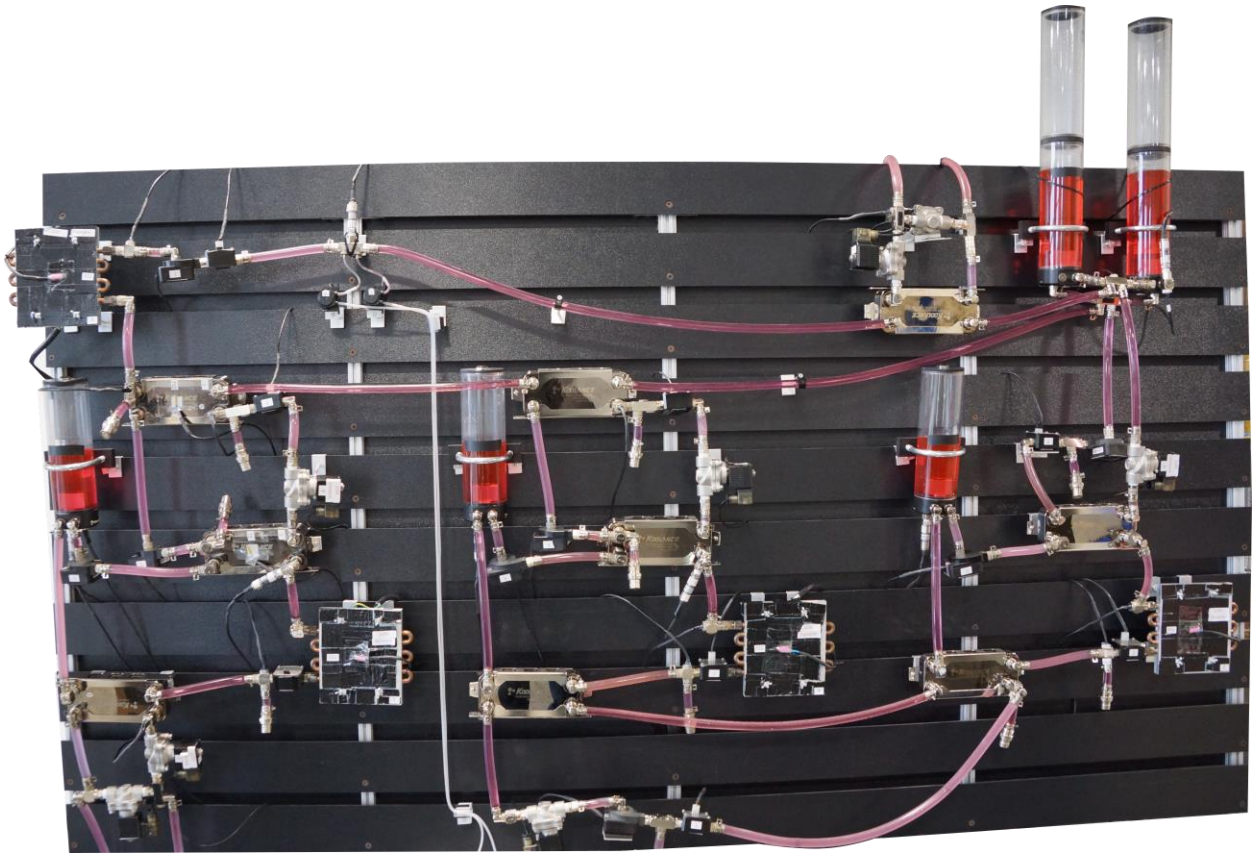

Figure 4.1 A fluid-based thermal management system testbed using to experimentally validate the proposed hierarchical estimation approach.

4.2 System Description

The fluid-based thermal management system testbed used to experimentally validate the proposed hierarchical estimation approach is shown in Figure 4.1. A schematic of the testbed is presented in Figure 4.2. The current configuration is intended to replicate the power flows that occur in a fuel thermal management system of an electrified aircraft without representing any specific platform. The testbed consists of 4 main fluid loops. Each loop contains a fluid reservoir, a pump, a cold plate heat exchanger, and fluid-to-fluid heat exchangers. Additional pumps and valves are used throughout the system to control the flow of the fluid between the loops. In this

configuration, valves can only be open or closed. In addition, the testbed includes temperature sensors, pressure sensors, mass flow rate sensors, and two chillers (i.e. heat sinks). Chiller 1 is connected to fluid loop 1 and chiller 2 is connected to fluid loop 4 as shown in Figure 4.2. Detailed descriptions of these components can be found in [40].

Thermal energy dissipated by the associated electrical components (i.e. battery, power electronics, electric machine, etc.) is represented by heat loads applied to the walls of the 4 cold plate heat exchangers. The main goal is to absorb that heat and transfer it through the fluid to the two heat sinks to keep the temperature of the electrical components within specific limits. The heat sinks can represent the ambient environment or a vapor compression system (VCS), for example. Throughout the remaining sections of this chapter, cold plate heat exchangers are referred to as cold plates and fluid-to-fluid heat exchangers are referred to as heat exchangers.

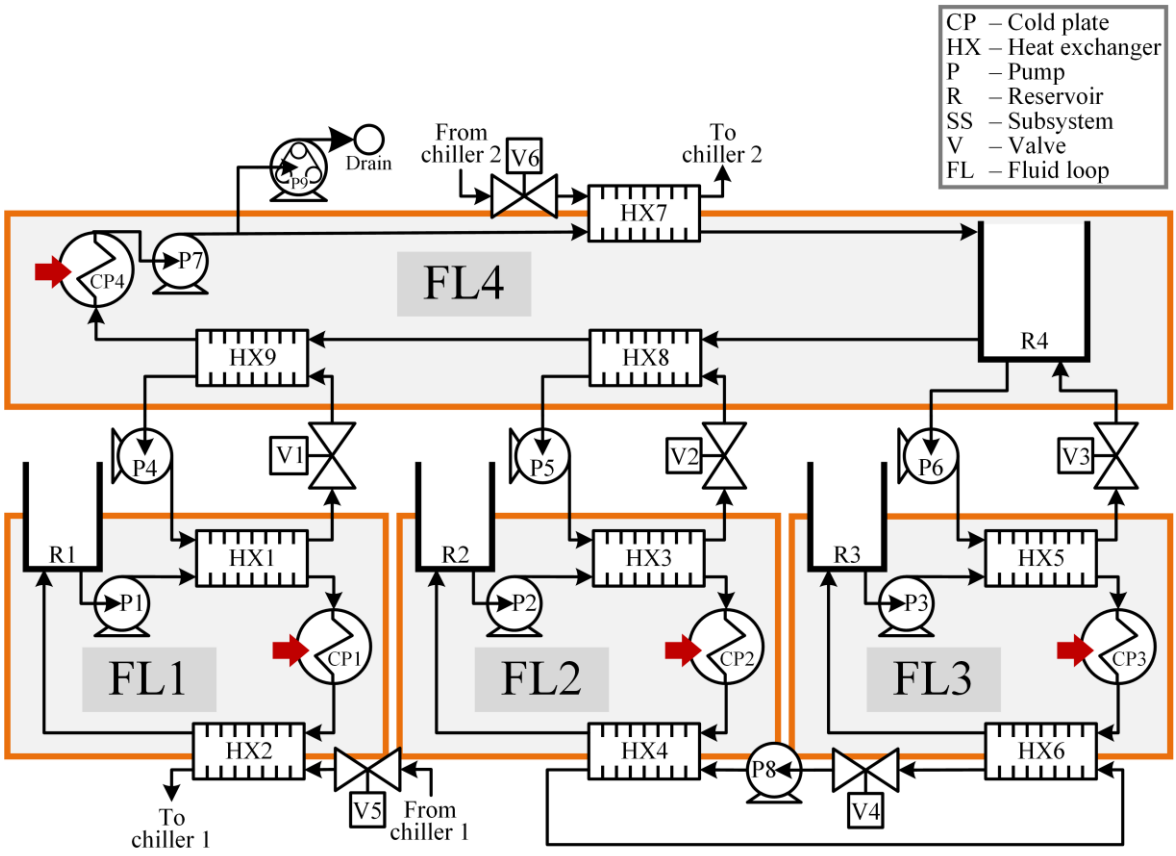

Figure 4.2 Schematic of the fluid-based thermal management system testbed.

4.3 Hierarchical Graph-based Model

Figure 4.3 shows the full-order thermal graph-based model of the entire testbed shown in Figure 4.1. The model consists of 39 states (i.e. vertices) representing the temperature of the fluids, the cold plate walls, and the heat exchanger walls. Heat enters the system through the source power flows applied to the cold plate walls (blue edges in Figure 4.3) and gets transferred to the thermal sinks through advection (i.e. green arrows) and convection (i.e. red arrows). The temperatures of the two heat sinks are modeled as known bounded exogeneous disturbances to the system.

A hierarchy of 3 levels is then obtained by spatially decomposing the full-order graph-based model into a set of interconnected subgraphs as done in [62]. The hierarchical graph-based model is shown in Figure 4.4. At the lowest level of the hierarchy, 4 subgraphs (SS1, SS2, SS3, and SS4), each representing one of the 4 fluid loops, are obtained by cutting 4 edges in the full-order graph-based model presented in Figure 4.3. Coupling vertices are represented as sink vertices in the resulting subgraphs. For example, subgraph 1 is obtained by cutting the advection edge connecting the temperatures of the secondary sides of heat exchangers 1 and 9. The vertex corresponding to the temperature of the secondary side of heat exchanger 9 is modeled as a sink vertex (i.e. disturbance) to subgraph 1. Similarly, the vertex corresponding to the temperature of the secondary side of heat exchanger 1 is modeled as a sink vertex to subgraph 4. At the second level of the hierarchy, two subgraphs (SS5 and SS6) are derived. The first subgraph (i.e. SS5) is a reduced-order graph-based model that captures the dynamics of SS1 and SS4. The second subgraph (i.e. SS6) is a reduced-order graph-based model that captures the dynamics of SS2 and SS3. At the highest level of the hierarchy, a reduced-order graph-based model of 17 states that capture the dynamics of SS5 and SS6 is derived. The top-level model is a low-resolution representation of the full-order model presented in Figure 4.3. Model order reduction is achieved by applying the aggregation-based approach presented in section 2.4.

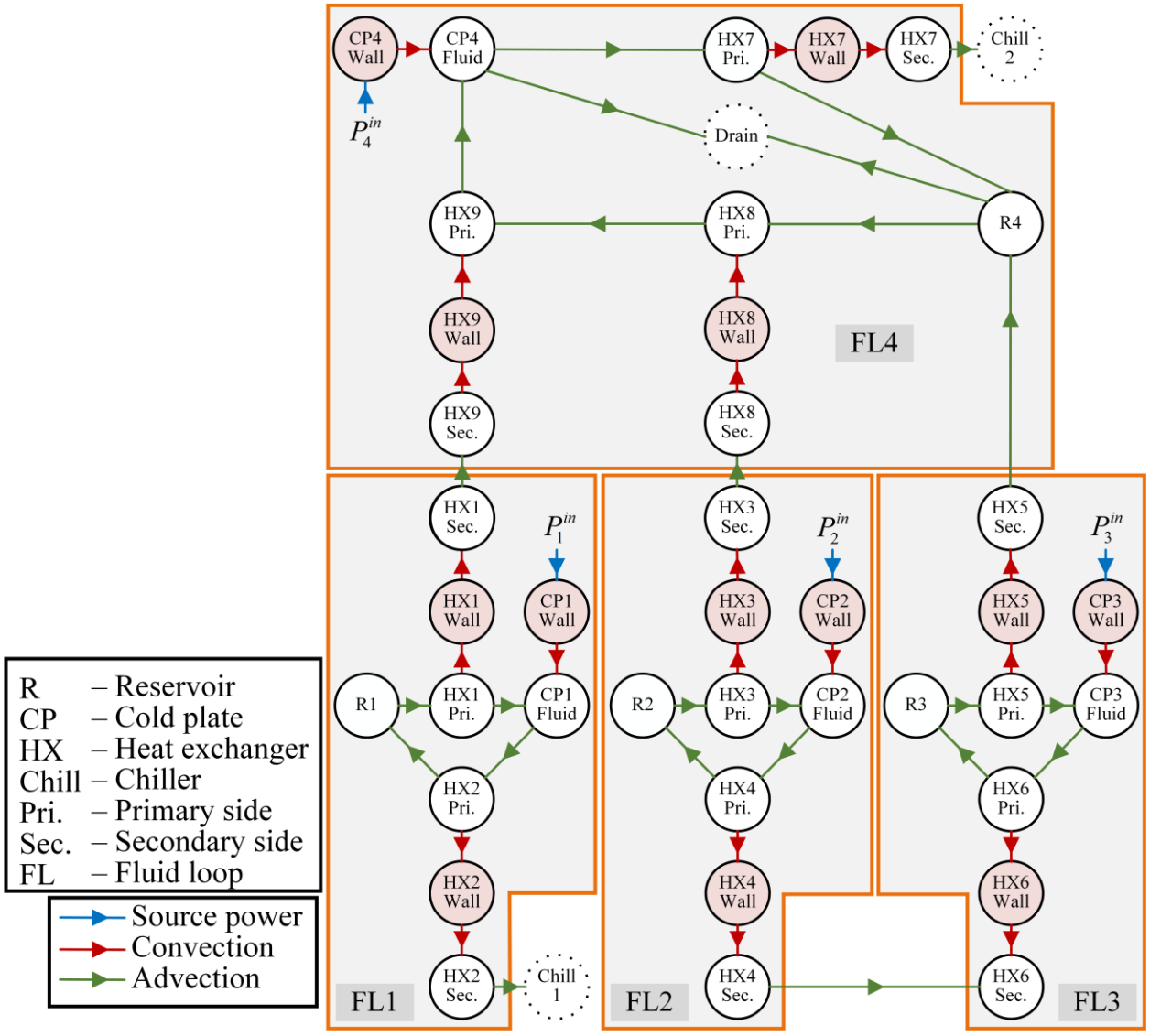

Figure 4.3 Full-order thermal graph-based model of the entire system shown in Figure 4.1.

4.4 A Multi-level Hierarchical Observer

The thermal dynamics of the fluid-based thermal management system are estimated by a 3-level hierarchical observer. To test the closed loop performance, the observer is connected to a previously developed hierarchical controller. The architecture of the hierarchical observer-controller is shown in Figure 4.5. Each controller of the hierarchical controller communicates with an observer of the hierarchical observer operating at the same level of the hierarchy to manage the dynamics of a subsystem. To capture the switching behavior of the valves, each

observer is designed as a switching Kalman filter (see Chapter 3) and each controller is designed as a switching model predictive controller (MPC). The reader is referred to [62] for a detailed design procedure of the hierarchical controller.

The control inputs of the thermal management system are defined by the mass flow rates (i.e. edge inputs of the thermal graph) controlled by the pumps and the valves of the testbed. The goal of the hierarchical observer is to communicate accurate dynamic thermal state estimates to the hierarchical controller at each level of the hierarchy. The goal of the hierarchical controller is to achieve high capability and to ensure the safety of the thermal management system. High capability represents the ability of the controller to track a reference thermal power profile corresponding to a desired operation of the electrical system. Safety corresponds to the ability of the controller to track the desired reference thermal trajectories without violating thermal constraints. As detailed in [62], when the fluid thermal management system does not have enough cooling capacity to track the thermal reference trajectories without violating temperature constraints, the controller performs selective electrical load shedding as necessary to guarantee the safety of the system. However, the controller is required to guarantee that loads that are critical to the mission can always be applied (i.e. load shedding is not allowed for critical loads).

As shown in Figure 4.5, observers and controllers update every 2s at the lowest level of the hierarchy, every 10s at the second level, and every 60s at the highest level. 9 temperature sensors are used by lowest-level observers to measure states 1, 5, and 7 of SS1, states 1, and 5 of SS2 and SS3, and states 1, and 8 of SS4. The observer of SS5 receives 5 pseudo-measurements from the observer of SS1 and 6 pseudo-measurements from the observer of SS4. The observer of SS6 receives 5 pseudo-measurements from the observer of SS2 and 5 pseudo-measurements from the observer of SS3. The global observer receives 9 pseudo-measurements from the observer of SS5 and 8 pseudo-measurements from the observer of SS6. Throughout the hierarchy, coupling state estimates are passed down by observers at the level above and internal state estimates are passed up by observers at the level below in the hierarchy and treated as pseudo-measurements.

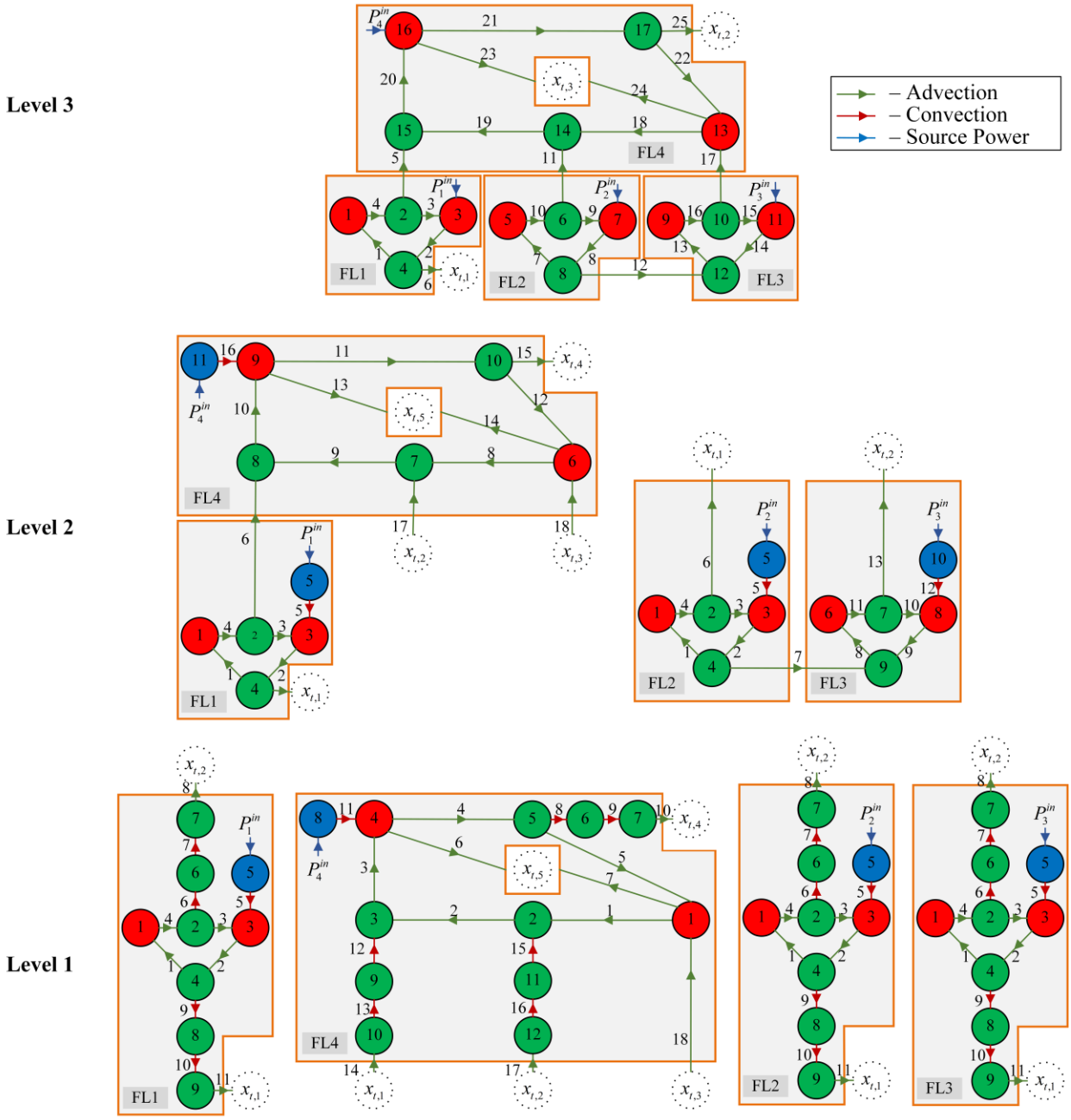

Figure 4.4 A hierarchical thermal graph-based model of the system shown in Figure 4.1.

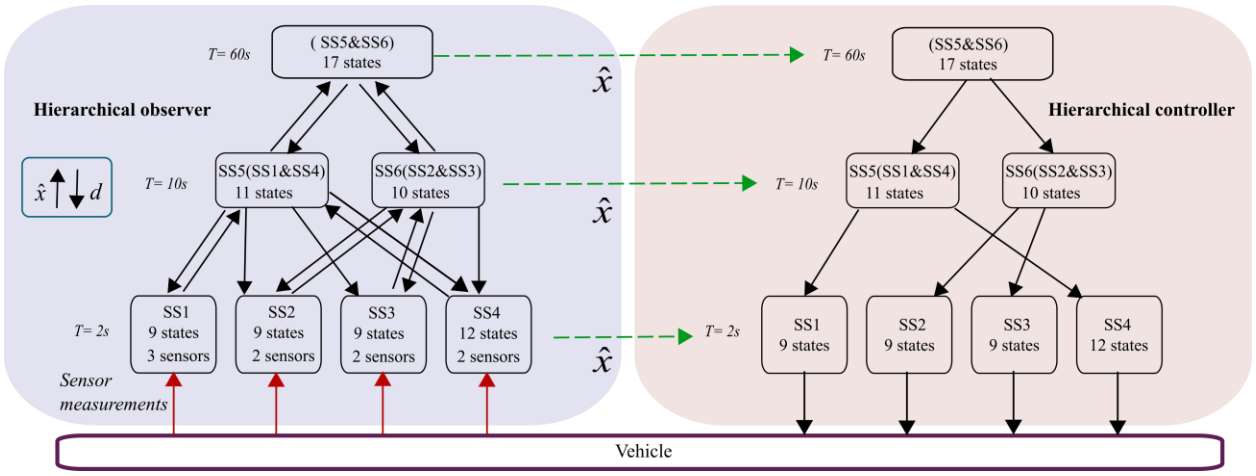

Figure 4.5 A 3-level hierarchical observer-controller designed to manage the dynamics of the system presented in Figure 4.1.

4.5 Simulation Results

Simulation results of the closed-loop performance of the hierarchical observer-controller are presented in this section. The hierarchical observer and the hierarchical controller are simulated on a desktop computer with 16 GB of RAM and 3.40 GHz Intel i7 processor. Figure 4.6 shows the performance of the hierarchical observer at all levels of the hierarchy. The simulated values of state 7 from SS2 (i.e. the state representing the temperature of the secondary side of HX3), state 2 from SS6, and state 6 from the top-level model are compared to their estimated values obtained from the hierarchical observer at the first (i.e. lowest), second, and top level of the hierarchy. Figure 4.6 demonstrates that the hierarchical observer achieves good estimation accuracy for component-level and system-level state estimation. The closed-loop performance of the hierarchical controller is presented in Figure 4.7 and Figure 4.8. The grey profiles in Figure 4.7 represent the desired reference thermal power trajectories that the hierarchical controller of the thermal management system is required to track. Light grey profiles represent sheddable loads and dark grey profiles represent critical loads that cannot be shed. As shown Figure 4.7, the applied loads (i.e. red profiles) track most of the desired profiles. The controller performed load shedding when necessary. However, all critical loads are applied throughout the mission. Figure 4.8 shows the states representing the fluid and wall temperatures of the 4 cold plates. These states correspond to the hottest states in the system as heat enters the

system through the cold plate walls. Dashed lines represent thermal constraints chosen to be 15℃ and 40℃ for the states representing fluid temperatures and 15℃ and 45℃ for the states representing wall temperatures. Figure 4.8 demonstrates that the controller maintained the safety of the system by keeping the hottest states within their constraints. By analyzing the results presented in Figure 4.7 and Figure 4.8, it can be noticed that the controller performed load shedding when the states reached their upper constraints. For example, the controller shed some of the loads applied to the wall of cold plate 1 (i.e. cold plate 1 plot in Figure 4.7) when the wall temperature of this cold plate (i.e. CP1 wall plot in Figure 4.8) reached its upper constraint. Additionally, it can be noticed that, throughout the entire mission, the temperatures are operating closer to their upper constraints which demonstrates that the controller is maximizing the system capability by pushing the system to its upper limits. This simulation case study shows that the hierarchical observer achieves good estimation accuracy that enables successful control design.

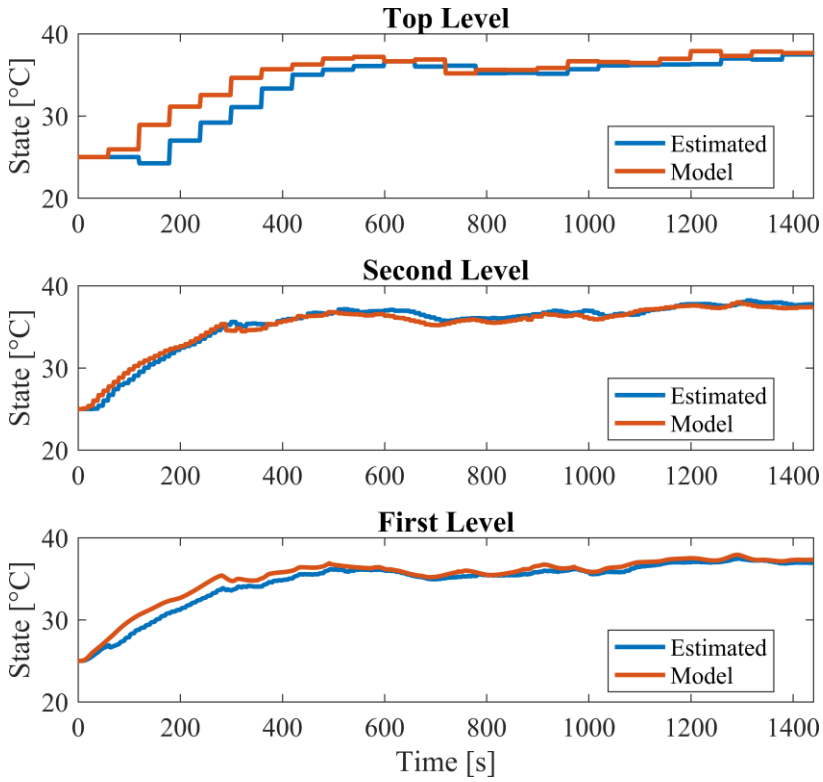

Figure 4.6 Actual vs estimated value of the state representing the temperature of the secondary side of heat exchanger 3 at all levels of the hierarchy – in simulation.

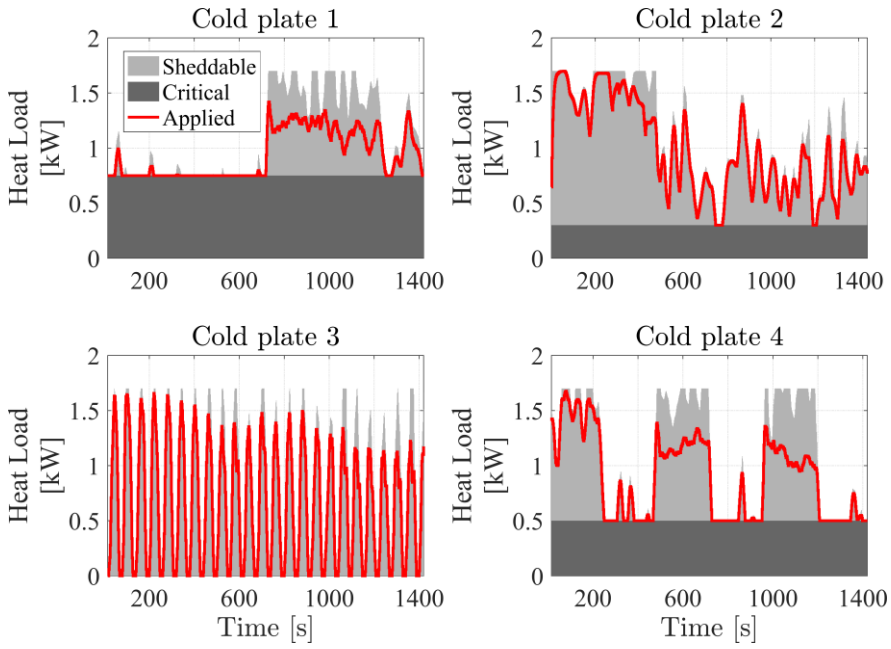

Figure 4.7 Desired versus applied loads – in simulation.

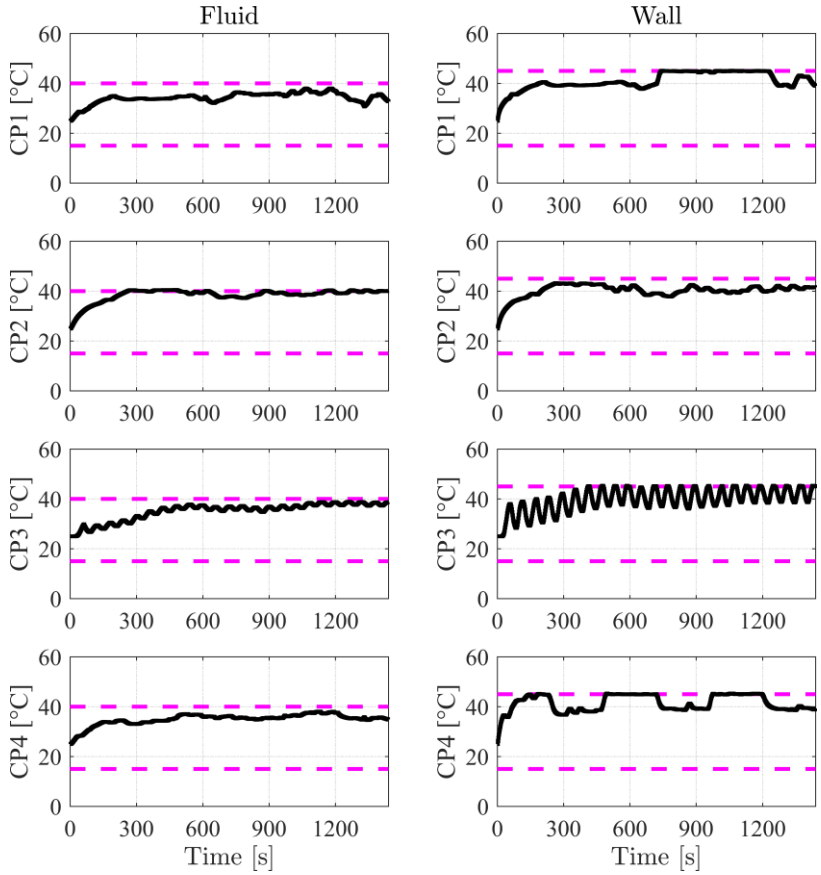

Figure 4.8 Fluid and wall temperature of the 4 cold plates – in simulation.

4.6 Experimental Results

The performance of the hierarchical observer-controller is experimentally validated on the testbed shown in Figure 4.1. The controllers are solved in parallel in this case to allow for real-time implementation. The same desktop computer used to run the simulation case study is used in the experimental validation. To experimentally validate the performance of the hierarchical observer, additional temperature sensors used as validation sensors are added to the testbed. Readings of the validation sensors are not fed to the observers at the lowest level of the hierarchy (i.e. H_w matrices from equation (3.47) are the same in the simulation and experimental case studies).

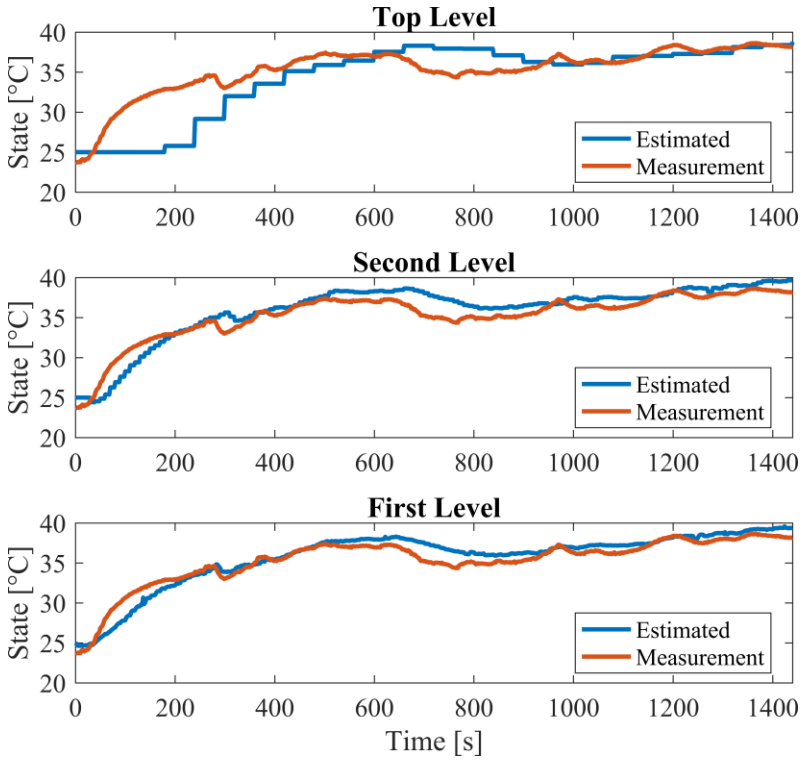

Figure 4.9 Actual vs estimated value of the state representing the temperature of the secondary side of heat exchanger 3 at all levels of the hierarchy – experimental results.

Figure 4.9 shows the experimentally estimated values of the states shown in Figure 4.6. Specifically, Figure 4.9 shows the estimated versus the actual value of the state representing the temperature of the secondary side of HX3, at all levels of the hierarchy. In this case, the

experimentally estimated values are compared to measurements obtained from a validation sensor (i.e. the same sensor reading is compared to the experimentally estimated value of the state at all levels of the hierarchy). Figure 4.9 shows that the hierarchical observer achieves good estimation accuracy when applied in real-time on an experimental system. The experimental closed-loop performance of the hierarchical controller is presented in Figure 4.10 and Figure 4.11. The experimental results and the simulation results of the controller are similar. However, constraints were slightly violated (i.e. less than 1°C) in the experiment (i.e. Figure 4.11) due to slack variables introduced in the controller, modeling errros or unknown disturbances.

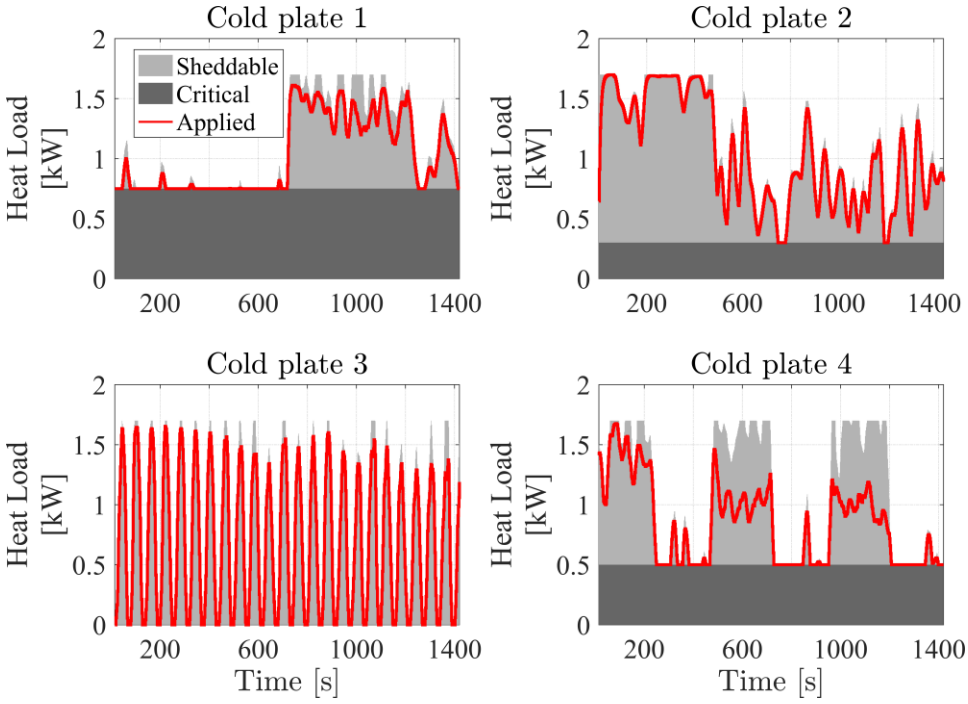

Figure 4.10 Desired versus applied loads – experimental results.

4.7 Comparison to a Centralized Observer

This section presents a comparison between the hierarchical observer and a benchmark centralized observer. In the centralized observer case, the states of the full-order thermal graph-based model of the entire testbed shown in Figure 4.1 are estimated by a single switching Kalman filter updating every 2s and receiving temperature measurements from 9 sensors. That is, the centralized observer updates at the same rate as the lowest-level observers of the hierarchical observer. Furthermore, the centralized observer uses the same number and

placement of temperature sensors used by the lowest-level observers of the hierarchical observer. The same desktop computer used to simulate the hierarchical observer is also used to simulate the centralized observer.

To compare the overall estimation accuracies of the proposed hierarchical observer and the centralized observer, the following error is calculated for every state estimated by each observer

$$error = \frac{1}{N}\sum_{k=0}^{N}\left|\frac{x_k - \hat{x}_{k|k}}{x_k}\right|, \tag{4.1}$$

where N is the total number of time steps of the simulation. In other words, equation (4.1) represents the average of the normalized estimation error. Figure 4.12 shows these errors for the 39 states estimated by the centralized observer. The dashed line represents the average of these errors over all states. As shown in Figure 4.12, this value is 0.0126 for the centralized observer. Figure 4.13 shows these errors for the 77 states estimated by the hierarchical observer at all levels of the hierarchy. Thus, the errors of the first 39 states correspond to the errors of the 4 local observers at the lowest level of the hierarchy. The errors corresponding to state 40 until state 60 represent the errors of the states estimated by the second-level observers (i.e. the observers of SS5 and SS6 in Figure 4.5). And the errors of the last 17 states correspond to the errors of the states estimated by the top-level observer.

As shown in Table 4.1, the mean $error$ and max $error$ of the centralized observer are 44% and 75.4% lower than the overall mean $error$ and max $error$ of the hierarchical observer, respectively. Table 4.2 provides a comparison between the overall estimation accuracy of the centralized observer and the estimation accuracy of the hierarchical observer at each level of the hierarchy. It can be seen that, on average, the estimation accuracy of the hierarchical observer at the first level of the hierarchy is higher than the overall estimation accuracy of the centralized observer. This might be due to the higher number of measured data per number of estimated states for the lowest-level observers of the hierarchical observer. For example, the observer of SS1 estimates 9 states using 3 sensors to measure the internal states of the subsystem, whereas the centralized observer uses 9 sensors to estimate 39 states. A higher estimation accuracy can be achieved by increasing the number of sensors. However, this case study shows that, for the same relatively low total number of sensors used by each observer, the hierarchical observer can reach

a higher estimation accuracy at the lowest level of the hierarchy compared to a centralized observer. Furthermore, as shown in Figure 4.13, as the level of the hierarchy increases, the estimation accuracy of the hierarchical observer decreases since the update rates of local observers decrease. Whereas, in the centralized observer, the errors are more homogeneous as shown in Figure 4.12.

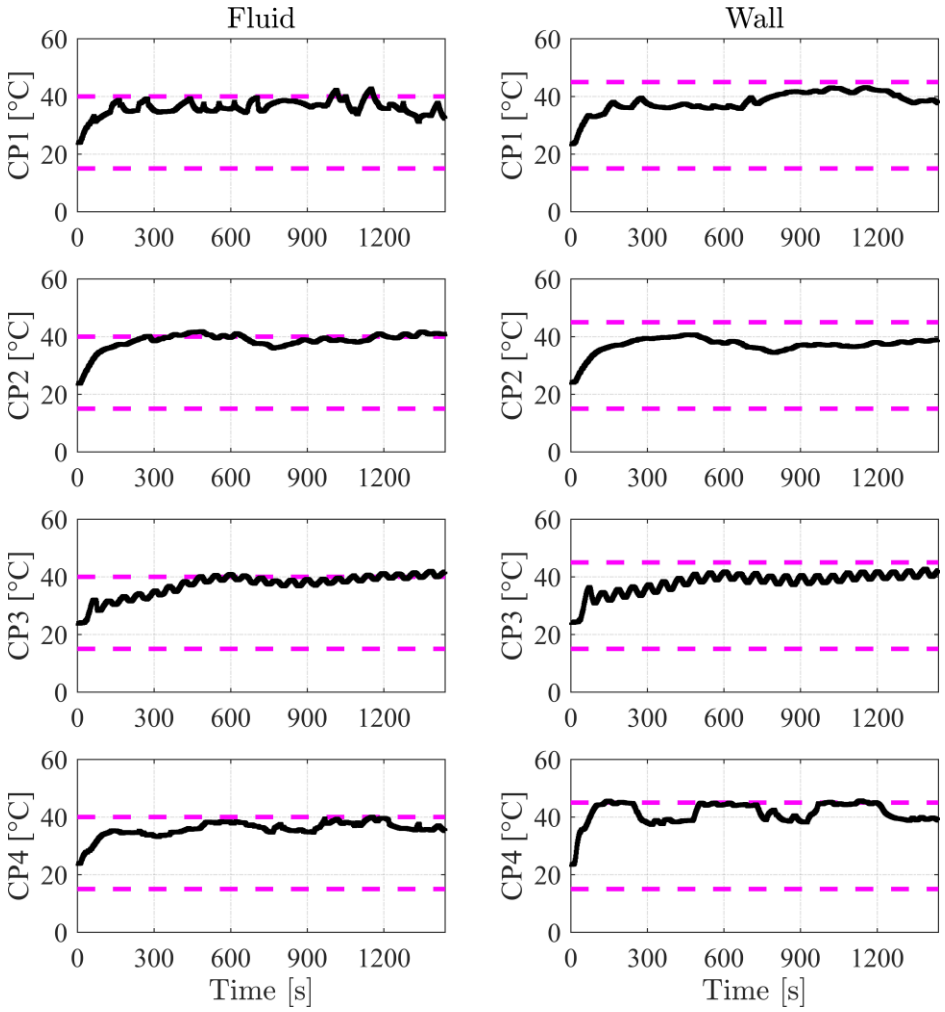

Figure 4.11 Fluid and wall temperature of the 4 cold plates – experimental results.

However, the higher estimation accuracy achieved by the centralized framework comes at the expense of an increase in the computational power required to run the observer. A Kalman filter algorithm has a complexity order of $\mathcal{O}(4n^3)$ where n is the number of the estimated states. A detailed analysis of the complexity of each step of the algorithm can be found in [89]. Therefore, in the centralized Kalman filter case where n is 39, the complexity of the algorithm is

of order $\mathcal{O}(237276)$. However, in the hierarchical estimation case, the overall complexity drops to $\mathcal{O}(44636)$ as shown in equation (4.2), which results in 5.3 times complexity reduction.

$$\begin{aligned}&\mathcal{O}(4\times 9^3)\times 3+\mathcal{O}(4\times 12^3)+\mathcal{O}(4\times 10^3)\\&+\mathcal{O}(4\times 11^3)+\mathcal{O}(4\times 17^3)=\mathcal{O}(44636).\end{aligned} \tag{4.2}$$

Consequently, even though the hottest states in the system did not violate their constraints when estimated by a centralized observer as shown in Figure 4.14, the controller failed to compute an input to the system in the sample time allotted for several instances highlighted in Figure 4.15. In these instances, the applied loads are set to zero for safety.

4.8 Comparison to a Decentralized Observer

This section compares the hierarchical observer designed in this chapter to a conventional decentralized observer that completely ignores coupling information between subsystems. To perform this comparison, a decentralized observer of 4 independent local Kalman filters is designed. Each local observer estimates the dynamics of 1 fluid loop of the testbed presented in Figure 4.1 and Figure 4.2 using a full-order graph-based model of that loop. That is, each local Kalman filter uses 1 of the 4 graph-based models from the lowest level of the hierarchical model presented in Figure 4.4. Constant values of zero are used to compensate for subsystem interactions (i.e. sink states of each subsystem graph-based model). All 4 local observers are designed to update every 2s (i.e. the same update rate of the lowest-level observers of the hierarchical observer and the update rate of the centralized observer designed in previous sections). Additionally, the local observers are designed using the same number and placement of temperature sensors used by the hierarchical observer and the centralized observer. That is, the local observer of FL1 (i.e. SS1) uses 3 temperature sensors to measure states 1, 5, and 7. The local observers of FL2 and FL3 uses 2 sensors each to measure states 1 and 5 of their subsystems. Finally, the local observer of FL4 uses 2 sensors to measure states 1 and 8 of its subsystem.

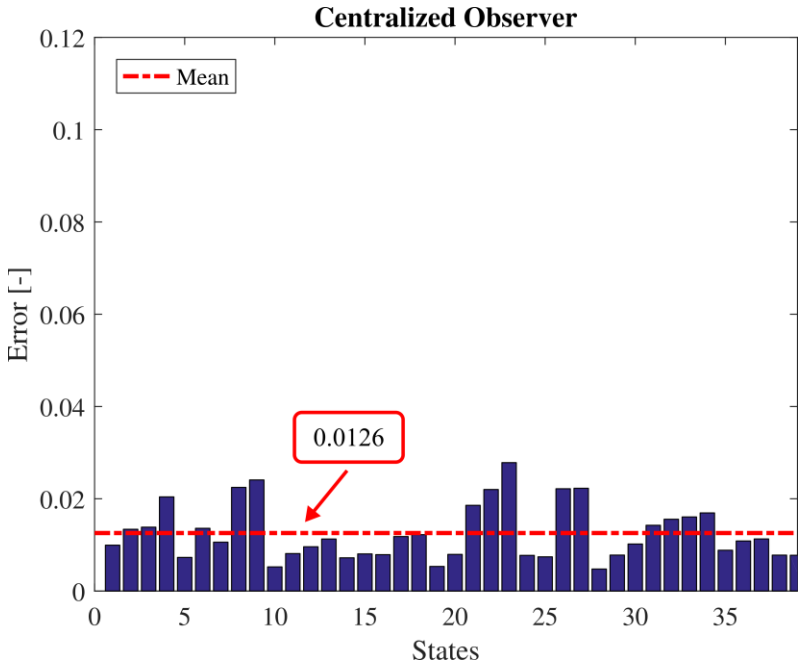

Figure 4.12 Mean of the normalized error of each state estimated by the centralized observer.

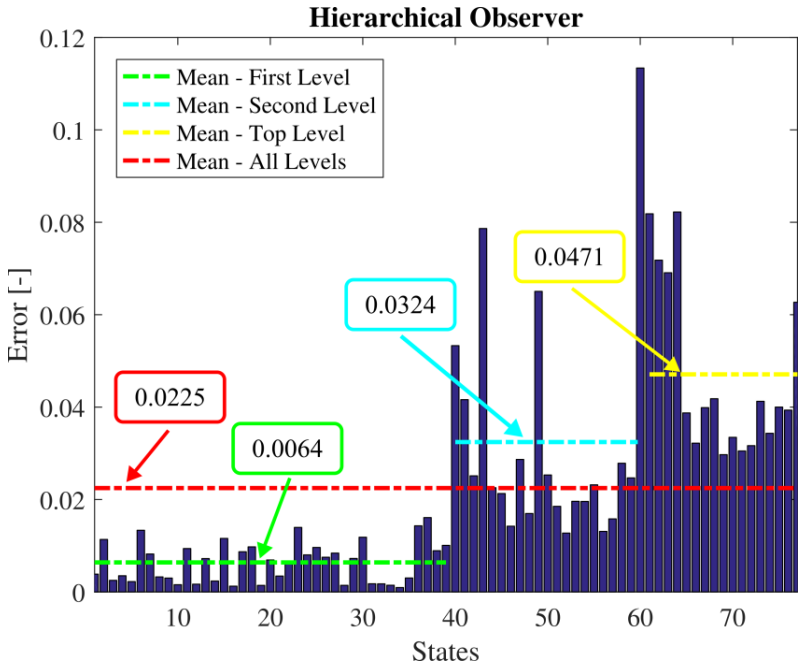

Figure 4.13 Mean of the normalized error of each state estimated by the hierarchical observer.

Table 4.1 Comparison between the overall estimation accuracies of the hierarchical observer and the centralized observer.

	Hierarchical	Centralized	Percent Decrease
Mean *error*	0.0225	0.0126	44%
Max *error*	0.113	0.0278	75.4%

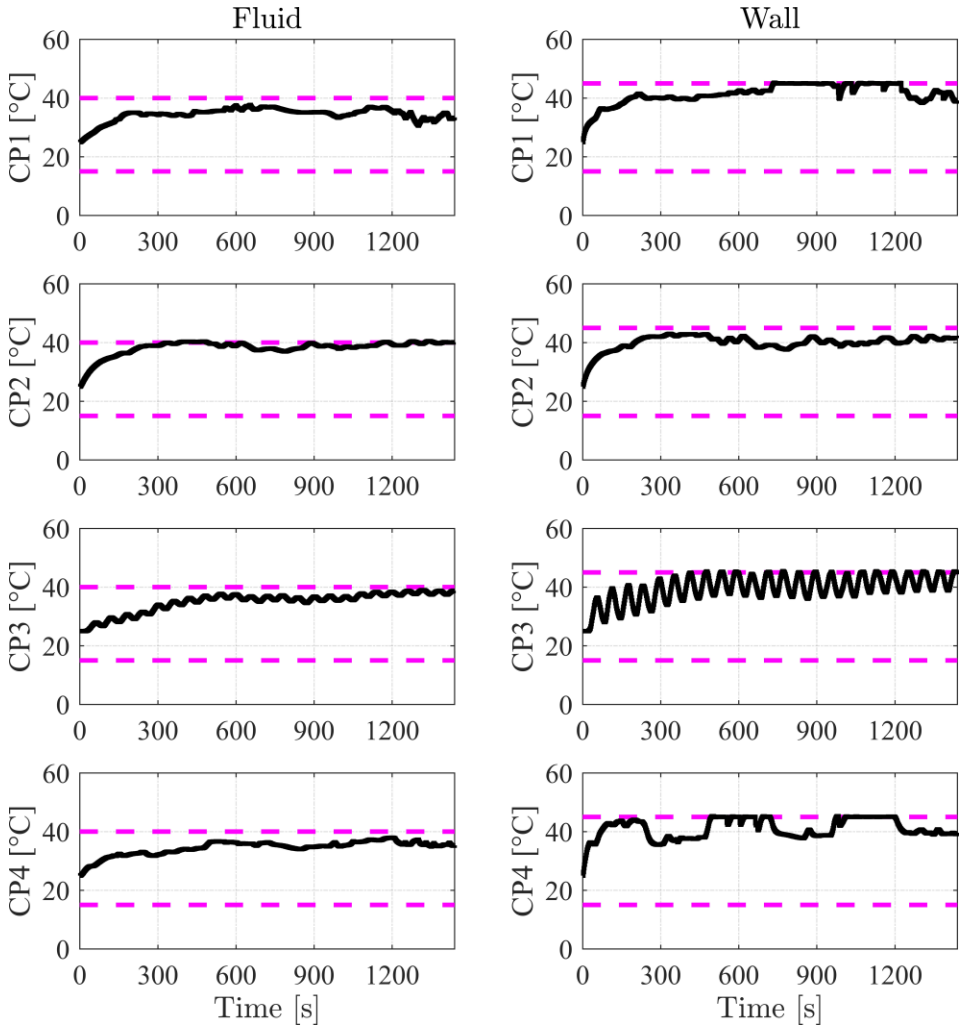

Figure 4.14 Fluid and wall temperatures of the 4 cold plates – simulation (centralized observer).

Table 4.2 Comparison between the overall estimation accuracy of the centralized observer and the estimation accuracy of the hierarchical observer at each level of the hierarchy.

	Hierarchical		Centralized	Percent Decrease
Mean *error*	Level 1	0.0064	0.0126	-96.88%
	Level 2	0.0324		61.11%
	Top Level	0.0471		73.25%
Max *error*	Level 1	0.0161	0.0278	-72.67%
	Level 2	0.0787		64.68%
	Top Level	0.113		75.4%

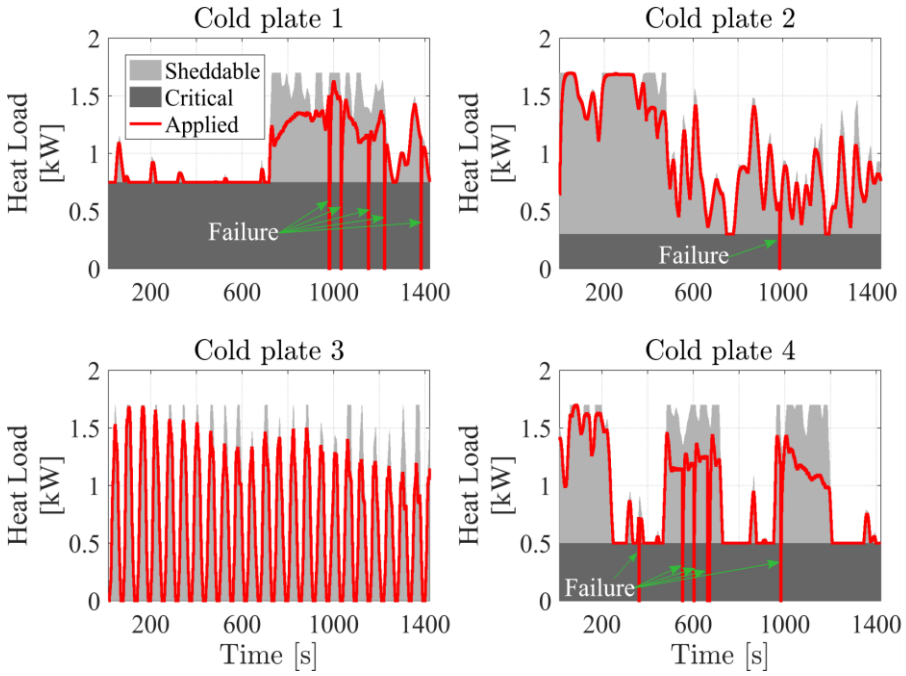

Figure 4.15 Desired versus applied loads using a centralized observer – simulation.

Figure 4.16 shows the normalized estimation errors of the 39 states of the full-order graph-based model estimated by the 4 independent local Kalman filters of the decentralized observer. The average of these errors over all states is 0.4532 as shown by the dashed red line in the figure. Table 4.3 compares the overall mean and max *error* of the decentralized and the hierarchical observers. Table 4.4 compares the overall mean and max *error* of the decentralized observer to the mean and max *error* of the hierarchical observer at each level of the hierarchy. The results presented in Figure 4.16 and Tables 4.3 and 4.4 show the significant reduction in the estimation accuracy of the decentralized observer compared to the hierarchical observer. This reduction is a result of ignoring subsystem interactions. Finally, the overall computational complexity of the decentralized obsevrer (i.e. $\mathcal{O}(4\times 9^3)\times 3+\mathcal{O}(4\times 12^3)=\mathcal{O}(15660)$) is 2.85 times smaller than the overall estimation accuracy of the hierarchical observer designed in this chapter. However, this reduction in computational complexity is accompanied by a much bigger reduction in estimation accuracy that prohibits successful control desgin.

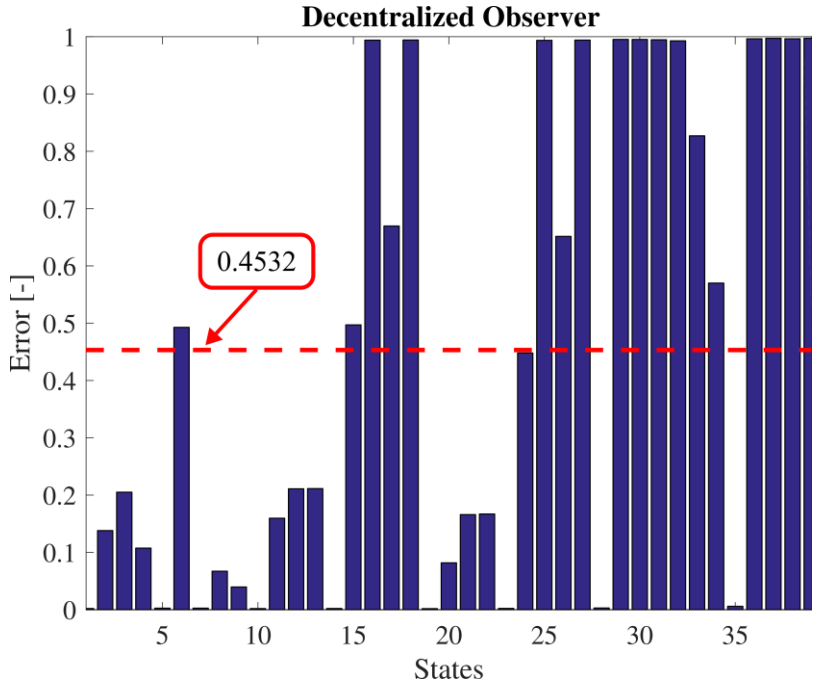

Figure 4.16 Mean of the normalized error of each state estimated by the decentralized observer.

Table 4.3 Comparison between the overall estimation accuracies of the hierarchical observer and the decentralized observer.

	Hierarchical	Decentralized	Percent Decrease
Mean *error*	0.0225	0.4532	-1914%
Max *error*	0.113	1	-784.96%

Table 4.4 Comparison between the overall estimation accuracy of the decentralized observer and the estimation accuracy of the hierarchical observer at each level of the hierarchy.

	Hierarchical		Decentralized	Percent Decrease
Mean *error*	Level 1	0.0064	0.4532	-6981%
	Level 2	0.0324		-1299%
	Top Level	0.0471		-862.2%
Max *error*	Level 1	0.0161	1	-6111%
	Level 2	0.0787		-1171%
	Top Level	0.113		-784.96%

4.9 Conclusion

This chapter presented a case study in which a Kalman filter-based hierarchical observer is connected to a hierarchical model predictive controller designed to manage the dynamics of a candidate fluid-thermal management system for electrified vehicles. Simulation and real-time experimental results showed that the hierarchical observer can be used to accurately estimate both component-level and system-level dynamics. Furthermore, a comparison between the proposed hierarchical observer and a centralized Kalman filter showed that, as expected, a better estimation accuracy can be achieved using a centralized observer. However, the computational complexity of the centralized observer was more than 5 times bigger than that of a hierarchical

observer designed according to the framework proposed in this dissertation. This increase in the computational load can be a constraint in many practical implementations. Finally, a comparison between the hierarchical observer designed in this chapter and a conventional Kalman filter-based decentralized observer showed that the decentralized observer is less computationally expensive. However, as a result of ignoring subsystem interactions, this reduction in computational complexity is accompanied by a huge reduction in estimation accuracy that can prevent successful control design.

Chapter 5

Robustness Analysis

5.1 Motivation and Background

The drawbacks of centralized and decentralized estimation algorithms motivated the development of many distributed [74], [75], [90], [91] and hierarchical estimation algorithms [51], [63], [76], [78]. Compared to a centralized design that suffers from a single point of failure, the inherent redundancy achieved by distributed and hierarchical algorithms increases the survivability of these frameworks. That is, the failure of a local observer in a hierarchical or distributed network can lead to a gradual degradation in the estimation accuracy rather than a complete failure of the overall observer.

In distributed architectures, the estimation problem is solved by a network of observers that update at the same rate and asymptotically estimate the dynamics of a system based on partial information from their neighbors. Additionally, many systems are characterized by separable timescale dynamics (e.g. slow and fast dynamics). The dynamic behaviors of such systems can be estimated by hierarchical estimation algorithms that consist of a network of observers updating at multiple timescales (see Chapter 3).

While distributed and hierarchical estimation algorithms offer many benefits compared to conventional designs, they also create new challenges that need to be overcome in order to provide accurate and reliable state estimates. A fault in a hierarchical or distributed observer can propagate in the network and negatively impact the dynamics of an entire physical system by communicating inaccurate estimates to its controllers. This is particularly dangerous for safety

critical systems such as electrified vehicles. The focus of this chapter is to analyze the robustness of the hierarchical estimation algorithm proposed in this dissertation (i.e. chapters 3 and 4).

Many fault-tolerant distributed estimation algorithms exist in the literature [74], [75], [90]–[92]. For example, in [93], robustness to sensor faults or attacks is achieved using an L_1-norm on the terms affected by the fault. However, security and robustness of hierarchical estimation algorithms require special attention. In contrast to distributed estimation algorithms, a hierarchical observer includes a global observer at the top-level of the hierarchy that inherently captures coupling among all subsystems. That is, the global observer at the top level is the main source of coupling information received by all lower-level observers in the hierarchy. Additionally, as derived in Chapter 3, there is a direct coupling between the stability and accuracy of the top-level observer and the lower-level observers in the hierarchy.

This chapter numerically examines the robustness of the 3-level hierarchical observer of the FTMS developed in section 4.4 with respect to

a. inilization errors,
b. faulty pseudo-measurements received by the top-level observer,
c. fautly sensor readings received by the lowest-level observers, and
d. tuning parameters.

The remainder of this chapter is organized as follows. The robustness of the overall hierarchical observer to faults at the top level of the hierarchy is presented in section 5.2. Section 5.3 compares the robustness of the proposed hierarchical observer and a conventional centralized observer to faulty physical sensor readings. The robustness of the proposed hierarchical observer to initialization errors is presented in section 5.4. The effect of the tuning parameters of each observer in the hierarchy on the estimation accuracy of the overall observer is presented in section 5.5. Conclusions are presented in section 5.6.

5.2 Robustness to Faults at The Top Level of The Hierarchy

This section investigates the impacts of faults at the top level of the hierarchy on the estimation accuracy of the overall proposed hierarchical observer. Faults are created by intentionally sending corrupted pseudo-measurements to the top-level observer. Specifically, subsection 5.2.1 explores the robustness of the hierarchical observer when pseudo-measurements

sent to the top-level observer are corrupted by additive incipient faults and subsection 5.2.2 explores the robustness of the hierarchical observer when the same pseudo-measurements are corrupted by additive abrupt faults.

5.2.1 Incipient Faults

In the case study presented in this subsection, all pseudo-measurements received by the global observer at the top level of the hierarchy are intentionally corrupted by the additive incipient fault presented in Figure 5.1. That is, at the end of the simulation, the incipient faults increase the actual value of each pseudo-measurement by around 35%. The resulting normalized estimation error of each state of the hierarchical observer is presented in Figure 5.2. The green, blue, and yellow dashed lines represent the average of the errors of first-level, second-level, and top-level states, respectively. Additionally, the red dashed line represents the average of the errors of all 77 states. Compared to the non-faulty scenario presented in Chapter 4 (i.e. Figure 4.13), around a 97% increase in the overall mean error (i.e. red dashed line) is shown in Figure 5.2. Additionally, the average estimation error increased by 20%, 6%, and 199% at the first (i.e. green dashed line), second (i.e. blue dashed line), and top level (i.e. yellow dashed line) of the hierarchy as shown in Figure 5.2. Nevertheless, the average estimation error remains below 1% at the lowest level and around 3% at the second level of the hierarchy. The simulated and estimated values of state 7 from SS2 (i.e. at the lowest level), state 2 from SS6 (i.e. at the second level), and state 6 from the top-level model (see Figure 4.4) are compared in Figure 5.3. Consequently, Figure 5.2 and Figure 5.3 demonstrate that, in the presence of an incipient fault that causes an average estimation error of 14% at the top level of the hierarchy, reliable state estimates can still be obtained from first-level and second-level local observers.

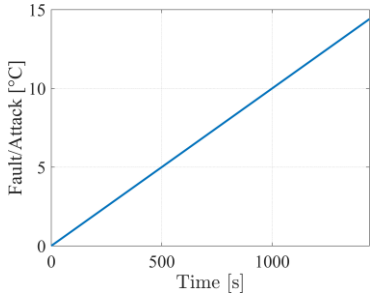

Figure 5.1 Profile of the incipient fault added to the pseudo-measurements received by the global observer at the top level of the hierarchy.

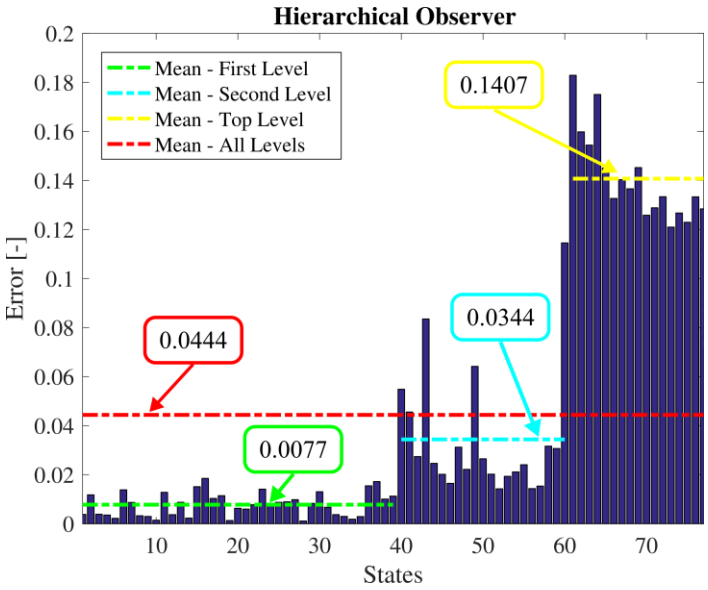

Figure 5.2 Mean of the normalized estimation error of each state of the hierarchical observer when the pseudo-measurements received by the top-level observer are corrupted by the additive incipient fault presented in Figure 5.1.

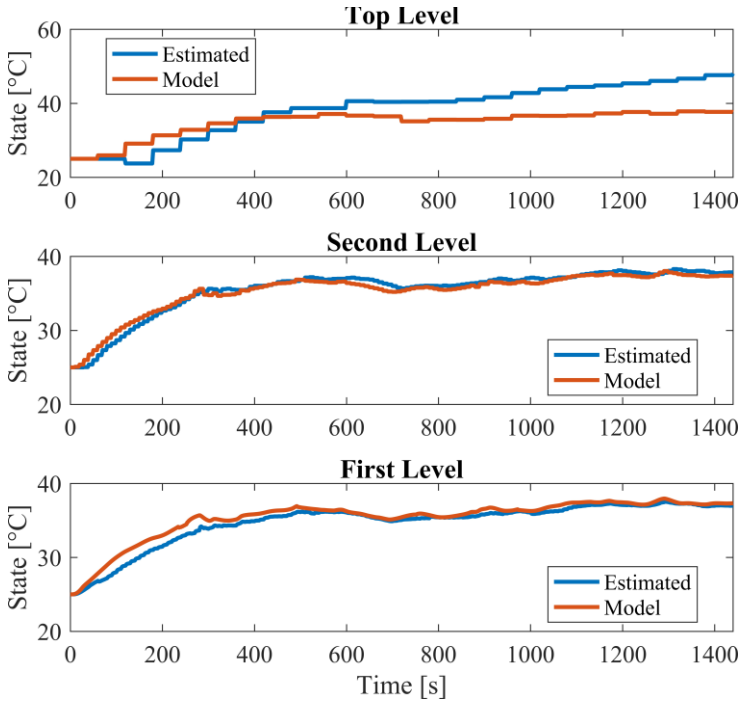

Figure 5.3 Performance of the hierarchical observer at all levels of the hierarchy when faulty pseudo-measurements corrupted by the incipient fault presented in Figure 5.1 are received by the top-level observer.

5.2.2 Abrupt Faults

In the case study presented in this subsection, all pseudo-measurements received by the global observer at the top level of the hierarchy are intentionally corrupted by the additive abrupt fault presented in Figure 5.4. This fault increases the value of each pseudo-measurement by around 25% for the first 600s of the simulation, then the value of the fault goes to zero for the rest of the simulation. The resulting means of the normalized estimation errors of the hierarchical observer are presented in Figure 5.5. Compared to the non-faulty scenario (i.e. Figure 4.13), Figure 5.5 shows around a 62% increase in the overall mean error (i.e. red dashed line), and 19%, 4%, and 125% increase in the average estimation error at the first (i.e. green dashed line), second (i.e. blue dashed line), and top levels (i.e. yellow dashed line) of the hierarchy, respectively. However, similar to the conclusions derived from the previous case study (i.e. subsection 5.2.1), Figure 5.5 and Figure 5.6 show that the failure of the overall observer is gradual and accurate state estimates can be obtained from the first-level and second-level observers even in the presence of faults at the top level of the hierarchy. Specifically, Figure 5.5 shows that, on average, the estimation error is below 1% at the lowest level and around 3% at the second level of the heirarchy. This survivabilty is enabled by the inherent redundancy achieved by the hierarchical network.

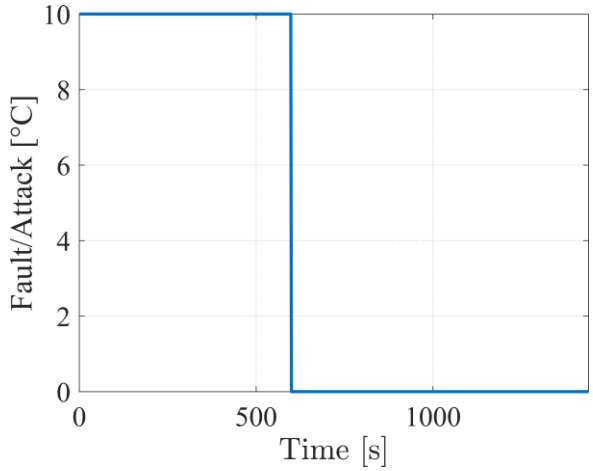

Figure 5.4 Profile of the abrupt fault added to the pseudo-measurements received by the global observer at the top level of the hierarchy.

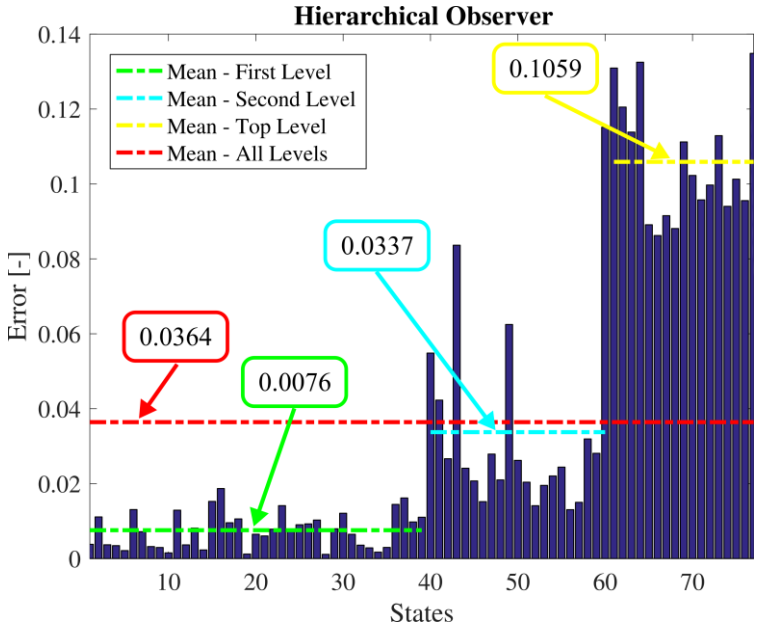

Figure 5.5 Mean of the normalized estimation error of each state of the hierarchical observer when the pseudo-measurements received by the top-level observer are corrupted by the additive abrupt fault presented in Figure 5.4.

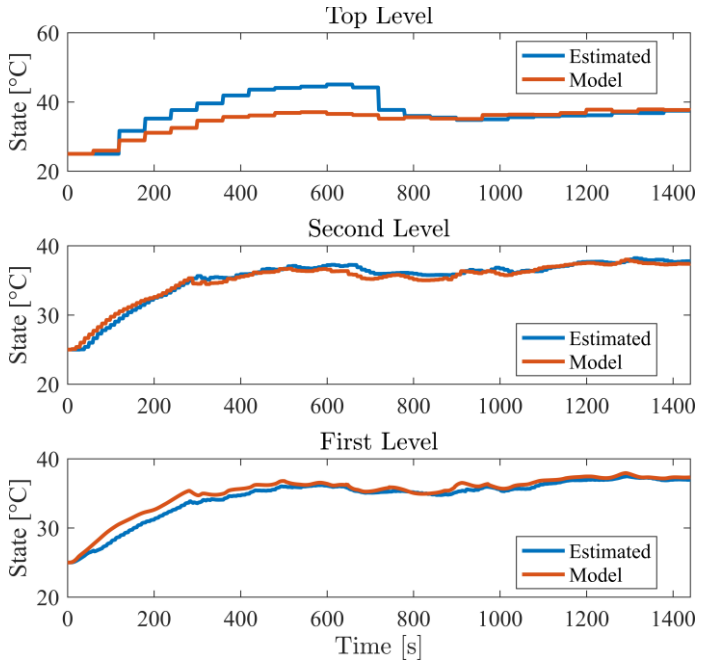

Figure 5.6 Performance of the hierarchical observer at all levels of the hierarchy when faulty pseudo-measurements corrupted by the abrupt fault presented in Figure 5.5 are received by the top-level observer.

5.3 Robustness to Faults at The Lowest Level of The Hierarchy

As described in section 3.3, only local observers at the lowest level of the hierarchy have direct access to physical sensor readings and every upper-level observer in the network treats local state estimates received from lower-level observers as pseudo-measurements. Therefore, the estimation accuracy at the lowest level of the hierarchy is critical to the overall stability and convergence of the proposed hierarchical observer. This section explores the robustness of the overall hierarchical observer to failures at the lowest level of the hierarchy. This is achieved by intentionally corrupting physical sensor readings received by lowest-level observers. Robustness to two types of faults is investigated. In subsection 5.3.1, physical sensor readings are corrupted by additive incipient faults. In subsection 5.3.2, physical sensor readings are corrupted by additive abrupt faults. Additionally, for both case studies, the performance of the benchmark centralized observer designed in Chapter 4 (see section 4.7) is presented.

5.3.1 Incipient Faults

In this case study, all sensor readings used by the observers of SS1, SS2, and SS3 (see section 4.4) are corrupted by the additive incipient fault presented in Figrue 5.1. The sensor readings received by the observer of SS4 are non-faulty. That is, 7 out of the 9 sensors used at the lowest level of the hierarchy (see figure 4.5) are corrupted. Figure 5.7 presents the resulting mean of the normalized estimation error of each state of the hierarchical observer at all levels of the hierarchy. Compared to the non-faulty scenario presented in Figure 4.13, Figure 5.7 shows around a 486% increase in the overall mean estimation error (i.e. red dashed line), and 1919%, 394%, and 118% increase in the average estimation errors at the first (i.e. green dashed line), second (i.e. blue dashed line), and top levels (i.e. yellow dashed line) of the hierarchy, respectively. The simulated and estimated values of state 7 from SS2, state 2 from SS6, and state 6 from the top-level model (see Figure 4.4) are presented in Figure 5.8. Thus, Figure 5.7 and Figure 5.8 show that, failures at the lowest level of the hierarchy can have a larger impact on the overall estimation accuracy of the hierarchical observer than top-level failures. This can be related to the fact that first-level observers use the highest-resolution models and thus generate the most accurate state estimates in the hierarchy as demonstrated in the results presented in Figure 4.13.

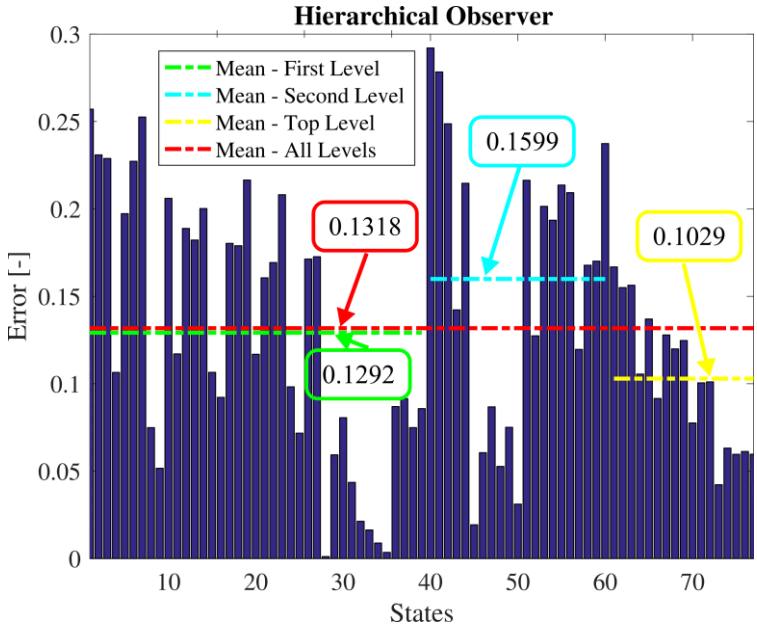

Figure 5.7 Mean of the normalized estimation error of each state of the hierarchical observer when sensor readings received by lowest-level observers are corrupted by the incipient fault presented in Figure 5.1.

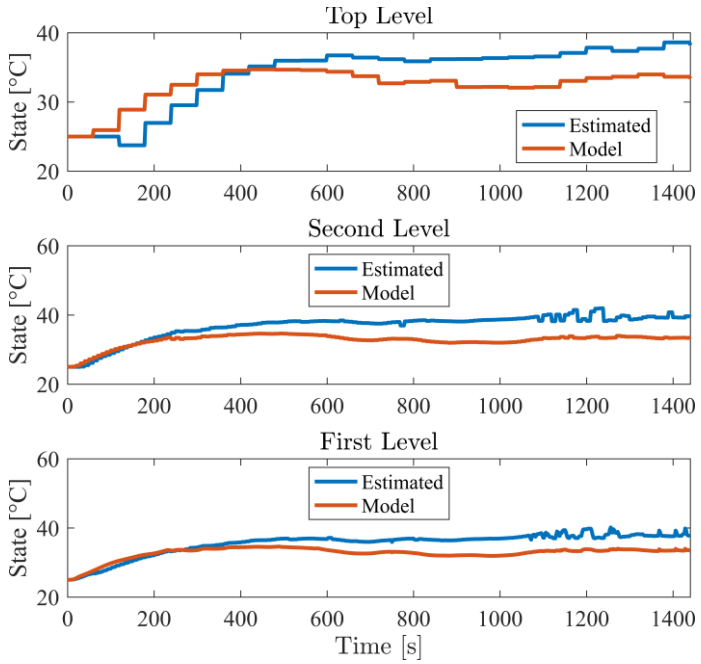

Figure 5.8 Performance of the hierarchical observer at all levels of the hierarchy when faulty sensor readings corrupted by the incipient fault presented in Figure 5.1 are received by lowest-level observers.

To examine the performance of a benchmark centralized observer operating under the same conditions, the centralized Kalman filter designed in Chapter 4 (see section 4.7) is tested using the same corrupted sensor readings. That is, 7 out of the 9 sensor readings used by the centralized observer are corrupted with the additive incipient fault presented in Figure 5.1. Figure 5.9 presents the resulting mean of the normalized estimation error of each state of the centralized observer. Compared to the non-faulty case study (i.e. Figure 4.12), Figure 5.9 shows around a 937% increase in the overall mean estimation error (i.e. red dashed line). Additionally, by comparing Figure 5.7 and Figure 5.9, it can be deduced that, for this case study, the hierarchical and the centralized observers are equally robust to the faulty sensor readings. Specifically, both observers have similar overall estimation accuracies, and the average estimation error of the hierarchical observer at the lowest level of the hierarchy is around 1% lower than the overall estimation accuracy of the centralized observer.

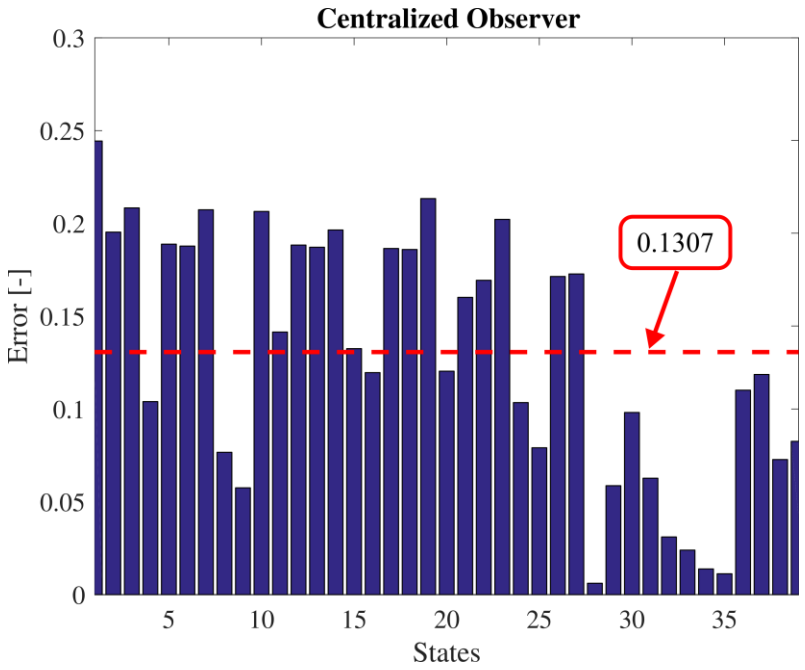

Figure 5.9 Mean of the normalized estimation error of each state of the centralized observer when sensor readings are corrupted by the additive incipient fault presented in Figure 5.1.

5.3.2 Abrupt Faults

Robustness of the proposed hierarchical and the benchmark centralized observers to faulty sensor readings corrupted by abrupt faults is analyzed in this subsection. Specifically, in this case study, all sensor readings used by the observers of SS1, SS2, and SS3 at the lowest level of the hierarchy (see Figure 4.4), and the equivalent 7 sensor readings used by the centralized observer are corrupted by the abrupt fault presented in Figure 5.4. The resulting mean of the normalized estimation error of each state of the hierarchical and the centralized observers is presented in Figure 5.10 and Figure 5.11, respectively. These results show that, for this case study, the overall mean of the normalized estimation errors of the hierarchical observer (i.e. red dashed line in Figure 5.10) is around 8% larger than that of the centralized observer (i.e. red dashed line in Figure 5.11). This can be due to the faster convergence achieved by the centralized observer (compared to the hierarchical observer) after the fault is resolved. Specifically, Figure 5.12 compares the simulated values of state 7 from SS2, state 2 from SS6, and state 6 from the top-level model (see Figure 4.4) to their estimated values obtained from the hierarchical observer, and Figure 5.13 compares state 7 from SS2 (i.e. the same first-level state presented in Figure 5.12) to its estimated value obtained from the benchmark centralized observer. The results presented in Figure 5.12 and Figure 5.13 demonstrate that a faster convergence is achieved by the centralized observer at 600s (i.e. after the fault is resolved). Additionally, Figure 5.12 show that as the level of the hierarchy increases, the convergence rates of the observers in the hierarchy decreases. Finally, the results of this case study show that, the performance of the centralized observer is equivalent to the performance of the hierarchical observer at the lowest level of the hierarchy. Specifically, the average of the estimation errors of the lowest-level states of the hierarchical observer (i.e. red dashed line in Figure 5.10) is around 1% lower than the average of the estimation errors of the centralized observer (i.e. red dashed line in Figure 5.11).

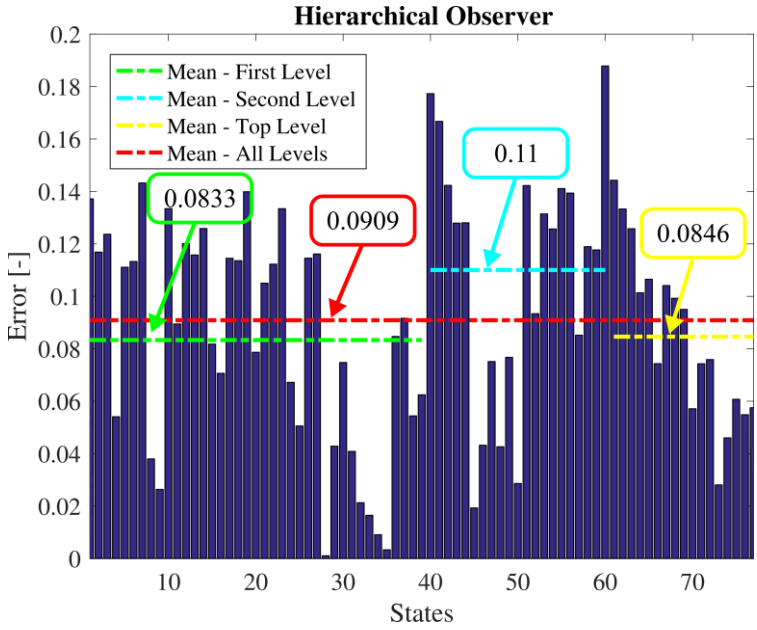

Figure 5.10 Mean of the normalized estimation error of each state of the hierarchical observer when sensor readings received by lowest-level observers are corrupted by the abrupt fault presented in Figure 5.4.

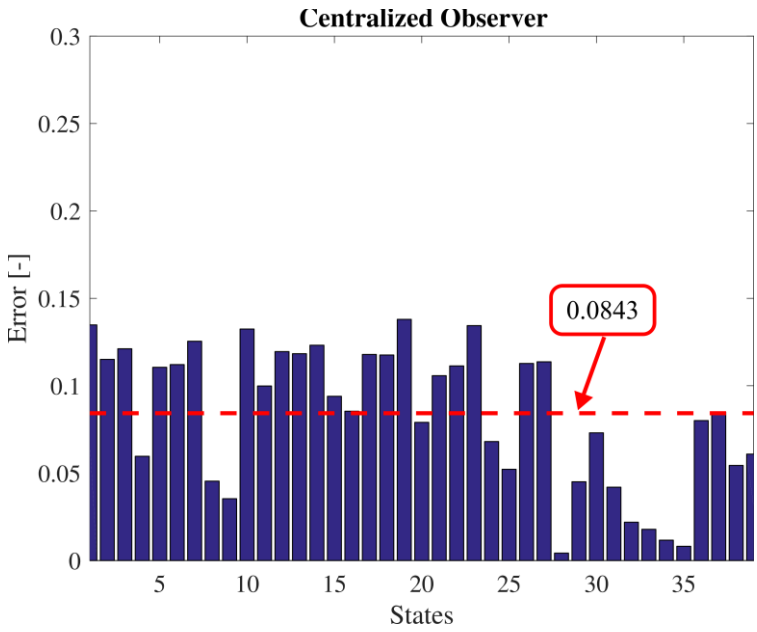

Figure 5.11 Mean of the normalized estimation error of each state of the benchmark centralized observer when its sensor readings are corrupted by the abrupt fault presented in Figure 5.4.

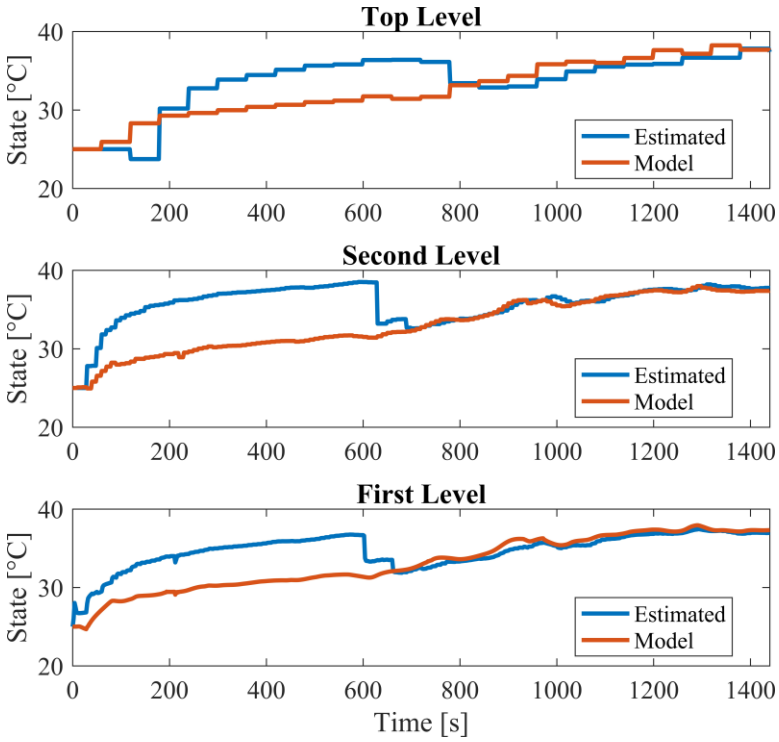

Figure 5.12 Performance of the hierarchical observer at all levels of the hierarchy when sensor readings corrupted by the abrupt fault presented in Figure 5.4 are received by lowest-level observers.

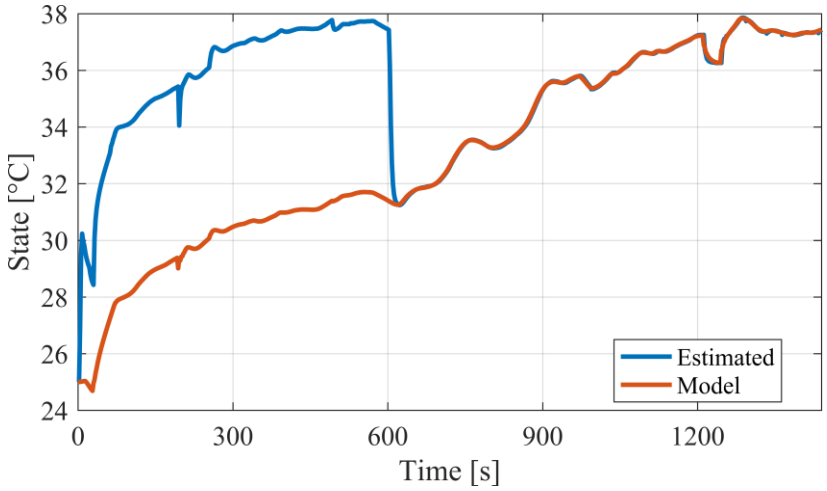

Figure 5.13 Performance of the centralized observer when sensor readings are corrupted by the abrupt fault presented in Figure 5.4.

5.4 Robustness to Initization Errors

This section examines the robustness of the proposed hierarchical observer to initialization errors in the observer states at all levels of the hierarchy. Specifically, a 20% initialization error is introduced to every state of every observer in the hierarchy. Figure 5.14 shows the simulated and the estimated values of state 7 from SS2, state 2 from SS6, and state 6 from the top-level model (see Figure 4.4). These results demonstrate that, the hierarchical observer converges to the actual state values in the presence of the introduced initialization errors at all levels of the hierarchy. Additionally, these results show that, as the level of the hierarchy increases, the convergence rates of the observers decrease. This is directly related to the update rates of the observers. As described in Chapter 3, as the level of the hierarchy increases, the update rates of the observers decrease.

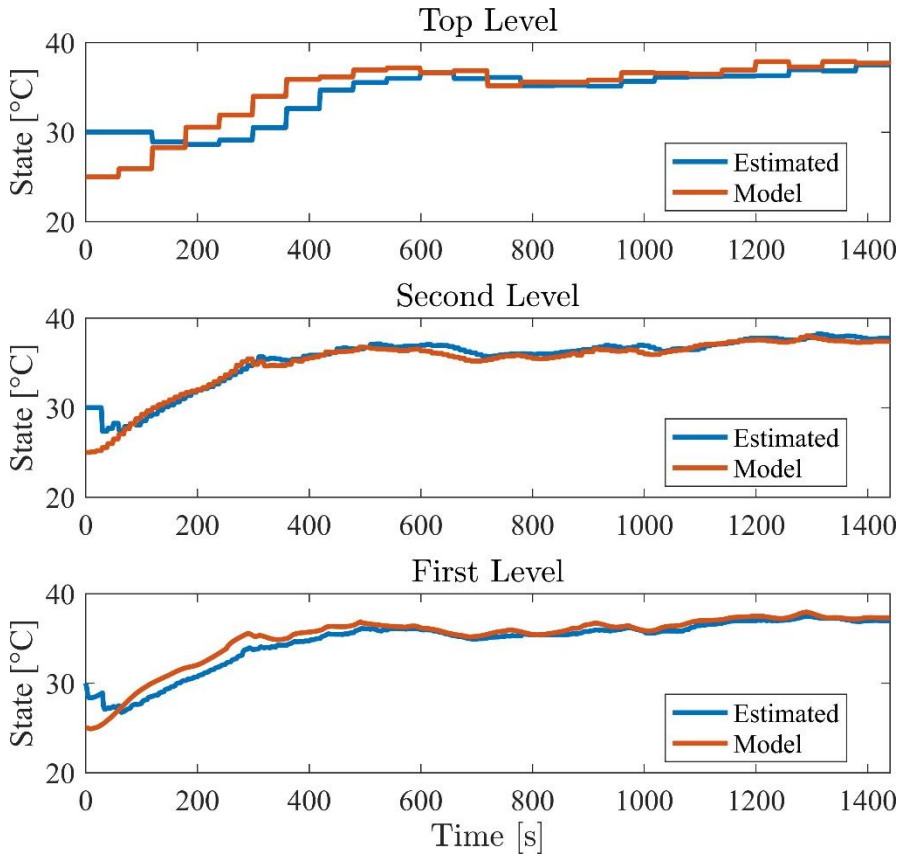

Figure 5.14 Performance of the hierarchical observer when 20% initialization errors are introduced in every observer at all levels of the hierarchy.

5.5 Effect of Tuning Parameters

In this section, the effect of the tuning parameters on the estimation accuracy of each observer in the hierarchy is tested. The tuning parameters are the matrices Q_i (i.e. covariance of the process noise) and R_i (i.e. covariance of the measurement noise) of each observer $_i$ in the hierarchical network. Values with lower estimated uncertainties are trusted more. Larger process noise covariance (i.e. larger Q_i) drives the observer to trust the measurements more than the model. Similarly, larger sensor noise covariance (i.e. larger R_i) drives the observer to trust the model more than the measurements. That is, the relative certainty between the measurements (or pseudo-measurements) and the model is an important factor in the performance of the observer.

Seven different cases are tested in this section. For each case, the values of the chosen parameters are presented in Table 5.1. I represents an identity matrix of appropriate dimensions. Set 7 shows the parameters used in the experimentally validated case study presented in Chapter 4. The performance of the proposed hierarchical observer in these seven cases is presented in Figures 5.15 - 5.21. In each of these figures, green, blue, and yellow dashed lines plot the average of the normalized estimation errors of first-level, second-level, and top-level states, respectively. Additionally, the red dashed lines represent the average of the normalized estimation errors over all 77 states.

Figure 5.15, and Figure 5.17 to Figure 5.21 show that, design sets 1, and 3 to 7 result approximately in the same overall estimation accuracy. Figure 5.16 and Figure 5.18 (i.e. sets 2 and 4) show that the overall performance of the hierarchical observer can be negatively affected if, at upper levels of the hierarchy, the models are trusted more than the pseudo-measurements. This reduction in the overall estimation accuracy is caused by pushing the upper-level observers to rely on reduced-order models rather than pseudo-measurements obtained from lower-level observers that use models of higher-resolutions.

The mean and maximum normalized estimation errors of the benchmark centralized observer (see section 4.7) are 0.0126 and 0.0278, respectively (see Table 4.1), for $Q = R = I$. Thus, Figures 5.15 to 5.21 show that, except for design set 2, the average estimation accuracy of the hierarchical observer at the lowest level of the hierarchy is higher than the overall estimation

accuracy of the centralized observer. Furthermore, Figures 5.15 to 5.21 show a constant trend for the estimation accuracy of the observer with respect to the level of the hierarchy. That is, regardless of the choice of the tuning parameters, the estimation accuracy decreases as the level of the hierarchy increases. This can be related to the update rates and the resolution of the models used by the observers as the level of the hierarchy increases. Specifically, as the level of the hierarchy increases, the update rates and the resolution of the models used by the observers decrease.

Table 5.1 Tuning sets for the proposed hierarchical observer.

		SS1	SS2	SS3	SS4	SS5	SS6	SS7
Set 1	R_i	$0.1I$	$0.1I$	$0.1I$	$0.1I$	$0.01I$	$0.01I$	$0.01I$
	Q_i	$50I$	$50I$	$50I$	$50I$	I	I	I
Set 2	R_i	$10I$	$10I$	$10I$	$10I$	$10I$	$10I$	$10I$
	Q_i	I	I	I	I	I	I	I
Set 3	R_i	I	I	I	I	I	I	I
	Q_i	$10I$	$10I$	$10I$	$10I$	$10I$	$10I$	$10I$
Set 4	R_i	$10I$	$10I$	$10I$	$10I$	I	I	$5I$
	Q_i	I	I	I	I	$5I$	$5I$	$10I$
Set 5	R_i	I	I	I	I	$5I$	$5I$	$10I$
	Q_i	$10I$	$10I$	$10I$	$10I$	$20I$	$20I$	$30I$
Set 6	R_i	$10I$	$10I$	$10I$	$10I$	$5I$	$5I$	I
	Q_i	I	I	I	I	$5I$	$5I$	$10I$
Set 7	R_i	$0.1I$	$0.1I$	$0.1I$	$0.1I$	$0.01I$	$0.01I$	I
	Q_i	$50I$	$50I$	$50I$	$50I$	I	I	I

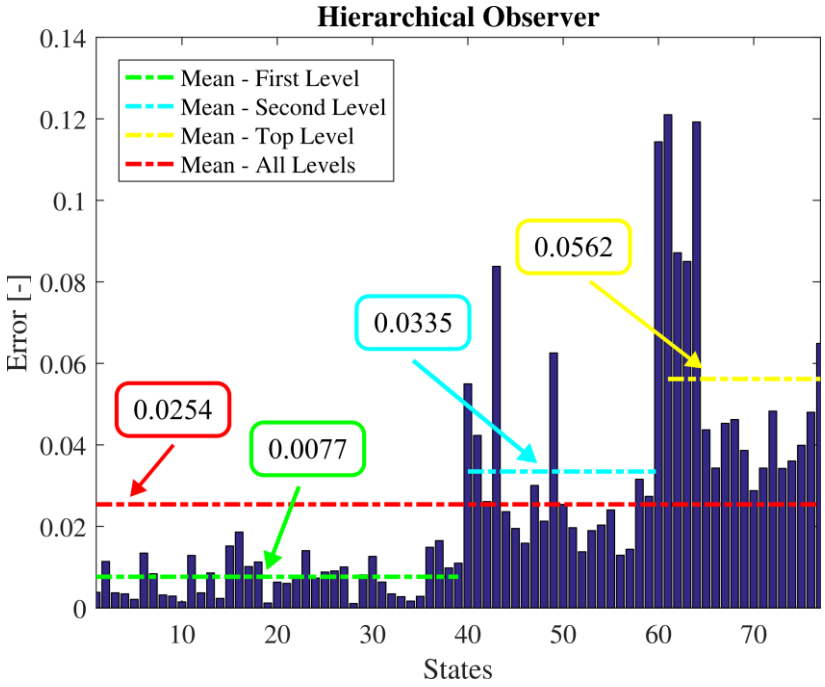

Figure 5.15 Mean of the normalized error of each state estimated by the hierarchical observer – Set 1.

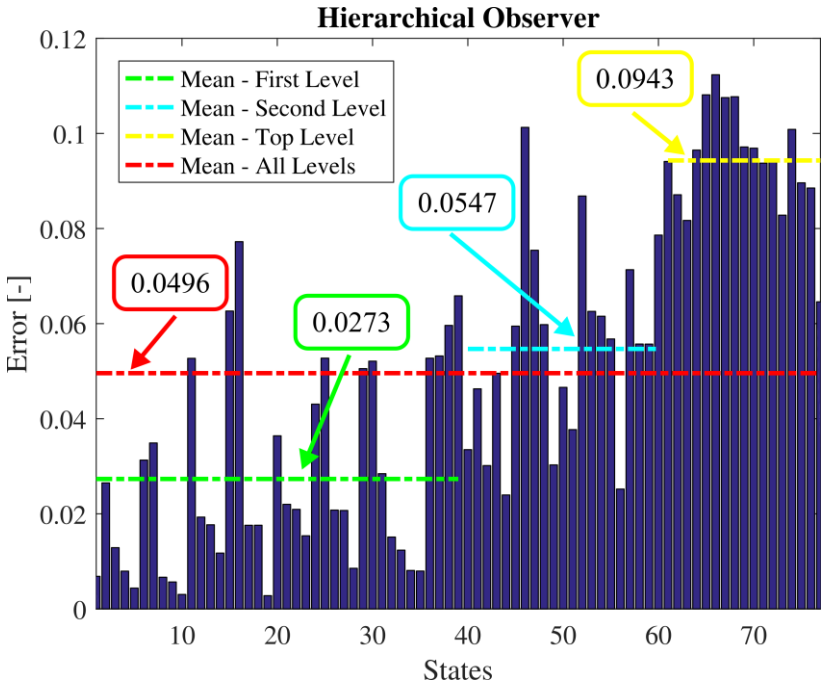

Figure 5.16 Mean of the normalized error of each state estimated by the hierarchical observer – Set 2.

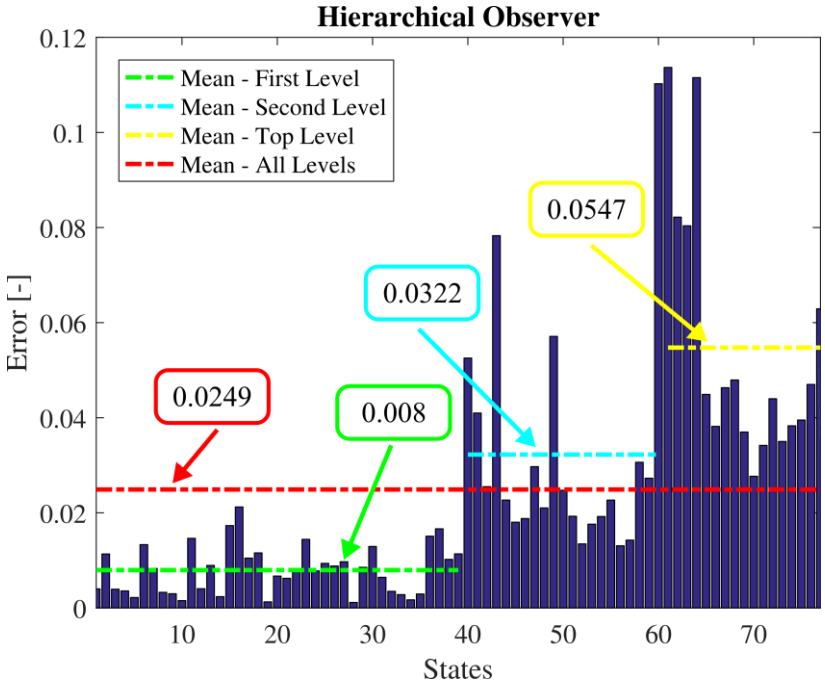

Figure 5.17 Mean of the normalized error of each state estimated by the hierarchical observer – Set 3.

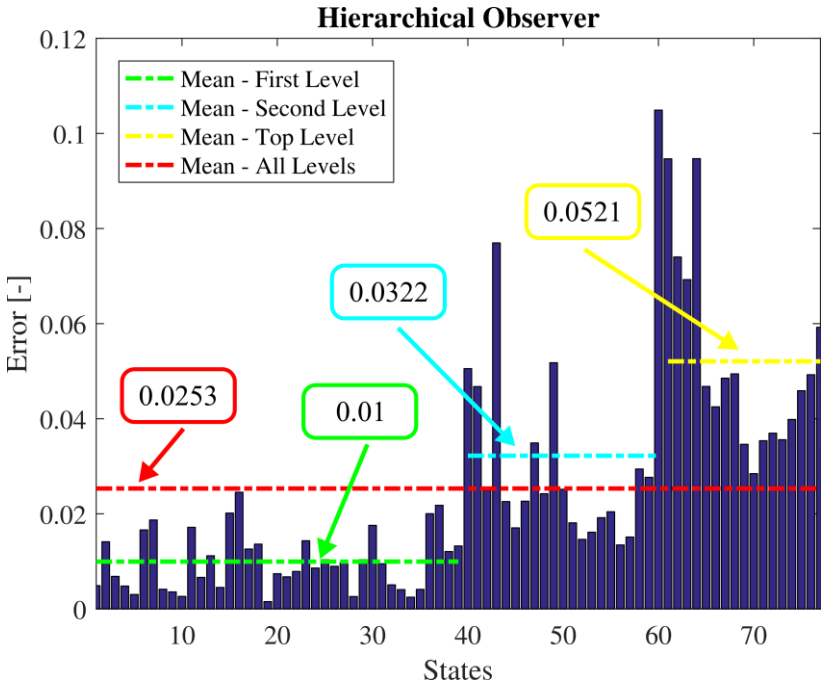

Figure 5.18 Mean of the normalized error of each state estimated by the hierarchical observer – Set 4.

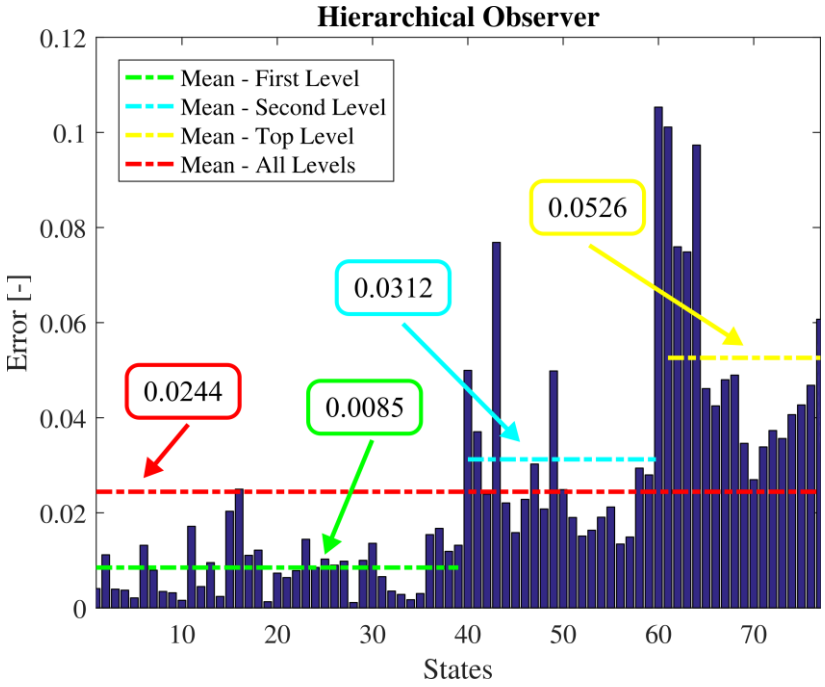

Figure 5.19 Mean of the normalized error of each state estimated by the hierarchical observer – Set 5.

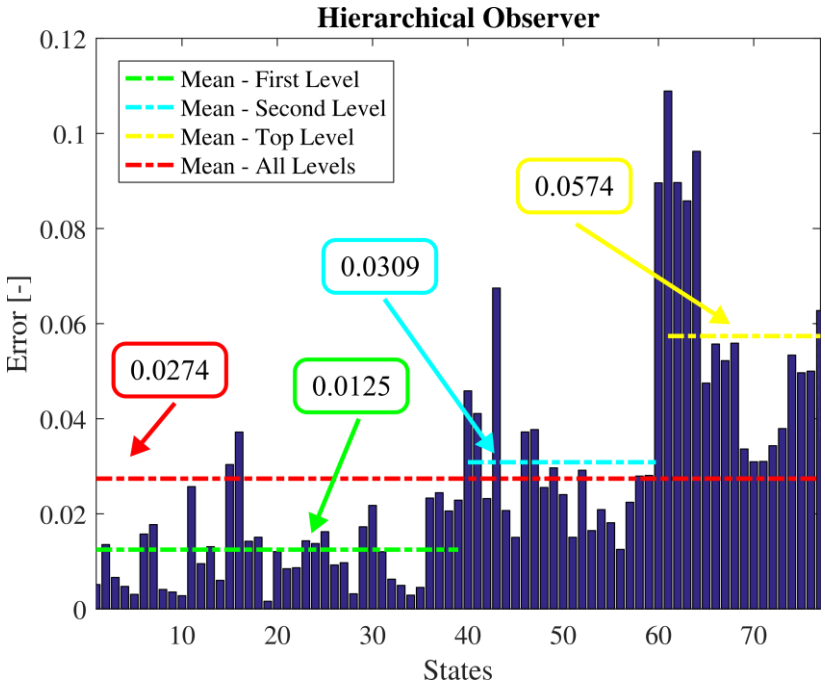

Figure 5.20 Mean of the normalized error of each state estimated by the hierarchical observer – Set 6.

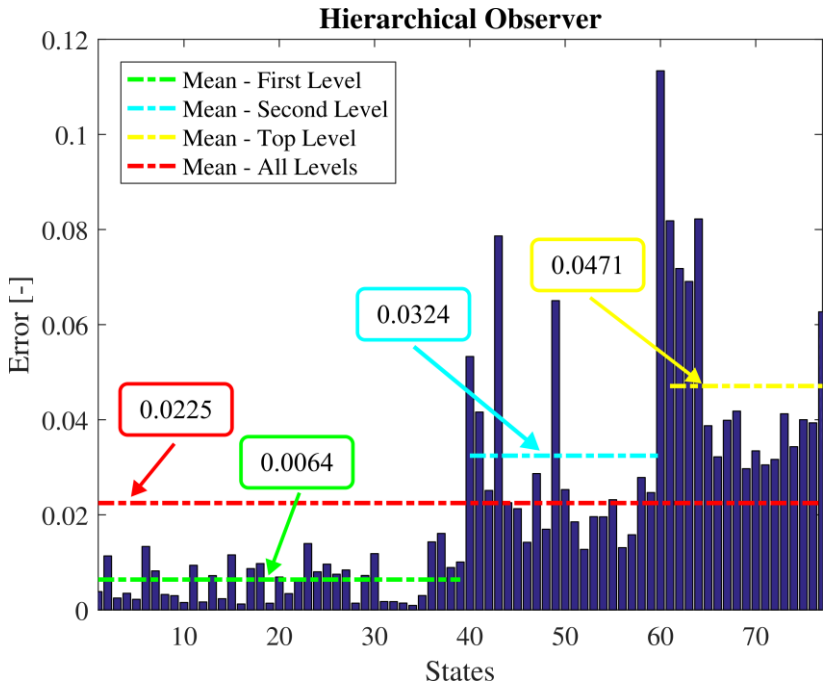

Figure 5.21 Mean of the normalized error of each state estimated by the hierarchical observer – Set 7.

5.6 Conclusion

This chapter presented several case studies that numerically investigate the robustness of the 3-level hierarchical observer of the FTMS presented in Chapter 4 to

- failures in the global observer at the top-level of the hierarchy,
- failures in the physical sensors used by the local observers at the lowest level of the hierarchy,
- initialization errors at all levels of the hierarchy, and
- tuning parameters at all levels of the hierarchy.

It has been demonstrated that, as a result of the inherent redundancy in the hierarchical network, the degradation in the performance of the overall observer is gradual in the case of a failure in the global observer at the top level of the hierarchy. Additionally, it has been shown that failures of the physical sensors used at the lowest level of the hierarchy can have a larger impact on the overall estimation accuracy of the hierarchical observer than the failure of the global observer at the top level. Also, for the case studies conducted in this chapter, it was found that the

hierarchical and the centralized observers are equally robust to faulty physical sensors. Furthermore, it has been demonstrated that, even in the presence of initialization errors at all levels of the hierarchy, the hierarchical observer can converge to the actual state values. However, as expected, the rate of the convergence decreases as the level of the hierarchy increases. This behavior is directly related to the update rates of the observers at different levels of the hierarchy (i.e. the update rates of the observers decrease as the level of the hierarchy increases). Finally, after testing several tuning parameter sets, the overall estimation accuracy of the hierarchical observer was found to be reduced when the models are trusted more than the pseudo-measurements at the upper levels of the hierarchy. This can be related to the fidelity of the models used by the upper-level observers. The results presented in this chapter are specific for a particular system. However, several of these outcomes can be generalizable for other systems with different architectures.

Chapter 6
Model-based Fault Diagnosis for Complex Dynamical Systems

6.1 Motivation and Background

Fault detection and isolation (FDI) has become an important and challenging topic in many engineering fields such as aerospace engineering [26], [94]–[102], chemical engineering [103]–[105], nuclear engineering [106], [107], and power electronics [108]. Early fault diagnosis not only improves system reliability but can also help prevent complete system failure in the case of safety-critical systems. A fault is defined to be any malfunction in the system dynamics that causes an anomaly in the system performance [25], [30], [109]. A fault can occur in the actuators, sensors, or even in the system components. A fault diagnosis approach can be used to ensure that the system is operating normally and safely. Fault diagnosis can be divided into two tasks: fault detection and fault isolation. The fault detection task determines whether a fault has occurred in the system. The fault isolation task determines in which sensor, actuator, or component the fault has occurred.

FDI techniques are usually based on analytical or hardware redundancies [25], [109]. In the case of hardware redundancy, multiple components are used to compare duplicate measurements of the same signal [26], [27]. The major problems of this approach are the increased cost and weight of the system due to the additional components needed. As a result, hardware redundancy might not be a good fit for systems such as small unmanned aircraft where there are hard constraints on the size, weight, and power of the system [110]. These problems

can be solved using an analytical redundancy approach in which a mathematical model of the system is used instead of the extra hardware [28]–[30].

Observer-based FDI methods are one of the most well-known techniques based on analytical redundancy. The basic concept of observer-based FDI techniques is to compare the actual system behavior to the estimated system behavior obtained from an observer [30]–[32]. The residual generated from the difference between the actual response and the estimated response of the system is used to detect and isolate faults. Typically, residuals are zero in fault-free case, and an increase in their values above zero indicates that a fault has occurred in the system. However, since perfect models do not exist in practice, there will always be a discrepancy between the actual system's measurements and the estimated measurements obtained from the observers even when there is no fault in the system. This discrepancy causes false alarms and interferes with the performance of the FDI approach. Hence, to avoid false alarms, residuals should be designed to be insensitive to modeling uncertainties and noise. On the other hand, reduction in the sensitivity of the residuals to modeling errors should not reduce its sensitivity to actual faults in the systems. Robustness is particularly important for the detection of incipient faults (i.e. drift change) since their effect on the residual is minor compared to the effect of abrupt faults (i.e. step change).

Unknown input observers can be used to generate robust residuals by de-coupling the unknown inputs, i.e. disturbances, from the residuals [36]. Once a fault is detected, it can be isolated using a set of structured residuals obtained from a bank of UIOs. Structured residuals are designed to be sensitive to certain faults and insensitive to others. UIO-based FDI has been widely applied in the literature owing to its robustness property [36], [105], [111]–[113]. However, most of the work in the literature considered low order models for the design of UIOs due to the additional complexity introduced with the design of online estimators for high dimensional models. This work develops and experimentally validates an overall fault detection and isolation approach for complex (i.e. high dimensional) dynamical systems using graph-based models, a structure preserving aggregation-based model order reduction technique, and a bank of UIOs.

The remainder of the chapter is organized as follows. Section 6.2 presents the observer-based fault diagnosis algorithm used in this work. The models used by the FDI algorithm are

presented in section 6.3. An example aircraft fluid-based thermal management system used to experimentally validate the fault diagnosis framework is presented in section 6.4. Experimental validation of the FDI implementation is presented in section 6.5. Conclusions are presented in section 6.6.

6.2 Observer-based Fault Diagnosis

Physical systems are usually excited by unknown exogenous signals (i.e. unknown disturbances). In the FDI community, these signals are referred to as "unknown inputs". Therefore, when unknown disturbances are present in a system, some of the inputs are unknown. Consequently, a conventional observer that uses all input signals of a system cannot be designed. In this case, a UIO, which is a generalization of the Luenberger observer, can be used. More specifically, a UIO is an observer in which the state estimation error approaches zero asymptotically regardless of the presence of the unknown input, i.e. disturbance, in the system [114]. Many methods have been proposed for the design of full-order [114]–[116] and reduced-order [117], [118] UIOs. However, the higher number of free parameters in the full-order UIO creates more design freedom that can be used to achieve other design criteria such as the rate of convergence. The focus of this chapter is on the design of a robust FDI framework based on full-order UIOs.

To design a UIO, system uncertainties are represented by additive disturbances as follows.

$$\begin{cases} \dot{x}(t) = Ax(t) + Bu(t) + Ed(t) \\ y(t) = Cx(t), \end{cases} \tag{6.1}$$

where $x(t) \in \mathbb{R}^n$ represents the state vector, $u(t) \in \mathbb{R}^r$ represents the known input vector, $d(t) \in \mathbb{R}^q$ represents the disturbance vector (i.e. unknown input), and $y(t) \in \mathbb{R}^m$ represents the output vector. A, B, C, and D are known matrices with appropriate dimensions. The dynamics of a full-order UIO are given by [114]

$$\begin{cases} \dot{z}(t) = Fz(t) + TBu(t) + Ky(t), \\ \hat{x}(t) = z(t) + Hy(t), \end{cases} \tag{6.2}$$

where $z(t) \in \mathbb{R}^n$ represents the observer state vector, $\hat{x}(t) \in \mathbb{R}^n$ represents the estimated state vector, and F, T, K, and H represent matrices that should be designed to achieve disturbance decoupling. The dynamics of the state estimation error $e(t) = x(t) - \hat{x}(t)$ are then given by

$$\dot{e}(t) = \dot{x}(t) - \dot{\hat{x}}(t) \tag{6.3}$$

$$\begin{aligned} \dot{e}(t) = {} & (A - HCA - K_1C)e(t) + [F - (A - HCA - K_1C)]z(t) \\ & + [K_2 - (A - HCA - K_1C)H]y(t) + [T - (I - HC)]Bu(t) \\ & + (HC - I)Ed(t), \end{aligned} \tag{6.4}$$

where

$$K = K_1 + K_2. \tag{6.5}$$

The primary requirement for the design of a UIO is the a priori knowledge of the matrix E. Thus, if F, T, K, and H are designed such that

$$\begin{cases} (HC - I)E = 0, \\ T = I - HC, \\ F = A - HCA - K_1C, \\ K_2 = FH, \end{cases} \tag{6.6}$$

the state estimation error will be given by

$$\dot{e}(t) = Fe(t). \tag{6.7}$$

Further, if F is Hurwitz, then $e(t)$ approaches zero asymptotically. Therefore, if K_1 is chosen such that F is Hurwitz, the observer will be a UIO since $\hat{x}(t) \to x(t)$ in the presence of unknown inputs. The necessary and sufficient conditions for the existence of a UIO are [114]:

1. rank(CE) = rank(E)
2. (C, A_1) is detectable, and $A_1 = A - E[(CE)^T CE]^{-1}CA$.

A fault can occur in a number of different locations in a system (e.g. sensors, actuators, components, etc.). However, the focus in this chapter is on actuator faults only. That is, sensors

and components are assumed to be fault-free. Fault diagnosis is achieved by generating residuals and detecting their threshold crossings. Residuals are generated from the difference between the actual system output and the observer output and are given by

$$r(t) = y(t) - C\hat{x}(t) = (I - CH)y(t) - Cz(t). \tag{6.8}$$

Faults can be then detected using the following logic

$$\begin{cases} \|r(t)\| \le \text{Threshold, Fault-free case} \\ \|r(t)\| > \text{Threshold, Faulty case} \end{cases} \tag{6.9}$$

and thresholds can be designed to be constant, time-varying, or state-dependent. Once a fault is detected, it can be isolated using a bank of r UIOs. Each UIO in the bank is given by

$$\begin{cases} \dot{z}^i(t) = F^i z^i(t) + T^i B^i u^i(t) + K^i y(t) \\ r^i(t) = (I - CH^i)y(t) - Cz^i(t), \quad for\ i = 1, 2, ..., r, \end{cases} \tag{6.10}$$

where $B^i \in \mathbb{R}^{n\times(r-1)}$ is obtained from B by deleting the i^{th} column b_i, and $u^i \in \mathbb{R}^{r-1}$ is obtained from u by deleting the i^{th} component u_i. The matrices F^i, T^i, K^i, and H^i are given by

$$\begin{cases} H^i C E^i = E^i \\ T^i = I - H^i C \\ F^i = T^i A - K_1^i C \\ K_2^i = F^i H^i \\ K^i = K_1^i + K_2^i \end{cases} \tag{6.11}$$

where

$$E^i = \begin{bmatrix} E & b_i \end{bmatrix}. \tag{6.12}$$

To isolate a fault in the i^{th} actuator, the following logic is used

$$\begin{cases} \left\| r^i(t) \right\| < R^i, \quad for\ i = 1,...,r \\ \left\| r^i(t) \right\| \geq R^k, \quad for\ k = 1,...,i-1,i+1,...,r \end{cases} \tag{6.13}$$

where R^i and R^k represent isolation thresholds.

The unknown disturbances modeled in equation (6.1) can represent modeling errors, linearization errors, parameter variations, or model order reduction errors. For example, a mathematical model can be represented by

$$\begin{bmatrix} \dot{x}_r(t) \\ \dot{x}_h(t) \end{bmatrix} = \begin{bmatrix} A_{11} & A_{12} \\ A_{21} & A_{22} \end{bmatrix} \begin{bmatrix} x_r(t) \\ x_h(t) \end{bmatrix} + \begin{bmatrix} B_1 \\ B_2 \end{bmatrix} u(t), \tag{6.14}$$

where x_r represents the state vector of the reduced-order model and x_h represents the vector of the remaining states of the full-order model (i.e. higher order states). Consequently, the reduced-order model can be represented as

$$\dot{x}_r(t) = A_r x_r(t) + B_r u(t) + Ed(t), \tag{6.15}$$

where

$$Ed(t) = \begin{bmatrix} (A_{11} - A_r) & A_{12} & (B_1 - B_r) \end{bmatrix} \begin{bmatrix} x_r(t) \\ x_h(t) \\ u(t) \end{bmatrix}. \tag{6.16}$$

That is, equations (6.15) and (6.16) show that model order reduction errors can be represented by additive disturbances and consequently, they can be decoupled from the residuals. However, the additive disturbance modeled in equation (6.1) do not capture sensor noise. In practice, sensor noise exists and actual system output (i.e. sensor measurement) can be represented by

$$y(t) = Cx(t) + \nu(t), \tag{6.17}$$

where for example $\nu(t) \sim N(0, R_k)$ is a white noise vector with zero mean and covariance R_k. Therefore, to avoid false alarms caused by sensor noise, thresholds should be chosen to be larger than the effect of sensor noise on the residuals. Substituting (6.17) into (6.10), threshold lower limits can be chosen such that

$$R^i > \left\| (I - CH^i)v(t) \right\|_2 . \tag{6.18}$$

Equation (6.10) shows that each residual is a function of all outputs (i.e. $y(t)$) and all but one input (i.e. $u^i(t)$). This framework is known as the generalized observer framework and can be used to detect and isolate one fault at a time. It is found that, for this class of applications, this framework offers more design freedom for disturbance decoupling than the dedicated observer framework in which multiple faults can be detected at the same time [114].

Compared to conventional observers (e.g. Luenberger observers or Kalman filters), the major benefit of UIOs is the robustness achieved through disturbance decoupling. Specifically, a Luenberger observer for (6.1) is given by

$$\begin{cases} \dot{\hat{x}}(t) = A\hat{x}(t) + Bu(t) + L(y(t) - C\hat{x}(t)), \\ \hat{y}(t) = C\hat{x}(t), \end{cases} \tag{6.19}$$

where L represents the gain matrix and $\hat{y}(t)$ represents the output of the observer. The dynamics of the state estimation error $e(t) = x(t) - \hat{x}(t)$ are then given by

$$\dot{e}(t) = (A - LC)e(t) + Ed(t). \tag{6.20}$$

Equation (6.20) demonstrates that, for a Luenberger observer, the state estimation error is affected by unknown signals disturbing the physical system. Consequently, using this type of observers to perform FDI complicates the process of threshold selection and affects the robustness of the residuals.

6.3 Physics-based Lumped Parameter models for Fault Diagnosis

6.3.1 Physics-based Lumped Parameter Models

The models used by the UIOs are required to run in real-time, demanding a suitable balance between accuracy and computational complexity. Consequently, these models are developed using the lumped parameter physics-based modeling technique presented in Chapter 2. That is, the dynamics of the monitored systems are captured by graph-based models. As presented in section 2.2 (i.e. equation (2.7)), the dynamics of graph-based models are typically

represented by a set of first order nonlinear differential equations. Therefore, prior to the design of the UIOs, the dynamics of the graph-based model of the monitored system should be linearized.

A linear representation of the graph dynamics can be obtained by individually linearizing the power flows along each edge of the graph. Chapter 3 showed that the dynamics of a graph can be directly represented by a linear time-varying system when the power flows along the edges satisfy a state-affine form. Furthermore, it has been demonstrated that thermal power flows of fluid-based thermal management systems (FTMS) of electrified vehicles (i.e. convective and advective power flows) are state-affine. Thus, thermal dynamics of a FTMS can be directly represented by a linear time-varying system. When, power flows along the edges of a graph can not be modeled by a state-affine form, a linear representation of the graph-dynamics can be obtained by linearizing each power flow individually using a first order Taylor series as done in [23].

6.3.2 Reduced-Order Models

High dimensional models present a challenge for online estimation. Therefore, it is often desirable to design observers using reduced-order models. In this chapter, complexity of graph-based models is reduced by applying an aggregation-based model order reduction technique. There are many methods available in the field of model order reduction. The best known methods are Truncated Balanced Realization [28], Hankel-norm reduction [120], and Proper Orthogonal Decomposition [121]. However, these methods do not preserve the physical correspondence between the physical system and the reduced-order model. The model order reduction technique used in this work reduces the number of nodes of the model while preserving its input-output behavior and the correspondence with the physical system. This technique is an aggregation based approach developed in [122]. It provides a way to aggregate multiple adjacent nodes in the full-order model into single nodes, called “super-nodes”, in the reduced-order model by applying the aggregation method of a continuous time Markov chain. The main idea behind this model order reduction technique is to find an optimal partition function $\phi : V \to M$, where $M = \{1, 2, ..., m\}$ with $m < n$. The partition ϕ reduces the dimension of the state space from n nodes in the full-order model into m nodes in the reduced-order

model, where m is specified by the user. Each super-node has a super-capacitance $\overline{C}$ and a super-state $\overline{x}$. Super-nodes are connected by edges representing super-power flows $\overline{P}$. Super-capacitances and super-power flows are given by

$$\overline{C}_k = \sum_{i \in V} C_i, \tag{6.21}$$

$$\overline{P}_{kl} = \sum_{i,j \in E} \overline{P}_{ij}. \tag{6.22}$$

In order to aggregate the nodes of the full-order model, the optimal partition function ϕ has to be found. This function is difficult to get exactly when the order of the reduced-order model is greater than 2 which is the general case. Instead, the reduced-order model is obtained by applying a spectral algorithm on the symmetric matrix $\breve{P} = 0.5(\Delta^{\frac{1}{2}} P \Delta^{-\frac{1}{2}} + \Delta^{-\frac{1}{2}} P^T \Delta^{\frac{1}{2}})$. Here $\Delta = diag(\pi)$, where π is the stationary distribution of the Markov chain, and $P(t)$ is the Markov transition matrix. For the linear systems of interest, $P(t)$ is given by $P(t) := e^{At}$ [123]. The stationary distribution is given in terms of the capacitances by

$$\pi_i = \frac{C_i}{\sum_{j \in V} C_j}, i \in V. \tag{6.23}$$

The computation steps used to develop reduced-order models are shown in Algorithm 5.1.

Algorithm 5.1: Computation Steps of The Model Order Reduction Algorithm

1. Construct $\breve{P}$: $\breve{P} = 0.5(\Delta^{\frac{1}{2}} P \Delta^{-\frac{1}{2}} + \Delta^{-\frac{1}{2}} P^T \Delta^{\frac{1}{2}})$.
2. Check the sign structure of the second largest eigenvector of $\breve{P}$.
3. Aggregate the spatially adjacent nodes that share the same sign into super-nodes.
4. Calculate the super-capacitances and super-power flows (Neglect the internal power flows in the super-nodes).

6.4 An Example Aircraft Fluid-based Thermal Management System

In this section, the robust UIO-based actuator FDI approach is implemented on the example aircraft fluid-based thermal management system shown in Figure 6.1. The system schematic is shown in Figure 6.2. In this system, the fluid plays the role of a heat sink and a coolant [124]. Heat generated from the generator, AEE, and electronics represented by the cold plates shown in Figure 6.1 gets absorbed by the fluid, and then rejected to neighboring systems through heat exchangers. The system is composed of 4 loops: 3 secondary loops (referred to by yellow, purple, and green arrows) and one main loop (referred to by red arrows).

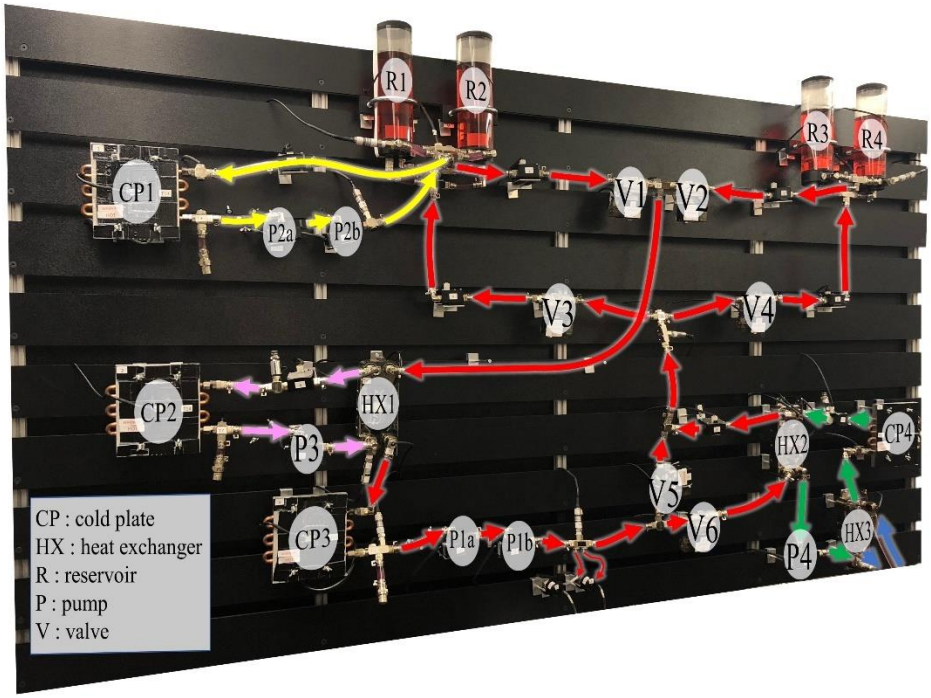

Figure 6.1 Testbed representing an example aircraft fluid thermal management system.

Heat generated by cold plate CP1 (in the secondary loop referred to by yellow arrows) gets absorbed by the fluid driven by pumps P2a and P2b and transferred to the reservoirs R1 and R2. Heat generated by cold plate CP2 (in the secondary loop referred to by purple arrows) gets absorbed by the fluid driven by pump P3 and transferred to the main loop through the fluid-to-fluid heat exchanger HX1. The secondary loop referred to by green arrows absorbs the heat generated in the main loop through the fluid driven by pump P4 and transfers it to a heat sink representing a neighboring system or the external environment. The blue arrows shown in Figure

6.2 represent input and output flows of a chiller representing a heat sink. Cold plate CP4 helps controlling the temperature of the fluid in the loop. For example, this cold plate helps setting specific temperatures for the external environment or the neighboring system represented by this secondary loop. The main loop fluid driven by pumps P1a and P1b absorbs the heat generated by cold plates CP1, CP2, and CP3 and transfers it to the heat sink loop.

Each component, actuator, or sensor of the testbed can fail in several ways leading to the failure of the overall system. The scope of this case study is limited to the detection and isolation of pump faults characterized by an increase in the pump commands above nominal pump command values determined a priori by a mission profile. Only major faults that occur in pumps are considered. Fluid leaks which would be more like incipient faults are not considered. A pump error can negatively impact both the hydraulic and the thermal behaviors of the system given the coupling between the two energy domains. However, in this example case study, fault detection and isolation are achieved by designing UIOs that estimate dynamics spanning the hydraulic domain only. More specifically, the inputs of the UIOs designed in this case study are the pump commands and the residuals are generated from the differences between the actual and estimated pressure drops across the corresponding fluid loops.

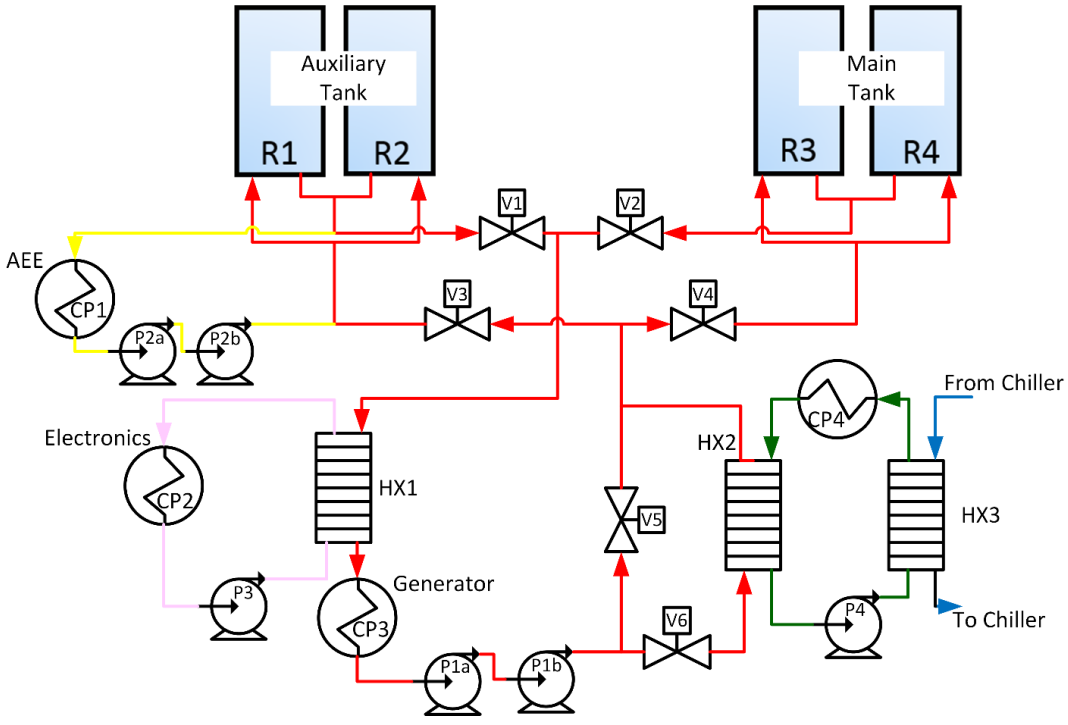

Figure 6.2 Schematic of the testbed shown in Figure 6.1.

As presented in section 6.2, fault isolation is achived by designing a bank of UIOs. The number of UIOs in the bank should be equal to the number of monitored actuators. Each residual is then designed to be sensitive to all but one fault. In this case study, the bank of UIOs is designed to isolate faults in pumps P1a, P1b, P2a, and P2b only since, from a hydraulic perspective, the remaining two loops (denoted by purple and green arrows) are disconnected from the main loop. Furthermore, pumps P1a and P1b are connected in series (i.e. driven by the same input) and are jointly referred to by P1. Similarly, pumps P2a and P2b are connected in series and are jointly referred to by P2. Therefore, it is not necessary to isolate faults between pumps P1a and P1b, or P2a and P2b. Consequently, the robust FDI approach is used to isolate P1 faults from P2 faults.

6.5 Experimental Validation of the FDI Framework

Figure 6.3 shows the full-order graph-based model of the mass flow dynamics of the 2 loops containing P1 and P2. As presented in Chapter 2, the hydraulic dynamics of a fluid thermal management system (FTMS) derived from a graph-based model are represented by a nonlinear form. Therefore, in order to design the UIOs, a linear dynamic model is obtained by linearizing each mass flow rate individually. From Chapter 2 (i.e. equations (2.11) and (2.13)), the nonlinear mass flow rates for all components of the FTMS can be described by the following general form [23]

$$\dot{m}_j = c_{1,j}\sqrt{c_{2,j} + c_{3,j}(p_j^{tail} - p_j^{head}) + c_{4,j}u_j}, \tag{6.24}$$

where the coefficient $c_{i,j}$ are constant for each i, and j, p_j^{tail}, and p_j^{head} are the pressure states associated with the head and tail vertices, and u_j is the actual pump effort given by

$$u_j(s) = \frac{e^{-\lambda_j s}}{\tau_j s + 1} u_j^c(s), \tag{6.25}$$

where u_j^c is the pump command value expressed in terms of % duty cycle of PWM, τ_j is the time constant, and λ_j is the time delay. By linearizing equation (6.24) around equilibrium

operating conditions using a first-order Taylor series, linear mass flow rates can be represented by

$$\Delta \dot{m}_j = a_j(\Delta p_j^{tail} - \Delta p_j^{head}) + b_j \Delta u_j, \tag{6.26}$$

where a_j and b_j are constant coefficients, and Δ represents deviations from the linearization point. By substituting the linearized mass flow rates in Equation (6.26) into (refer to Chapter 2 for a detailed derivation of equation (6.27))

$$C\dot{p} = -\overline{M}\dot{m}, \tag{6.27}$$

the linear state space model used by the UIOs can be given by

$$\begin{aligned} \dot{p} &= A\Delta p + B\Delta u \\ \Delta \dot{m} &= C\Delta p + D\Delta u \end{aligned} \tag{6.28}$$

where

$$A = -(C)^{-1}\overline{M}\,diag([a_j])(\overline{M})^T, \tag{6.29}$$

$$B = -(C)^{-1}\overline{\overline{M}}\,\hat{b} \tag{6.30}$$

$$C = diag([a_i])(\overline{M})^T, \tag{6.31}$$

$$D = [d_{jk}] \in \mathbb{R}^{N_e \times N_p}. \tag{6.32}$$

$\overline{\overline{M}}$ represents the columns of the submatrix $\overline{M}$ corresponding to edges associated with pumps, and $\hat{b}$ represents the vector of input coefficients for edges associated with pumps. d_{jk} is given by

$$d_{jk} = \begin{cases} b_j, & \text{if edge } j \text{ is associated with pump } k, \\ 0, & \text{else.} \end{cases} \tag{6.33}$$

Figure 6.4 shows pumps P1 and P2 commands given in terms of %PWM. The reduced-order graph-based model is shown in Figure 6.5. Each node of the reduced-order model represents a lumped state of pressure obtained by aggregating several adjacent nodes of the full-

order model. Figure 6.6 shows simulation versus experimental results of the pressure dynamics of the nonlinear full-order, linearized full-order, and linearized reduced-order graph-based models of 2 components of the FTMS (i.e. Tank 3, and Pump 2b).

According to the FDI framework presented in section 6.2, a fault in one of the pumps results in an increase in the values of all but one residual. Since the FDI framework is used to isolate faults between two pumps (i.e. P1 and P2), a bank of 2 UIOs is used. The matrices of the state space model and the observers' parameters are shown in the Appendix. UIO1 generates residual 1 (R^1) and UIO2 generates residual 2 (R^2). Consequently, a fault in P1 results in an increase in R^2, and a fault in P2 results in an increase in R^1.

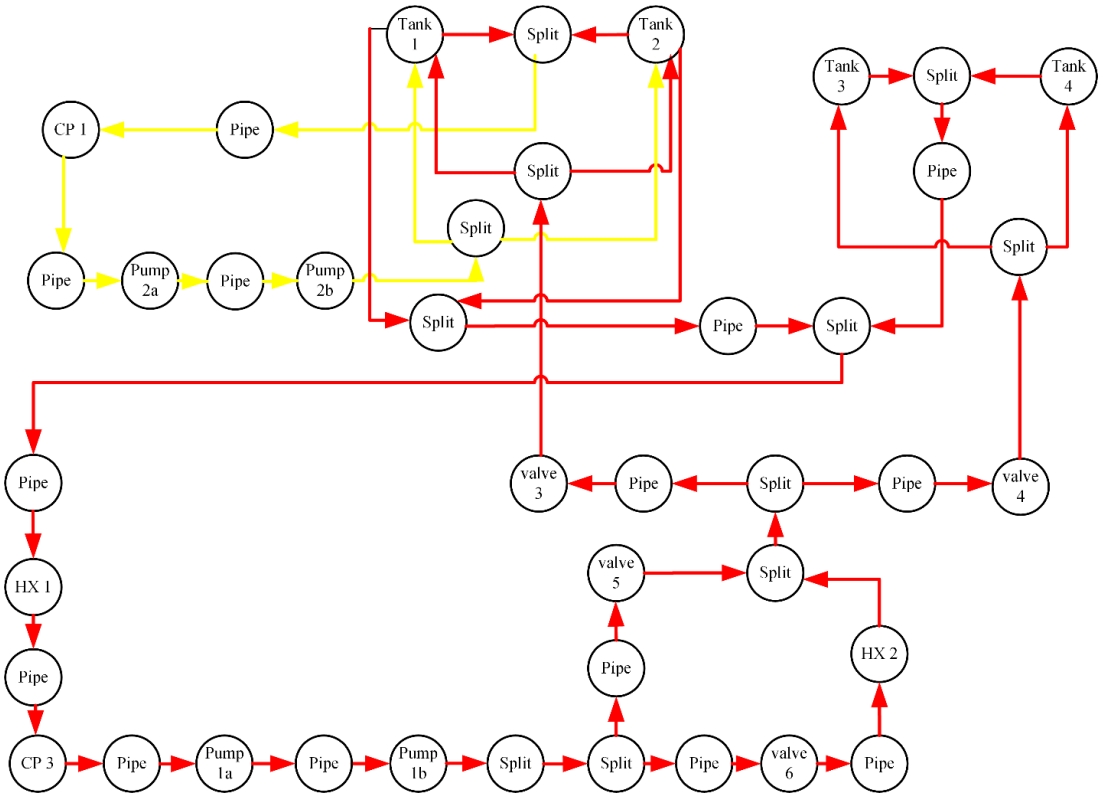

Figure 6.3 Full-order graph-based model of the mass flow dynamics of the FTMS.

The performance of the FDI approach is tested in 3 different scenarios. In the first scenario, P1 and P2 operate at their nominal commands (i.e. no fault in the system). Simulation and experimental results presented in Figure 6.7 show that, in a fault-free scenario, there is no increase in the values of residuals R^1 and R^2 above their threshold. In the second scenario, a

fault is introduced in P1 as shown in Figure 6.8. In this scenario, R^2 crosses the threshold until the fault is cleared and then remains below the threshold until the end of the mission. On the other hand, R^1 remains below the threshold during the entire mission. In the third scenario, a fault introduced in P2 as shown in Figure 6.9 results in an increase in R^1 above the threshold until the fault is cleared, whereas R^2 remains below the threshold during the entire mission. Figure 6.8 and Figure 6.9 present results from 3 experiments. Through disturbance decoupling achieved by equations (6.6) and (6.7), a constant threshold value of $R^1 = R^2 = 0.2$ is found to be large enough to avoid false alarms and sensitive enough to detect a 25% change in actuator input commands. Threshold lower bound was found using equation (6.15) based on pressure sensor noise properties and matrices $(A3)$, $(A4)$, and $(A5)$ from the Appendix. In all experiments, pressure is measured using Measurement Specialities US300 sensors with a +/-0.1% accuracy. It is important to note that increasing threshold values decreases the UIO sensitivity to actual actuator faults. Furthermore, using sensors with higher accuracy helps decreasing threshold lower bounds and consequently increasing UIO sensitivity. Figures 6.7-6.9 indicate that the constant residuals chosen did not result in any false alarms or missed detections.

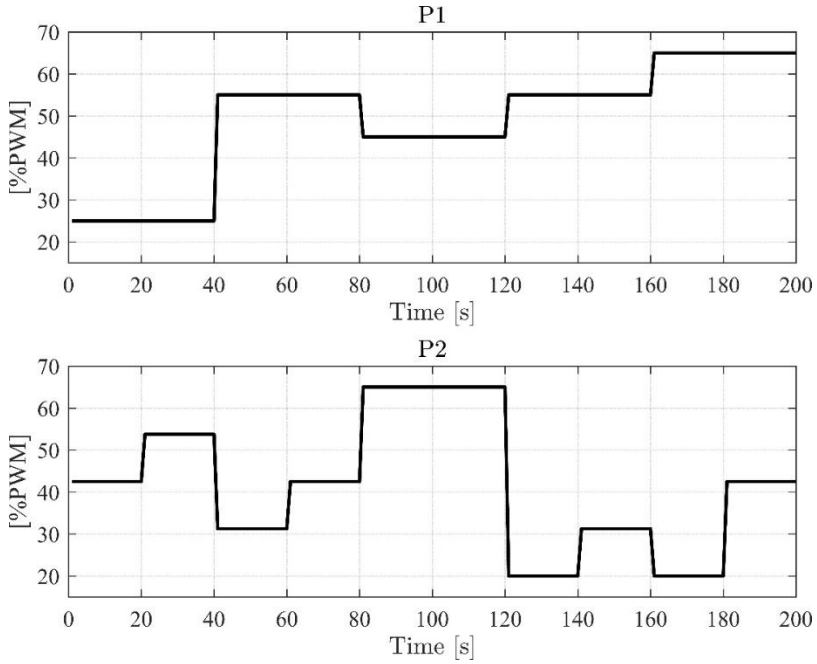

Figure 6.4 Pump commands given in terms of PWM.

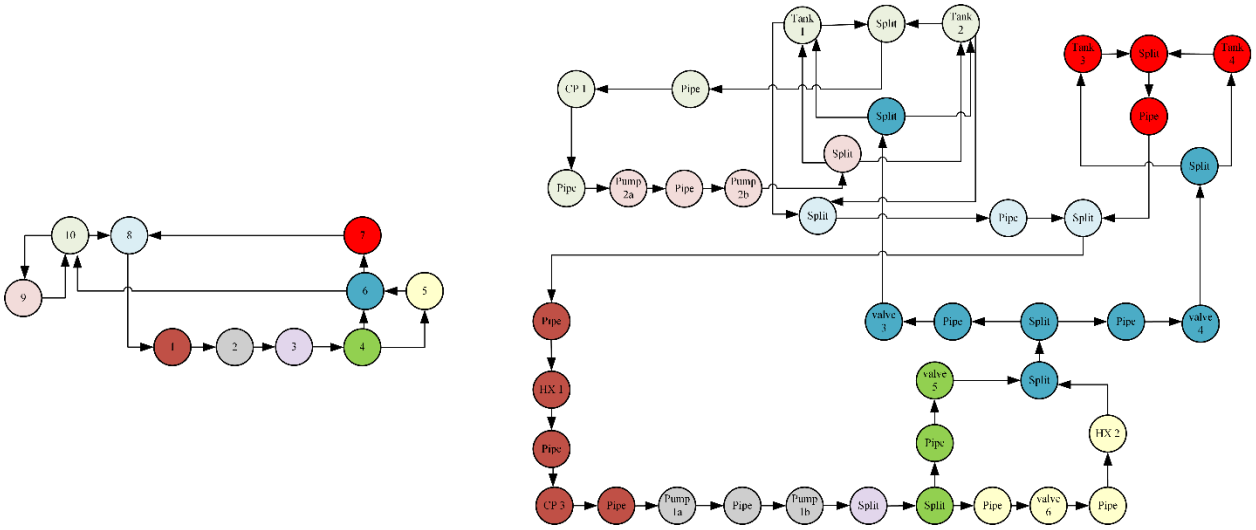

Figure 6.5 Reduced order (left) versus full-order (right) graph-based model of the mass flow dynamics of the FTMS.

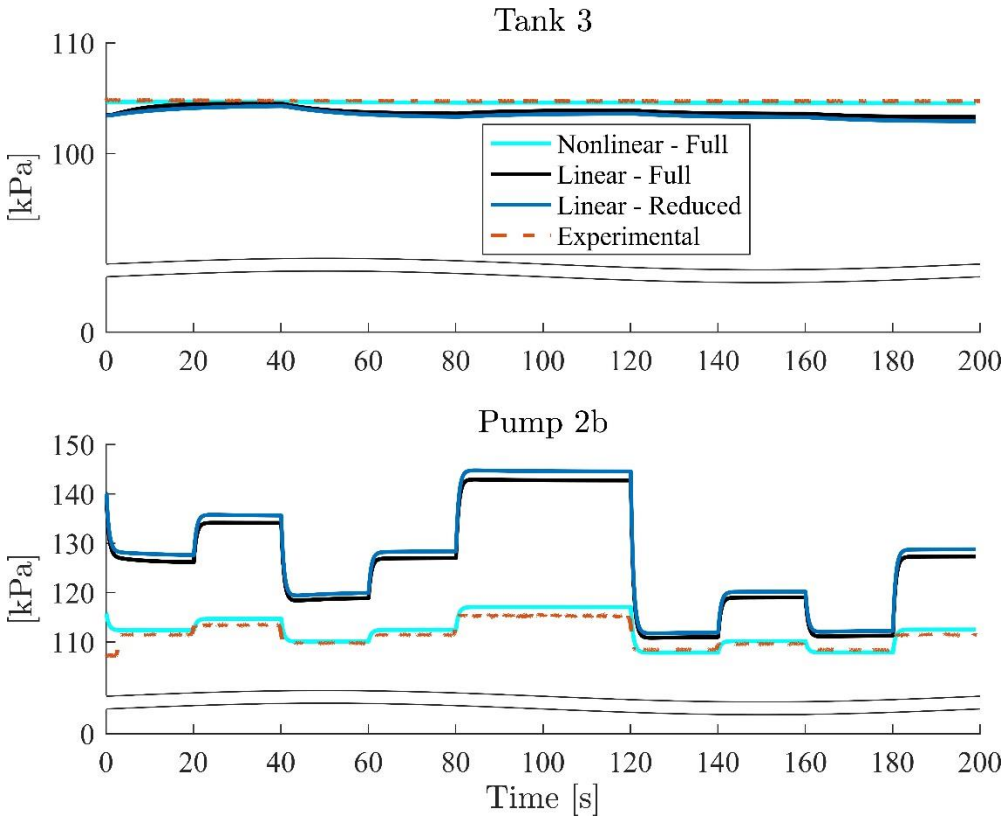

Figure 6.6 Pressure dynamics of the FTMS.

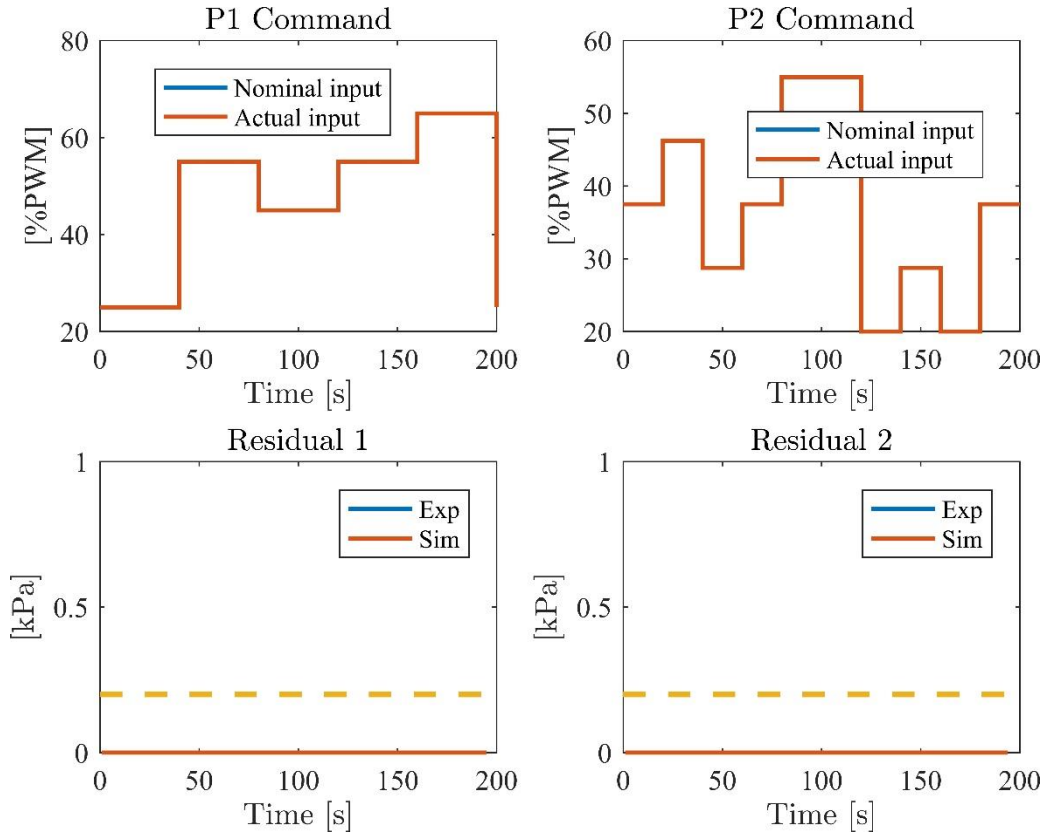

Figure 6.7 FDI – Scenario 1 (Non-faulty case).

6.6 Conclusions

In the case of safety critical systems (e.g. aircraft systems), early fault diagnosis not only improves system reliability, but can also help prevent complete system failure. This chapter presents a robust fault detection and isolation (FDI) framework for complex dynamical systems. For fault diagnosis, robustness is central for avoiding false alarms without reducing sensitivity to actual faults in the system. In this chapter, robustness is achieved by decoupling the effect of unknown inputs modeled as additive disturbances (i.e. modeling errors, linearization errors, parameter variations, or model order reduction errors) from a set of structured residuals generated from a bank of UIOs. The framework is experimentally validated on an example aircraft fluid thermal management system (FTMS). System dynamics are modeled using the graph-based approach presented in Chapter 2. To reduce the complexity of the dynamic models used by the observers, a structure-preserving aggregation-based model order reduction technique

is used. A reduced-order linearized state space model is then used in a bank of UIOs to generate a set of structured robust (in the sense of disturbance decoupling) residuals. Simulation and experimental results show successful actuator FDI in the presence of unknown inputs.

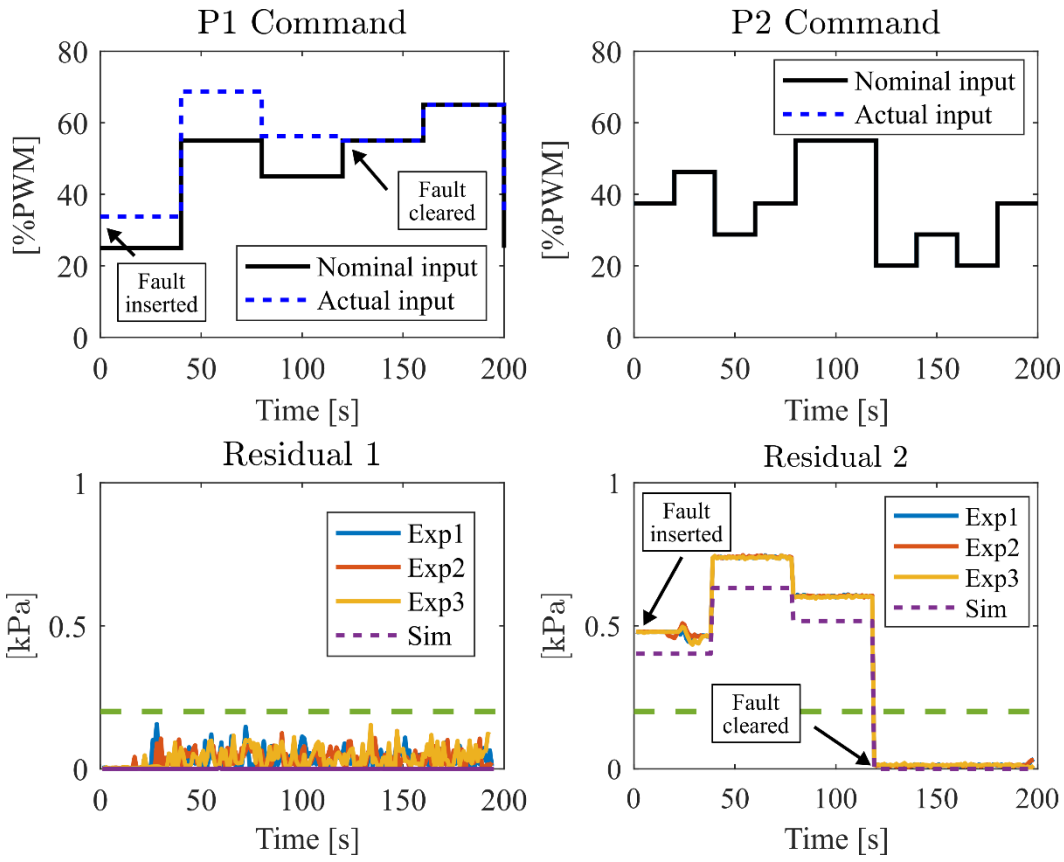

Figure 6.8 FDI – Scenario 2 (faulty case).

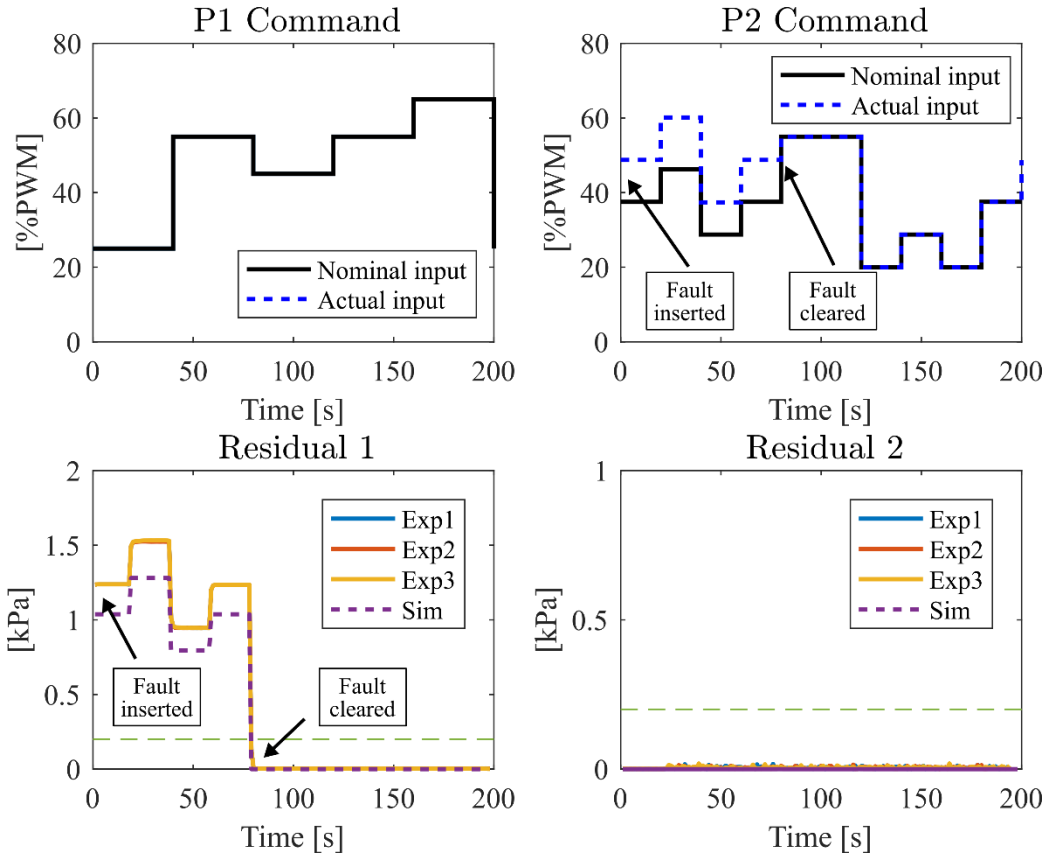

Figure 6.9 FDI – Scenario 3 (faulty case).

Chapter 7
Conclusion

7.1 Summary of Research Contributions

Electrified vehicles consist of many subsystems that interact among each other across multiple energy domains and dynamic timescales. To ensure their safe, reliable, and efficient performance, a holistic system perspective with novel estimation strategies that can account for coupling between subsystems and energy domains and identify anomalies in the system performance is needed. This dissertation proposes a hierarchical estimation approach with a novel coordination framework and an overall fault diagnosis approach for electrified vehicle systems.

Chapter 2 presents a modular and scalable graph-based modeling approach that can capture dynamics spanning multiple energy domains and timescales. The resulting models are control-oriented physics-based lumped parameter models that can run in real-time. Additionally, various system decomposition techniques that can generate hierarchical graph-based models are presented in this chapter. Finally, to reduce the computational complexity of the hierarchical models used by the hierarchical observers, Chapter 2 presents an aggregation-based model order reduction technique that preserves the physical correspondence between the physical systems and their reduced-order models.

Chapter 3 presents the architecture, formulation, and stability analysis of the proposed mutli-level hierarchical estimation framework. The formulation of a baseline centralized observer used as a benchmark for the hierarchical observer is also presented in this chapter. Furthermore, the advantages of the proposed hierarchical estimation approach compared to

conventional and current practices are discussed. This chapter ends with two simulation case studies that show the boundedness and convergence of the hierarchical estimation approach. It is found that, even though the sufficient conditions for the stability and convergence of the proposed hierarchical observer are derived in a conservative approach, the error bounds calculated in the case study are effective enough for successful control.

Chapter 4 presents and experimentally validates a 3-level hierarchical observer for thermal management systems of electrified vehicles. The testbed used for validation is designed to replicate the power flows of a fuel thermal management system of an electrified aircraft but does not represent any specific platform. The hierarchical observer is connected to a previously developed 3-level hierarchical controller with the objective of increasing the safety, capability, and efficiency of the thermal management system. Experimental results demonstrate that the hierarchical observer achieves good estimation accuracy that enables successful control of multi-timescale dynamical systems. Additionally, this chapter demonstrates that hierarchical estimation creates a tradeoff between centralized and decentralized estimation. Specifically, it is shown that the 3-level hierarchical observer is more accurate than a decentralized observer and less computationally expensive than a centralized observer.

Chapter 5 investigates the robustness of the hierarchical observer designed in Chapter 4 to failures at the top and lowest levels of the hierarchy, initialization errors, and tuning parameters. It is found that a fault at the lowest level of the hierarchy has a larger negative impact on the overall estimation accuracy of the proposed hierarchical observer than a fault at the top level. Additionally, it is demonstrated that the hierarchical observer can converge to the actual state values even in the presence of initialization errors. However, the convergence speed is directly related to the update rate of the observer, and thus lower-level observers converge faster than upper-level observers. Finally, it is found that designing upper-level observers to rely on their reduced-order models more than their pseudo-measurements reduces the overall estimation accuracy of the hierarchical observer.

Chapter 6 proposes and experimentally validates a robust fault diagnosis framework that detects and isolates faults in complex energy systems. Robustness is achieved by decoupling the effect of unknown inputs (i.e. modeling errors, linearizarion errors, model order reduction errors, parameter variations, noise, etc.) from a set of structured residuals used for fault diagnosis. Fault

isolation is then achieved using a bank of unknown input observers (UIOs). Experimental validation is performed on a testbed representative of an aircraft fluid-thermal management system without replicating any specific platform. The lumped parameter models used by the UIOs are derived using the graph-based modeling approach presented in Chapter 2. The complexity of the models is further reduced using a structure-preserving aggregation-based model order reduction technique. Experimental results demonstrate successful fault detection and isolation (i.e. no false alarms and missed detections).

7.2 Future Work

The contributions presented in this dissertation constitute an initial effort towards the development of safe, reliable, and efficient complex energy systems. Future research on this topic will build on this work to advance the theory and applications.

1. Hierarchical estimation of additional physical systems and energy domains: The hierarchical estimation framework proposed in this dissertation is adaptable to different systems, architectures, and energy domains. However, the dynamics of the testbed used for validation (i.e. the FTMS of an electrified aircraft presented in Chapter 4) spanned the hydraulic and thermal domains only. Electrical inefficiencies (i.e. from the battery, power electronics, electric machine, etc.) are simulated. Future work will expand the current testbed to include electrical and mechanical components and experimentally validate hierarchical observers and controllers that capture interactions between the mechanical, electrical, thermal, and hydraulic domains. Additionally, future work should experimentally validate the approach on a different platform (e.g. electrified automotive system [51]).
2. Sufficient conditions for the stability and convergence of multilevel hierarchical observers for nonlinear systems with switched dynamics: The stability analysis presented in Chapter 3 is based on the assumption that every observer in the hierarchy is a linear Kalman filter. However, many complex energy systems are better represented by nonlinear models. Additionally, it is very common for these systems to include discrete components with switching dynamics (e.g.

valves in a hydraulic system, switches in an electrical system, etc.). Future work should expand the analysis presented in Chapter 3 to include sufficient conditions for the stability and convergence of hierarchical frameworks that include nonlinear and switched observers.

3. Simultaneous fault detection and isolation of multiple faults for different component types: The fault diagnosis framework proposed and experimentally validated in Chapter 6 can isolate one actuator fault at a time. However, in practice there is a need to simultaneously detect and isolate faults in multiple components of different types (e.g. simultaneously detecting and isolating faults in 3 sensors, 2 actuators, and 1 pipe). Additionally, it is very important to communicate accurate estimates of the fault magnitudes and profiles to the controllers of the monitored systems so that appropriate corrective actions can be taken in real time. Future efforts should build on the tools presented in Chapter 6 to incorporate these capabilities in the robust fault diagnosis framework proposed in this dissertation.
4. Scalable observer-based fault diagnosis: Observer-based FDI suffers from a scalability problem. As described in Chapter 6, in these approaches, fault isolation is achieved through a bank of obsevers that run in parallel. Additionally, each observer in the bank is designed using the entire system model. Model order reduction can be an effective strategy to reduce the computational cost of this technique. However, for many large-scale complex energy systems, model order reduction might not be sufficient to design fast running models for the entire system with appropriate details for effective fault diagnosis. Consequently, to reduce computational cost, future work will investigate distributed observer-based fault diagnosis by integrating the fault diagnosis framework proposed in Chapter 6 into the hierarchical estimation framework proposed in Chapter 3. For example, each local observer at the lowest level of the hierarchy can be appended by a bank of observers designed to perform fault diagnosis for a specific subsystem only while receiving the required coupling information from upper-level observers in the hierarchy.

References

[1] V. Madonna, P. Giangrande, and M. Galea, “Electrical Power Generation in Aircraft: Review, Challenges, and Opportunities,” *IEEE Trans. Transp. Electrif.*, vol. 4, no. 3, pp. 646–659, 2018.

[2] B. Sarlioglu and C. T. Morris, “More Electric Aircraft: Review, Challenges, and Opportunities for Commercial Transport Aircraft,” *IEEE Trans. Transp. Electrif.*, vol. 1, no. 1, pp. 54–64, 2015.

[3] J. A. Rosero, J. A. Ortega, E. Aldabas, and L. Romeral, “Moving towards a more electric aircraft,” *IEEE Aerosp. Electron. Syst. Mag.*, vol. 22, no. 3, pp. 3–9, 2007.

[4] IEA, “Global EV Outlook 2019,” Paris, 2019.

[5] J. Hou, Z. Song, H. Park, H. Hofmann, and J. Sun, “Implementation and evaluation of real-time model predictive control for load fluctuations mitigation in all-electric ship propulsion systems,” *Appl. Energy*, vol. 230, no. August, pp. 62–77, 2018.

[6] J. N. Davidson, D. A. Stone, M. P. Foster, and D. T. Gladwin, “Real-Time Temperature Estimation in a Multiple Device Power Electronics System Subject to Dynamic Cooling,” *IEEE Trans. Power Electron.*, vol. 31, no. 4, pp. 2709–2719, 2016.

[7] W. Huang, S. Ghosh, S. Velusamy, K. Sankaranarayanan, K. Skadron, and M. R. Stan, “HotSpot: A compact thermal modeling methodology for early-stage VLSI design,” *IEEE Trans. Very Large Scale Integr. Syst.*, vol. 14, no. 5, pp. 501–513, 2006.

[8] M. Pedram and S. Nazarian, “Thermal Modeling, Analysis, and Management in VLSI Circuits: Principles and Methods,” *Proc. IEEE*, vol. 94, no. 8, pp. 1487–1501, 2006.

[9] A. K. Coskun, T. S. Rosing, and K. Whisnant, “Temperature aware task scheduling in MPSoCs,” in *Proceedings -Design, Automation and Test in Europe*, 2007.

[10] J. Doty *et al.*, “Dynamic Thermal management for aerospace technology: Review and outlook,” *J. Thermophys. Heat Transf.*, vol. 31, no. 1, pp. 86–98, 2017.

[11] D. B. Doman, “Fuel flow control for extending aircraft thermal endurance part I: Underlying principles,” *2016 AIAA Guid. Navig. Control Conf.*, no. January, 2016.

[12] D. B. Doman, “Fuel flow control for extending aircraft thermal endurance part II: Closed loop control,” *2016 AIAA Guid. Navig. Control Conf.*, no. 937, pp. 1–23, 2016.

[13] M. Bodie and M. Wolff, “Robust optimization of an aircraft power thermal management

system," *8th Annu. Int. Energy Convers. Eng. Conf.*, no. July 2010, 2010.

[14] T. Fischer, F. Götz, L. F. Berg, H.-P. Kollmeier, and F. Gauterin, "Model-based Development of a Holistic Thermal Management System for an Electric Car with a High Temperature Fuel Cell Range Extender," *Proc. 11th Int. Model. Conf. Versailles, Fr. Sept. 21-23, 2015*, vol. 118, pp. 127–133, 2015.

[15] Q. Wang, B. Jiang, B. Li, and Y. Yan, "A critical review of thermal management models and solutions of lithium-ion batteries for the development of pure electric vehicles," *Renew. Sustain. Energy Rev.*, vol. 64, pp. 106–128, 2016.

[16] S. Park and D. Jung, "Design of vehicle cooling system architecture for a heavy duty series-hybrid electric vehicle using numerical system simulations," *J. Eng. Gas Turbines Power*, vol. 132, no. 9, pp. 1–11, 2010.

[17] R. Fang, W. Jiang, J. Khan, and R. Dougal, "Thermal modeling and simulation of the chilled water system for future all electric ship," *2011 IEEE Electr. Sh. Technol. Symp. ESTS 2011*, pp. 265–271, 2011.

[18] J. S. Thongam, M. Tarbouchi, A. F. Okou, D. Bouchard, and R. Beguenane, "All-electric ships - A review of the present state of the art," *2013 8th Int. Conf. Exhib. Ecol. Veh. Renew. Energies, EVER 2013*, pp. 1–8, 2013.

[19] S. R. T. Peddada, D. R. Herber, H. C. Pangborn, A. G. Alleyne, and J. T. Allison, "Optimal flow control and single split architecture exploration for fluid-based thermal management," *J. Mech. Des. Trans. ASME*, vol. 141, no. 8, 2019.

[20] C. Bailey, "Thermal management technologies for electronic packaging: Current capabilities and future challenges for modelling tools," *10th Electron. Packag. Technol. Conf. EPTC 2008*, pp. 527–532, 2008.

[21] F. Kennel, D. Gorges, and S. Liu, "Energy management for smart grids with electric vehicles based on hierarchical MPC," *IEEE Trans. Ind. Informatics*, vol. 9, no. 3, pp. 1528–1537, 2013.

[22] M. R. Amini, H. Wang, X. Gong, D. Liao-McPherson, I. Kolmanovsky, and J. Sun, "Cabin and Battery Thermal Management of Connected and Automated HEVs for Improved Energy Efficiency Using Hierarchical Model Predictive Control," *IEEE Trans. Control Syst. Technol.*, vol. PP, pp. 1–16, 2019.

[23] H. C. Pangborn, J. P. Koeln, M. A. Williams, and A. G. Alleyne, "Experimental Validation of Graph-Based Hierarchical Control for Thermal Management," *J. Dyn. Syst. Meas. Control*, vol. 140, no. 10, p. 101016, 2018.

[24] Z. Gao, S. Member, C. Cecati, F. Ieee, and S. X. Ding, "A Survey of Fault Diagnosis and Fault - Tolerant Techniques Part I : Fault Diagnosis with Knowledge - Based and Signal-Based Approaches," *IEEE Trans. Ind. Electron.*, vol. 62, pp. 3757–3767, 2015.

[25] I. Hwang, S. Kim, Y. Kim, and C. E. Seah, "A survey of fault detection, isolation, and reconfiguration methods," *IEEE Trans. Control Syst. Technol.*, vol. 18, no. 3, pp. 636–653, 2010.

[26] P. Goupil, "AIRBUS state of the art and practices on FDI and FTC in flight control

system," *Control Eng. Pract.*, vol. 19, no. 6, pp. 524–539, 2011.

[27] D. S. Shim and C. K. Yang, "Optimal configuration of redundant inertial sensors for navigation and FDI performance," *Sensors*, vol. 10, no. 7, pp. 6497–6512, 2010.

[28] J. J. Gertler, "Analytical redundancy methods in fault detection and isolation- survey and synthesis," *Proc. IFAC/IAMCS Symp. safe Process*, vol. 1, no. December, pp. 9–21, 1991.

[29] E. Y. Chow and A. S. Willsky, "Analytical Redundancy and the Design of Robust Failure-Detection Systems," *IEEE Trans. Automat. Contr.*, vol. 29, no. 7, pp. 603–614, 1984.

[30] P. M. Frank, "Fault diagnosis in dynamic systems using analytical knowledge-based redundancy – A survey and some new results," *Automatica*, vol. 26, no. 3, pp. 459–474, 1990.

[31] R. J. Patton and J. Chen, "Observer-based fault detection and isolation: Robustness and applications," *Control Eng. Pract.*, vol. 5, no. 5, pp. 671–682, 1997.

[32] P. M. Frank and X. Ding, "Survey of robust residual generation and evaluation methods in observer-based fault detection systems," *J. Proc. Cont.*, no. 6, pp. 403–424, 1997.

[33] S. Mondal, G. Chakraborty, and K. Bhattacharyya, "Robust Unknown Input Observer for Nonlinear Systems and Its Application to Fault Detection and Isolation," *J. Dyn. Syst. Meas. Control*, vol. 130, no. 4, p. 044503, 2008.

[34] C.-S. Liu and H. Peng, "Inverse-Dynamics Based State and Disturbance Observers for Linear Time-Invariant Systems," *J. Dyn. Syst. Meas. Control*, vol. 124, no. 3, pp. 375–381, 2002.

[35] W. Chen and M. Saif, "Observer-Based Fault Diagnosis of Satellite Systems Subject to Time-Varying Thruster Faults," *J. Dyn. Syst. Meas. Control*, vol. 129, no. 3, p. 352, 2007.

[36] J. Chen, R. J. Patton, and H. Y. Zhang, "Design of unknown input observers and robust fault detection filters," *Int. J. Control*, vol. 63, no. 1, pp. 85–105, 1996.

[37] A. Teixeira, I. Shames, H. Sandberg, and K. H. Johansson, "Distributed fault detection and isolation resilient to network model uncertainties," *IEEE Trans. Cybern.*, vol. 44, no. 11, pp. 2024–2037, 2014.

[38] T. Van Cutsem and M. Ribbens-Pavella, "Critical Survey of Hierarchical Methods for State Estimation of Electric Power Systems," *IEEE Power Eng. Rev.*, vol. PER-3, no. 10, p. 37, 1983.

[39] R. Scattolini, "Architectures for distributed and hierarchical Model Predictive Control - A review," *J. Process Control*, vol. 19, no. 5, pp. 723–731, 2009.

[40] J. P. Koeln, M. A. Williams, H. C. Pangborn, and A. G. Alleyne, "Experimental Validation of Graph-Based Modeling For Thermal Fluid Power Flow Systems," in *Dynamic Systems and Control Conference (DSCC)*, 2016.

[41] K. Mccarthy, E. Walters, A. Heltzel, P. C. Krause, and J. Dalton, "Dynamic Thermal Management System Modeling of a More Electric Aircraft," in *Power Systems Conference*, 2008.

[42] B. P. Rasmussen and A. G. Alleyne, "Dynamic Modeling and Advanced Control of Air

Conditioning and Refrigeration Systems," Ph.D. dissertation, University of Illinois at Urbana-Champaign, 2006.

[43] M. A. Williams, "A Framework For The Control Of Electro-Thermal Aircraft Power Systems," Ph.D. dissertation, University of Illinois at Urbana-Champaign, 2017.

[44] P. J. Gawthrop and G. P. Bevan, "Bond-Graph Modeling - A Tutorial Introduction For Control Engineers," *IEEE Control Syst.*, vol. 27, no. 2, pp. 24–45, 2007.

[45] T. Ersal, H. K. Fathy, and J. L. Stein, "Structural simplification of modular bond-graph models based on junction inactivity," *Simul. Model. Pract. Theory*, vol. 17, no. 1, pp. 175–196, 2009.

[46] J. P. Koeln, H. C. Pangborn, M. Kawamura, and M. A. Williams, "Hierarchical Control of Aircraft Electro-Thermal Systems," *IEEE Trans. Control Syst. Technol.*, 2019.

[47] D. J. Docimo, H. C. Pangborn, and A. G. Alleyne, "Hierarchical Control for Electro-Thermal Power Management of an Electric Vehicle Powertrain," in *Proceedings of the ASME 2018 Dynamic Systems and Control Conference*, 2018.

[48] P. J. Tannous, S. R. T. Peddada, J. T. Allison, T. Foulkes, R. C. N. Pilawa-Podgurski, and A. G. Alleyne, "Model-based temperature estimation of power electronics systems," *Control Eng. Pract.*, vol. 85, no. April 2019, pp. 206–215, 2019.

[49] D. J. Docimo and A. G. Alleyne, "Electro-Thermal Graph-Based Modeling for Hierarchical Control with Application to an Electric Vehicle," in *Conference on Control Technology and Applications*, 2018.

[50] P. J. Tannous and A. G. Alleyne, "Fault detection and isolation for complex thermal management systems," in *Proceedings of the ASME 2018 Dynamic Systems and Control Conference (DSCC)*, 2018.

[51] P. J. Tannous, D. J. Docimo, H. C. Pangborn, and A. G. Alleyne, "Hierarchical Estimation for Complex Multi-Domain Dynamical Systems," in *American Control Conference (ACC)*, 2019.

[52] S. G. Garrow, C. T. Aksland, S. Sharma, and A. G. Alleyne, "Integrated Modeling for Battery Electric Vehicle Transcritical Thermal Management System," *Proc. Am. Control Conf.*, vol. 2018-June, pp. 5632–5638, 2018.

[53] Y. Ji and N. Geroliminis, "On the spatial partitioning of urban transportation networks," *Transp. Res. Part B Methodol.*, vol. 46, no. 10, pp. 1639–1656, 2012.

[54] J. Yu, H. Huang, and S. Tian, "Survey of Clustering Algorithms," *IEEE TRANSACATIONS NEURAL NETWORKS*, vol. 16, no. 3, pp. 645–678, 2005.

[55] S. E. Schaeffer, "Graph clustering," *Comput. Sci. Rev.*, vol. 1, no. 1, pp. 27–64, 2007.

[56] S. Guha, R. Rastogi, and K. Shim, "CURE: An efficient clustering algorithm for large databases," in *ACM SIGMOD Record*, 1998, vol. 27, no. 2, pp. 73–84.

[57] S. Guha, R. Rastogi, and K. Shim, "Rock: a robust clustering algorithm for categorical attributes," *Inf. Syst.*, vol. 25, no. 5, pp. 345–366, 2000.

[58] L. Xiaohong and H. Jingwei, "SHC: A spectral algorithm for hierarchical clustering," in

International Conference on Multimedia Information Networking and Security, MINES 2009, 2009.

[59] S. Guattery and G. L. Miller, "On the Performance of Spectral Graph Partitioning Methods," in *the Sixth Annual ACM/SIAM Symposium on Discrete Algorithms (SODA)*, 1995.

[60] U. Von Luxburg, "A tutorial on spectral clustering," *Stat. Comput.*, vol. 17, no. 4, pp. 395–416, 2007.

[61] R. J. Sánchez-García *et al.*, "Hierarchical spectral clustering of power grids," *IEEE Trans. Power Syst.*, vol. 29, no. 5, pp. 2229–2237, 2014.

[62] H. C. Pangborn, "Hierarchical Control For Multi-Domain Coordination Of Vehicle Energy Systems With Switched Dynamics," University of Illinois at Urbana-Champaign, 2019.

[63] P. J. Tannous and A. G. Alleyne, "Mutli-Level Hierarchical Estimation For Thermal Management Systems of Electrified Vehicles," *J. Dyn. Syst. Meas. Control*.

[64] P. J. Tannous, S. R. T. Peddada, J. T. Allison, T. Foulkes, R. C. N. Pilawa-Podgurski, and A. G. Alleyne, "Dynamic temperature estimation of power electronics systems," *Control Eng. Pract.*, vol. 85, no. January, pp. 206–215, 2019.

[65] A. C. Antoulas, *Approximation of Large-Scale Dynamical Systems*. Philadelphia: SIAM, 2005.

[66] C. T. Aksland, "Modular Modeling And Control of A Hybrid Unmanned Aerial Vehicle's Powertrain," University of Illinois at Urbana-Champaign, 2019.

[67] S. R. T. Peddada, P. J. Tannous, A. G. Alleyne, and J. T. Allison, "Optimal Sensor Placement Methods in Active High Power Density Electronic Systems With Experimental Validation," *J. Mech. Des.*, vol. 142, no. 2, pp. 1–13, 2020.

[68] J. P. Koeln, M. A. Williams, and A. G. Alleyne, "Hierarchical Control of Multi-Domain Power Flow in Mobile Systems - Part I: Framework Development and Demonstration," in *Proceedings of the ASME 2015 Dynamic Systems and Control Conference*, 2015.

[69] K. Deng, S. Goyal, P. Barooah, and P. G. Mehta, "Structure-preserving model reduction of nonlinear building thermal models," *Automatica*, vol. 50, no. 4, pp. 1188–1195, 2014.

[70] S. Lall, P. Krysl, and J. E. Marsden, "Structure-preserving model reduction for mechanical systems," *Phys. D Nonlinear Phenom.*, vol. 184, no. 1–4, pp. 304–318, 2003.

[71] N. Monshizadeh, H. L. Trentelman, and M. K. Camlibel, "Projection-based model reduction of multi-agent systems using graph partitions," *IEEE Trans. Control Netw. Syst.*, vol. 1, no. 2, pp. 145–154, 2014.

[72] Y. Gu, N. Bottrell, and T. C. Green, "Reduced-Order Models for Representing Converters in Power System Studies," *IEEE Trans. Power Electron.*, vol. 33, no. 4, pp. 3644–3654, 2018.

[73] D. A. Copp, R. Gondhalekar, and J. P. Hespanha, "Simultaneous model predictive control and moving horizon estimation for blood glucose regulation in Type 1 diabetes," *Optim. Control Appl. Methods*, vol. 39, no. 2, pp. 904–918, 2018.

[74] R. Olfati-Saber, “Distributed Kalman filtering for sensor networks,” *Proc. IEEE Conf. Decis. Control*, pp. 5492–5498, 2007.

[75] F. S. Cattivelli and A. H. Sayed, “Diffusion strategies for distributed Kalman filtering and smoothing,” *IEEE Trans. Automat. Contr.*, vol. 55, no. 9, pp. 2069–2084, 2010.

[76] T. Van Cutsem, J. L. Horward, and M. Ribbens-Pavella, “A two-level static state estimator for electric power systems,” *IEEE Trans. Power Appar. Syst.*, vol. PAS-100, no. 8, pp. 3722–3732, 1981.

[77] K. L. Lo, M. M. Salem, R. D. Mccoll, and A. M. Moffattt, “Two-level state estimation for large power system Part 1: Algoirthm,” *IEEE Proc. C, Gener. Transm. Distrib.*, vol. 135, no. 4, pp. 299–308, 1988.

[78] S. Iwamoto, M. Kusano, and V. H. Quintana, “Hierarchical state estimation using a fast rectangular-coordinate method [power system analysis computing],” *Power Syst. IEEE Trans.*, vol. 4, no. 3, pp. 870–880, 1989.

[79] T. Van Cutsem and M. Ribbens-Pavella, “Critical Survey of Hierarchical Methods for State Estimation of Electric Power Systems,” *IEEE Trans. Power Appar. Syst.*, no. 10, 1983.

[80] G. N. Korres, “A distributed multiarea state estimation,” *IEEE Trans. Power Syst.*, vol. 26, no. 1, pp. 73–84, 2011.

[81] L. Zhao and A. Abur, “Multiarea State Estimation Using Synchronized Phasor Measurements,” *IEEE Trans. Power Syst.*, vol. 20, no. 2, pp. 611–617, 2005.

[82] A. Gómez-Expósito, A. Abur, A. de la V. Jaén, and C. Gómez, “A Multilevel State Estimation Paradigm for Smart Grids,” *Proc. IEEE*, vol. 99, no. 6, 2011.

[83] S. Lakshminarasimhan and A. A. Girgis, “Hierarchical State Estimation Applied to Wide-Area Power Systems,” in *2007 IEEE Power Engineering Society General Meeting*, 2007.

[84] R. Li, A. B. Corripio, M. A. Henson, and M. J. Kurtz, “On-line state and parameter estimation of EPDM polymerization reactors using a hierarchical extended Kalman filter,” *J. Process Control*, vol. 14, no. 8, pp. 837–852, 2004.

[85] S. A. Zonouz and W. H. Sanders, “A Kalman-based coordination for hierarchical state estimation: Algorithm and analysis,” *Proc. Annu. Hawaii Int. Conf. Syst. Sci.*, 2008.

[86] D. Liberzon, *Switching in Systems and Control*, 1st ed. Springer Science+Business Media New York, 2003.

[87] G. Böker and J. Lunze, “Stability and performance of switching Kalman filters,” *Int. J. Control*, vol. 75, no. 16, pp. 1269–1281, 2002.

[88] X. Yin, J. Zeng, and J. Liu, “Forming Distributed State Estimation Network From Decentralized Estimators,” *IEEE Trans. Control Syst. Technol.*, vol. 27, no. 6, pp. 2430–2443, 2018.

[89] A. Valade, P. Acco, P. Grabolosa, and J. Y. Fourniols, “A study about kalman filters applied to embedded sensors,” *Sensors*, vol. 17, no. 12, pp. 1–18, 2017.

[90] Y.-S. Wang, S. You, and N. Matni, “Localized Distributed Kalman Filters for Large-Scale

Systems," *IFAC-PapersOnLine*, vol. 48, no. 22, pp. 52–57, 2015.

[91] R. Olfati-Saber, "Distributed Kalman filter with embedded consensus filters," *Proc. 44th IEEE Conf. Decis. Control. Eur. Control Conf. CDC-ECC '05*, vol. 2005, pp. 8179–8184, 2005.

[92] J. L. Speyer, "Computation and Transmission Requirements for a Decentralized Linear-Quadratic_Gaussian Control Problem," *IEEE Trans. Automat. Contr.*, vol. 24, no. 2, pp. 266–269, 1979.

[93] R. Gautam Dutta, T. Zhang, and Y. Jin, "Resilient Distributed Filter for State Estimation of Cyber-Physical Systems Under Attack," in *American Control Conference (ACC)*, 2019.

[94] C. Favre, "Fly-by-wire for commercial aircraft : the Airbus experience," *Int. J. Control*, vol. 59, no. 1, pp. 139–157, 1994.

[95] E. Kiyak, O. Cetin, and A. Kahvecioglu, "Aircraft sensor fault detection based on unknown input observers," *Aircr. Eng. Aerosp. Technol. An Int. J.*, vol. 80, no. 5, pp. 545–548, 2008.

[96] D. Briere and P. Traverse, "AIRBUS A320 / A330 / A340 Electrical Flight Controls A Family of Fault-Tolerant Systems," in *Fault-Tolerant Computing*, 1993, pp. 616–623.

[97] P. Castaldi, W. Geri, M. Bonfè, S. Simani, and M. Benini, "Design of residual generators and adaptive filters for the FDI of aircraft model sensors," *Control Eng. Pract.*, vol. 18, no. 5, pp. 449–459, 2010.

[98] D. G. Dimogianopoulos, J. D. Hios, and S. D. Fassois, "FDI for aircraft systems using stochastic pooled-NARMAX representations: Design and assessment," *IEEE Trans. Control Syst. Technol.*, vol. 17, no. 6, pp. 1385–1397, 2009.

[99] J. Bokor, S. Ganguli, I. Szaszi, G. J. Balas, and A. Marcos, "Application of FDI to a Nonlinear Boeing -747 Aircraft," *Proc. 10th Mediterr. Conf. Control Autom. - MED2002*, 2002.

[100] W. Xue, Y. Q. Guo, and X. D. Zhang, "Application of a bank of Kalman filters and a Robust Kalman filter for aircraft engine sensor/actuator fault diagnosis," *Int. J. Innov. Comput. Inf. Control*, vol. 4, no. 12, pp. 3161–3168, 2008.

[101] M. L. Fravolini, V. Brunori, G. Campa, M. R. Napolitano, and M. La Cava, "Structural analysis approach for the generation of structured residuals for aircraft FDI," *IEEE Trans. Aerosp. Electron. Syst.*, vol. 45, no. 4, p. 1446, 2009.

[102] D. W. and K.-Y. Lum, "Adaptive unknown input observer approach for aircraft actuator fault detection and isolation," *Int. J. Adapt. Control Signal Process.*, vol. 22, no. 4, pp. 325–343, 2007.

[103] Y. Seng and R. Srinivasan, "Engineering Applications of Artificial Intelligence Multi-agent based collaborative fault detection and identification in chemical processes," *Eng. Appl. Artif. Intell.*, vol. 23, no. 6, pp. 934–949, 2010.

[104] Y. Chetouani, "Design Of A Multi- Model Observer-Based Estimator For Fault Detection And Isolation (FDI) Strategy: Application To A Chemical Reactor," *Brazilian J. Chem. Eng.*, vol. 25, no. 04, pp. 777–788, 2008.

[105] O. A. Z. Sotomayor and D. Odloak, “Observer-based fault diagnosis in chemical plants,” *Chem. Eng. J.*, vol. 112, no. 1–3, pp. 93–108, 2005.

[106] K. Roy, R. N. Banavar, and S. Thangasamy, “Application of Fault Detection and Identification (FDI) Techniques in Power Regulating Systems of Nuclear Reactors,” *IEEE TRANSACATIONS Nucl. Sci.*, vol. 45, no. 6, pp. 3184–3201, 1998.

[107] B. Upadhyaya, K. Zhao, and B. Lu, “Fault Monitoring Of Nuclear Power Plant Sensors And Field Devices,” *Prog. Nucl. Energy*, vol. 43, no. 1, pp. 337–342, 2003.

[108] R. Peuget, S. Courtine, and J. Rognon, “Fault Detection and Isolation on a PWM Inverter by Knowledge-Based Model,” *IEEE Trans. Ind. Appl.*, vol. 34, no. 6, pp. 1318–1326, 1998.

[109] Z. Gao, C. Cecati, and S. X. Ding, “A Survey of Fault Diagnosis and Fault-Tolerant Techniques Part I: Fault Diagnosis,” *IEEE Trans. Ind. Electron.*, vol. 62, no. 6, pp. 3768–3774, 2015.

[110] R. Venkataraman, P. Bauer, P. Seiler, and B. Vanek, “Comparison of fault detection and isolation methods for a small unmanned aircraft,” *Control Eng. Pract.*, vol. 84, pp. 365–376, 2019.

[111] S. Tahraoui, A. Meghebbar, D. Boubekeur, and A. Boumédiène, “System modeling and faults diagnosis of a five hydraulic tank,” *Control Eng. Appl. Informatics*, vol. 18, no. 1, pp. 59–67, 2016.

[112] J. Anzurez-Marin, N. Pitalúa-Díaz, O. Cuevas-Silva, and J. Villar-García, “Unknown inputs observers design for fault detection in a two-tank hydraulic system,” *Proc. - Electron. Robot. Automot. Mech. Conf. CERMA 2008*, pp. 373–378, 2008.

[113] P. Zhang, Y. M. Fu, and G. R. Duan, “Design of unknown input observer for a class of linear time-delay systems,” *Int. J. Control. Autom. Syst.*, vol. 2, no. 4, pp. 530–535, 2004.

[114] J. Chen, *Robust Model-Based Fault Diagnosis for Dynamic Systems*, no. 1. 2014.

[115] M. Corless and J. Tu, “State and input estimation for a class of uncertain systems,” *Automatica*, vol. 34, no. 6, pp. 757–764, 1998.

[116] M. Darouach, M. Zasadzinski, and S. J. J. Xu, “Full-order observers for linear systems with unknown inputs,” *IEEE Trans. Automat. Contr.*, vol. 39, no. 3, pp. 606–609, 1994.

[117] Y. Guan and M. Saif, “A novel approach to the design of unknown input observers,” *Autom. Control. IEEE Trans.*, vol. 36, no. 5, pp. 632–635, 1991.

[118] M. Hou and P. C. Muller, “Design of Observers for Linear Systems with Unknown Inputs,” *IEEE Trans. Automat. Contr.*, vol. 37, no. 6, 1992.

[119] B. Moore, “Principal component analysis in linear systems: Controllability, observability, and model reduction,” *IEEE Trans. Automat. Contr.*, vol. 26, no. 1, pp. 17–32, 1981.

[120] K. Glover, “All optimal Hankel-norm approximations of linear multivariable systems and their L, ∞ -error bounds,” *Int. J. Control*, vol. 39, no. 6, pp. 1115–1193, 1984.

[121] W. Schilders, *Introduction to Model Order Reduction*. 2008.

[122] K. Deng, P. Barooah, P. G. Mehta, and S. P. Meyn, “Building Thermal Model Reduction

via Aggregation of States," in *American Control Conference (ACC)*, 2010.

[123] K. Deng, S. Goyal, P. Barooah, and P. G. Mehta, "Structure-preserving model reduction of nonlinear building thermal models," *Automatica*, vol. 50, no. 4, pp. 1188–1195, 2014.

[124] W. A. Hudson and M. L. Levin, "Integrated Aircraft Fuel Thermal Thermal Management System," 1998.

Appendix A

Parameters of the Unknown Input Observers

The following parameters are used to design the bank of unknown input observers presented in section 6.5.

$$A=\begin{bmatrix} -0.3845 & 0.2983 & 0 & 0 & 0 & 0 & 0 & 0.0862 & 0 & 0 \\ 0.3995 & -0.5148 & 0.1153 & 0 & 0 & 0 & 0 & 0 & 0 & 0 \\ 0 & 0.1100 & -0.3565 & 0.2465 & 0 & 0 & 0 & 0 & 0 & 0 \\ 0 & 0 & 0.2465 & -1.2982 & 0.5923 & 0.4594 & 0 & 0 & 0 & 0 \\ 0 & 0 & 0 & 0.9930 & -1.4099 & 0.4169 & 0 & 0 & 0 & 0 \\ 0 & 0 & 0 & 0.4594 & 0.2487 & -1.9904 & 0.3005 & 0 & 0 & 0.9819 \\ 0 & 0 & 0 & 0 & 0 & 0 & -1.42e^{-4} & 1.4e^{-4} & 0 & 0 \\ 0.1102 & 0 & 0 & 0 & 0 & 0 & 17.5457 & -18.2123 & 0 & 0.5564 \\ 0 & 0 & 0 & 0 & 0 & 0 & 0 & 0 & -0.69 & 0.69 \\ 0 & 0 & 0 & 0 & 0 & 7.8e^{-6} & 0 & 4.4e^{-6} & 5.3e^{-6} & -1.75e^{-5} \end{bmatrix} \quad \text{(A1)}$$

$$B=\begin{bmatrix} 0 & -31.03 \\ 0 & 41.56 \\ 0 & 0 \\ 0 & 0 \\ 0 & 0 \\ 0 & 0 \\ 0 & 0 \\ 0 & 0 \\ 65.25 & 0 \\ -4.95e^{-4} & 0 \end{bmatrix} \quad \text{(A2)}$$

$$C=\begin{bmatrix}0&0&0&0&0&0&0&0&0&1\\0&0&0&0&0&0&0&0&1&0\\0&0&0&0&0&0&1&0&0&0\\0&0&1&0&0&0&0&0&0&0\\1&0&0&0&0&0&0&0&0&0\\0&0&0&0&0&1&0&0&0&0\end{bmatrix} \tag{A3}$$

$$H^{1}=\begin{bmatrix}1.8&1.1&2&0&1.7&1.2\\2.1&1.4&2.5&0&2&1.5\\2&1.3&2&10&1.9&1.4\\2.2&1.5&2.1&0&2.1&1.6\\2.6&1.9&1.9&0&2.5&2\\2.1&1.4&1.9&0&2&1.5\\1.9&1.2&2.3&0&1.8&1.3\\2.1&1.4&2&0&2&1.5\\2.6&1.9&1.9&0&2.5&2\\1.8&1.1&2.5&0&1.7&1.2\end{bmatrix}\times e^{-6} \tag{A4}$$

$$H^{2}=\begin{bmatrix}1.8&90&2.5&0&1.7&120\\2.1&140&2.5&0&2&150\\2&130&2&10&1.9&790\\2.2&150&2.5&0&2.1&160\\2.6&190&1.9&0&2.5&200\\2.1&300&3.2&0&2&150\\1.9&120&2.3&0&1.8&130\\2.1&530&2&0&2&150\\2.6&190&1.9&0&2.5&200\\1.8&110&3.5&0&1.7&120\end{bmatrix}\times e^{-6} \tag{A5}$$

$$E=\begin{bmatrix}1\\1\\1\\1\\1\\0\\0\\0\\0\\0\end{bmatrix} \tag{A6}$$

$$eig(UIO1)=\begin{bmatrix}-40&-35&-38&-47&-62&-58.3&-59&-49.7&-54&-31\end{bmatrix} \tag{A7}$$

$$eig(UIO2)=\begin{bmatrix}-2&-3&-4&-5&-6&-7&-8&-9&-10&-11\end{bmatrix} \tag{A8}$$

$$d=10 \tag{A9}$$